

**TWO-PHOTON PHOTOEMISSION SPECTROSCOPY
OF WET ELECTRON STATE AND FEMTOSECOND
ELECTRON DYNAMICS ON TiO₂ SURFACES**

by

Bin Li

B. S. in Applied Physics, Peking University, China, 1999

M. S. in Physics, University of Pittsburgh, USA, 2000

Submitted to the Graduate Faculty of
Arts and Sciences in partial fulfillment
of the requirements for the degree of
Doctor of Philosophy

University of Pittsburgh

2006

UNIVERSITY OF PITTSBURGH
SCHOOL OF ARTS AND SCIENCES

This thesis was presented

By

Bin Li

It was defended on

August 11, 2006

and approved by

Hrvoje Petek, Professor, Departmental of Physics and Astronomy

Hong Koo Kim, Professor, Departmental of Electrical Engineering

Daniel Boyanovsky, Professor, Departmental of Physics and Astronomy

Jeremy Levy, Professor, Departmental of Physics and Astronomy

David Snoke, Professor, Department of Physics and Astronomy

Albert Heberle, Associate Professor, Department of Physics and Astronomy

Thesis Advisor: Hrvoje Petek, Professor, Departmental of Physics and Astronomy

Copyright © by Bin Li

2006

TWO-PHOTON PHOTOEMISSION SPECTROSCOPY OF WET ELECTRON STATE AND FEMTOSECOND ELECTRON DYNAMICS ON TiO₂ SURFACES

Bin Li, PhD

University of Pittsburgh, 2006

Combination of the femtosecond laser time-resolved two-photon photoemission (TR-2PP) and the ultra high vacuum (UHV) surface science preparation techniques provides the possibility to study the electronic structures and the interfacial electron transfer dynamics at the atomically ordered adsorbate overlayers on single-crystalline surfaces, such as TiO₂. The nearly perfect, stoichiometric TiO₂ surface is prepared by a standard surface-preparation protocol, while various UHV surface preparation methods are available to modify the stoichiometric surfaces by introducing defects and/or adsorbed molecules. Two-photon photoemission (2PP) spectroscopy with near ultraviolet (400 nm) femtosecond laser pulses are used to investigate systematically the work function, and the occupied and unoccupied electronic structure of TiO₂ surfaces due to the presence of defects and adsorbates. Adsorbates e.g. O₂, H₂O, CH₃OH are introduced onto TiO₂ surfaces to investigate their interaction with the TiO₂ surface, as well as the ultrafast interfacial charge transfer dynamics. O₂ molecules act as electron acceptors and titrate (heal) the surface O atom vacancy defects. H₂O acts as an electron donor and forms a monolayer

structure with an effective electric-dipole of 0.5 D pointing outwards. More remarkably, at ~ 1 monolayer coverage of water with minority -OH species present on TiO₂ surfaces, an unoccupied state of 2.45 eV above the Fermi level is observed. Density functional theory shows this to be a “wet-electron” state, representing the lowest energy nonadiabatic electron transfer pathway through the interface. The decay of the wet-electron state through the reverse charge transfer occurs within 15 femtoseconds, faster than the dielectric response time scale of the H₂O overlayer. Similarly, the chemisorption of CH₃OH molecules on TiO₂ surfaces induces a related resonance at 2.3 ± 0.2 eV above the Fermi level. Following the injection of electrons into the CH₃OH overlayer we can follow by pump-probe measurements the ultrafast dielectric response of the interface leading to the solvation of injected electrons. Surprisingly, the solvation dynamics exhibit a strong deuterium-isotope effect. The excess charge is stabilized by the structural reorganization of the interface involving the inertial motion of substrate ions (polaron formation), followed by slower diffusive solvation by the molecular overlayer. According to the pronounced isotope effect on the electron lifetime, this motion of heavy atoms transform the reverse charge transfer from a purely electronic process (nonadiabatic) to a proton-coupled electron transfer (PCET) regime on ~ 30 fs time scale.

Contents

Contents	vi
List of Figures	x
Acronyms	xv
Notation	xvii
Publications	xviii
Acknowledgement	xix
Chapter One: Introduction	1
1.1 TiO ₂ Fundamentals	1
1.2 Applications of TiO ₂	7
1.3 Application of Two-photon Photoemission (2PP) Technique to Molecule/TiO ₂ System	12
Chapter Two: Experimental Apparatus	20
2.1 Laser system	20
2.1.1 Ti:Sapphire Oscillator	21
2.1.2 Non-linear Optics	22

2.1.3 The Variable Time-delay Generation with a Mach-Zehnder Interferometer.....	28
2.2 The UHV Chamber and Electronic Instruments	29
2.2.1 Overview of the UHV system	29
2.2.2 The Hemispherical Electron Energy Analyzer and the Channeltron Detector.....	33
2.2.3 The Fundamentals of Photoemission Experiments	36
2.3 Data Acquisition and Diagnostic System	38
2.3.1 The Overview of the Data Acquisition System	38
2.3.2 Spectroscopy and 7-channel Data Acquisition	39
2.3.3 Time-resolved Dynamic Measurement and Signal Synchronization.....	41
<u>Chapter Three: 2PP Background</u>	<u>45</u>
3.1 Hot Electron Dynamics	45
3.1.1 Laser Pulse Induced Electron Distribution at the Intermediate Unoccupied States	46
3.1.2 Fermi-Liquid Theory Description of Electron-electron Scattering.....	48
3.1.3 Other Electron Dynamical Pathways	53
3.2 Diagnostic Measurement for the Laser Excitation Source	58
3.2.1 Nonlinear Auto-correlation Characterization of the Laser Pulse.....	58
3.2.2 Dispersion and Linear Chirp for a Gaussian Pulse	62
3.3 Optical Bloch Equation Approach to Simulating Electron Dynamics.....	68
3.4 Hot Electron Dynamics and the Fitting Procedures	75

<u>Chapter Four: 2PP Measurements on TiO₂ Surfaces</u>	80
4.1 2PP Spectra for Various Bare TiO ₂ Surfaces	81
4.2 Oxygen Adsorption on TiO ₂ Surfaces	87
4.2.1 O ₂ does not adsorb at the Stoichiometric Surface.....	89
4.2.2 O ₂ Adsorption at the TiO ₂ Sample with Surface Defects.....	90
4.2.3 O ₂ Adsorption at the Sample with Both Surface and Sub-surface Defects.....	92
4.2.4 Oxygen Adsorption on the Heavily Damaged TiO ₂ Surface.....	95
<u>Chapter Five: Observation of Wet Electrons at the H₂O/TiO₂ (110) Surface</u>	98
5.1 The Model for H ₂ O Adsorption on the TiO ₂ (110) Surface.....	99
5.2 H ₂ O Adsorption on Various TiO ₂ Surfaces: the Work Function Changes.....	102
5.3 The Unoccupied Electronic Structures for H ₂ O Adsorbed on Defective TiO ₂ Surfaces.....	107
5.4 Temperature Dependence of the Water-induced Resonance Intensity.....	112
5.5 DFT Electronic Structures of H ₂ O/TiO ₂ Surfaces	115
5.6 Atomic-H Adsorption on TiO ₂ Surface and co-adsorption with H ₂ O.....	118
5.7 Charge Transfer Dynamics at the H ₂ O/TiO ₂ Interface	123
<u>Chapter Six: Electron Solvation in Methanol Overlayers on TiO₂ Surfaces</u>	127
6.1 Methanol Adsorption Structures	128
6.2 CH ₃ OH Adsorption Induced Wet-Electron States	131
6.3 Electron Dynamics at the CH ₃ OH/TiO ₂ Interface: Energy and Coverage	

Dependence	135
6.4 The Kinetic Scheme for Simulating the CH ₃ OH Dynamics.....	139
6.5 Charge Transfer Dynamics, Isotopic Effect, Solvation and Proton Coupled Electron Transfer Mechanism	144
6.6 DFT Electronic Structure Interpretation of the PCET Dynamics.....	154
<u>Chapter Seven: Summary and Conclusions</u>	<u>161</u>
<u>Appendix A: The Typical Parameters of the 2PP Spectroscopy.....</u>	<u>165</u>
<u>Appendix B: Software for Time-resolved Experiment.....</u>	<u>167</u>
<u>Appendix C: Universal Curve for Electron Escape Depth.....</u>	<u>197</u>
<u>Appendix D: Density Functional Theory.....</u>	<u>198</u>
<u>Bibliography.....</u>	<u>201</u>

List of Figures

1.1	The unit cell structure of rutile TiO ₂	2
1.2	(a) The stoichiometric and (b) defective TiO ₂ surfaces	3
1.3	The calculated electronic structure of the bulk-reduced TiO ₂ crystal along with the bandgap states	4
1.4	The UPS spectra of the reduced TiO ₂ surfaces	6
1.5	High resolution STM image of the TiO ₂ (110)-(1×1) crystal surface	7
1.6	Photocatalysis of H ₂ O on a TiO ₂ based composite catalyst	9
1.7	Schematic of the operation of the dye-sensitized TiO ₂ solar cell	10
1.8	The electron transfer mechanism mediated by the molecular excited states, from the adsorbate overlayer to the oxide substrates	13
1.9	Charge transfer from the aromatic adsorbate to the TiO ₂ substrate	15
1.10	MD simulations for charge transfer in the catechol/anatase-TiO ₂ structures	16
1.11	The 2PP process at TiO ₂ surface and the charge injection between the surface molecules and the substrate.....	18
2.1	The optical system for the time-resolved photoemission experiment.....	21
2.2	The phase matching condition for a negative uniaxial non-linear optical crystal.....	24

2.3	The diagram for the Type I SHG generation with a BBO crystal.....	26
2.4	The fundamental and second harmonic spectra of theTi:Sapphire laser	27
2.5	Overview of the UHV System	30
2.6	The diagram of the multi-channel energy analyzer.....	35
2.7	Electron amplification in a channeltron	36
2.8	The schematic diagram of a 2PP measurement for a wide bandgap semi-conductor (TiO ₂) and the energy alignment.....	37
2.9	Overview of the electronic data acquisition system.....	38
2.10	The screenshot of the software window during a 7-channel data acquisition	40
2.11	The electronic system for the interferometric two-pulse correlation measurements.....	41
2.12	Signal synchronization between the calibration interference fringes and the two-pulse correlation Signals.....	43
3.1	Excitation scheme in two-photon process.....	47
3.2	The electron-electron scattering process according to the Fermi-Liquid theory.....	50
3.3	The experimentally measured hot-electron lifetimes compared with theoretical calculations by Free-electron model or the band structure calculation.....	53
3.4	Various electron excitation mechanism in copper.....	54
3.5	Excited electron transport into the bulk.....	57
3.6	SSHG at a metal surface	61
3.7	The calculated interferometric auto-correlation signals for Gaussian pulses with different linear chirp dispersions.....	67
3.8	Experimental auto-correlation signals for laser pulse.....	68

3.9	OBE in a metal or a semi-conductor system	70
3.10	A typical I2PC signal on the adsorbates covered TiO ₂ surface is decomposed into three components: 0ω , 1ω , 2ω , and the coherent/incoherent fitting procedures for the electron dynamics.....	77
4.1	Energy diagram of the defective TiO ₂ crystal and 2PP measurement with the electron energy analyzer.....	81
4.2	2PP spectra of stoichiometric, electron-irradiated, vacuum annealed, and Ar ⁺ sputtered surfaces at 90 K.....	83
4.3	Photoemission spectra of bare Ar ⁺ sputtered surface at 100 K measured with different modes of excitation.....	85
4.4	Diagram of the O ₂ adsorption on an Oxygen-deficient TiO ₂ (110) surface	88
4.5	The effect of Oxygen exposure onto the stoichiometric surface	89
4.6	2PP spectra of electron-irradiate surface at 100 K and exposure to oxygen molecules.....	91
4.7	2PP spectra of vacuum annealed surfaces before and after exposure to oxygen.....	93
4.8	2PP spectra of Ar ⁺ sputtered surfaces before and after exposure to oxygen.....	96
5.1	The model for H ₂ O/TiO ₂ interface.....	99
5.2	(a) The calculated structure of 1 ML H ₂ O on TiO ₂ surface and (b)UPS spectra.....	101
5.3	2PP spectra for the progressive H ₂ O adsorption onto a stoichiometric TiO ₂ surface.....	103
5.4	The work function change upon the water exposure to various TiO ₂ surfaces.....	107
5.5	2PP spectra for successive exposures of reduced (annealed) TiO ₂ (110) surface to H ₂ O.....	109
5.6	The 2PP deference spectra of deposition ~1 ML H ₂ O to the reduced TiO ₂ surface.....	110

5.7	The wet electron-state peak area and the work-function change plotted as a function of water exposure	112
5.8	TPD spectra for different initial exposures of water to TiO ₂ (110) surface.....	113
5.9	The 2PP difference spectra recorded at different temperatures after exposing the reduced TiO ₂ surface to H ₂ O below 100 K.....	114
5.10	The molecular structures and orbital distribution for the 1 ML H ₂ O + 0.5 ML H covered TiO ₂ surface at 2.4 eV above the E _F	116
5.11	The correlation of the wet-electron energy for different coverages of H ₂ O and H adsorbates with the number of dangling H atoms in each of hydration cluster.....	118
5.12	2PP spectra for atomic H progressive exposures onto a stoichiometric TiO ₂ surface.....	120
5.13	The STM image for H-terminated surface along with low energy electron irradiation.....	121
5.14	The comparison of 2PP spectra excited with s- and p-polarized light for different exposures of the mild hydroxylated TiO ₂ (110) surface to H ₂ O molecules.....	122
5.15	Time-resolved measurement at various electron energies of ~ 1 ML H ₂ O covered TiO ₂ (110) surface and the phase-averaged I2PC spectra	124
5.16	Phase-averaged I2PC scans for the bare reduced TiO ₂ , and after exposure to 0.5 and 1.1 ML of H ₂ O.respectively, along with OBE simulation results.....	126
6.1	Possible adsorption sites and structures of CH ₃ OH on TiO ₂ (110) surface.....	129
6.2	Several calculated structures for the chemisorption of CH ₃ OH on TiO ₂ (110) surface.....	130
6.3	2PP spectra for a series of exposures of CH ₃ OH on TiO ₂ surfaces.....	131
6.4	Work function change fitted by Helmholtz model and the resonance peak area for increasing	

	exposure of TiO ₂ (110) surface to CH ₃ OH.	132
6.5	The normalized 2PP spectra of (a) reduced and (b) stoichiometric TiO ₂ (110) surface exposed to 1.1 L methanol measured with p- and s- polarization at 100 K.....	133
6.6	(a) Time-resolved measurements at ~ 1.2 ML covered CH ₃ OH surface and (b) The Phase-averaged I2PC signals at various energy levels.....	136
6.7	The typical normalized I2PC intensities at the different coverages of CH ₃ OH adsorbed TiO ₂ surfaces.....	137
6.8	The 3D contour plots of the 2PP intensity decay profiles of the different amounts of CH ₃ OH adsorbed TiO ₂ surfaces.....	139
6.9	The OBE model used to simulate the electron dynamics at the CH ₃ OH/TiO ₂ surface.....	141
6.10	(a) 3D contour plots of the 2PP intensity decay profiles of the wet-electron states on CH ₃ OH adsorbed TiO ₂ (110) surfaces, (b) The experimental along with the simulated two-photon correlation signals (2PC) at the “wet electron” resonance energy, (c) the retrieved “wet-electron” population dynamics.....	146-148
6.11	(a) Comparison between CH ₃ OH and CH ₃ OD dynamics, (b) The proposed proton-coupled electron transfer dynamics in a generalized solvent coordinate.....	151
6.12	The DFT calculated orbital distributions of ground state and excite state electronic structures at ~ 1 ML CH ₃ OH covered TiO ₂ surface.....	155
6.13	Schematic diagram for the overall dynamic mechanism of the 2PP excitation occurring at the CH ₃ OH/TiO ₂ interface.....	159

Acronyms

UPS: Ultra- violet spectroscopy

CB: Conduction band

VB: Valence band

2PP: Two-photon photoemission

TR-2PP: Time-resolved two-photon photoemission

NA: Non-adiabatic mechanism

PCET: Proton-coupled electron transfer

CT: Charge transfer

RCT: Reverse charge transfer

AC: Auto-correlation

SHG: Second harmonic generation

SSHG: Surface second harmonic generation

OBE: Optical Bloch equation

2PC: Two-photon correlation

I2PC: Interferometric two-photon correlation

STM: Scanning tunneling microscopy

MOSFET: Metal-oxide-semiconductor field effective transistor

TM: Transverse magnetic mode

TE: Transverse electric mode

FWHM: Full width of half maximum

ML: Monolayer

UHV: Ultra high vacuum

TPD: Temperature programmed desorption

HREELS: High resolution electron energy loss spectroscopy

DFT: Density function theory

VASP: Vienna ab- initio simulation package code

Notation

$\hbar\omega, h\nu$	Photon
k_r	Radiative decay rate
k_{nr}	Non-radiative decay rate
k_{CT}	Charge transfer rate
Ti_{5c}^{4+}	Terminal titanium ion
$Ti_{5c}^{+4-\delta}$	Reduced terminal titanium ion
E_F	Fermi level
E_v, E_{VBM}	Valence band & Valence band maximum
E_c, E_{CBM}	Conduction band & Conduction band minimum
E_{vac}	Vacuum level
E_p	Pass energy of the electron analyzer
$f(E)$	Fermi-Dirac distribution
ϵ_0	Electric dielectric constant in vacuum
T_1^1, T_1^2	Population decay time scale at the intermediate state energy 1 or final state energy 2
$T_2^{01}, T_2^{12}, T_2^{02}$	“Pure” dephasing time scale between various energy states
$\Delta\phi$	Work function change
μ_{eff}	Effective electric dipole moment
τ_{RCT}	Reverse charge transfer time scale
τ_{PCET}	Proton-coupled electron transfer time scale
τ_{sol}	Time scale for solvation process

Publications

1. Ken Onda, Bin Li and Hrvoje Petek, “Two-photon photoemission spectroscopy of TiO₂(110) surfaces modified by defects and O₂ or H₂O adsorbates”, **Phys. Rev. B** **70**, 045415 (2004).
2. Ken Onda, Bin Li, Jin Zhao, Kenneth D. Jordan, Jinlong Yang and Hrvoje Petek, “Wet electrons at the H₂O/TiO₂(110) surface”, **Science** **308**, 1154 (2005).
3. Ken Onda, Bin Li and Hrvoje Petek, in **Ultrafast Phenomena XIV** (T. Kobayashi, K. Nelson, and S. De Silvestri) **416** (Springer-Verlag, Berlin, 2005).
4. Ken Onda, Bin Li, Jin Zhao and Hrvoje Petek, “The electronic structure of methanol covered TiO₂(110) surfaces”, **Surf. Sci.** **593**, 32 (2005).
5. Bin Li, Jin Zhao, Ken Onda, Kenneth D. Jordan, Jinlong Yang and Hrvoje Petek, “Ultrafast Interfacial Proton-coupled Electron Transfer”, **Science** **311**, 1436 (2006).
6. Jin Zhao, Bin Li, Kenneth D. Jordan, Jinlong Yang and Hrvoje Petek, “The electronic structure of partially hydrated electrons on TiO₂(110) surfaces”, **Phys. Rev. B** **73**, 159309 (2006).
7. Jin Zhao, Bin Li, Ken Onda, Min Feng, and Hrvoje Petek, “Solvated electrons on metal-oxide surfaces”, **Chemical Review** (in Press).
8. Bin Li, Jin Zhao, Ken Onda, Kenneth D. Jordan, Jinlong Yang and Hrvoje Petek, “Charge transfer dynamics in the CH₃OH overlayer at the TiO₂ (110) surfaces”, (in Preparation).

Acknowledgement

The acknowledgement should firstly go to my thesis advisor, Prof. H. Petek for his continuous support, supervision and encouragement for my Ph.D work on the TiO₂ research project, and for his precious time and endeavor to carefully read through word by word and revise this manuscript. Without a large amount of critical, but essential comments from him, my thesis cannot be improved to the present version. The special appreciation should go to Dr. Ken Onda, for his kind tutoring, effective discussion and efficient collaboration with me on the TiO₂ project up to September 2004, and also to Dr. Jin Zhao for her hard work along with her beautiful DFT calculation that provided excellent theoretical support and collaboration. The author also thanks Prof. John T. Yates, for the invaluable discussions with him and his group, also for his generously sharing hardware, chemicals and electronic devices. The acknowledgement goes to the thesis committee, Professors D. Boyanovsky, J. Levy, H. K. Kim, D. Snoke and A. P. Heberle for their kind concern for my research progress, continuous service and invaluable comments regarding to the research topics. The author also thanks Drs. A. Kubo and N. Pontius for the invaluable discussions, and for their assistance in experimental and technical problems.

Chapter 1

Introduction

The subject of this thesis is the electronic structure and interfacial charge transfer dynamics of molecule modified titanium dioxide $\text{TiO}_2(110)$ surfaces. TiO_2 is one of the most investigated metal oxides by surface science techniques, in part because of its many important applications such as in photocatalysis, as an anode in dye-sensitized solar cells, a potential gate material of the next generation of MOSFETs, as a coating with self-cleaning properties, and others [1]. Here, we investigate the electronic structure and heterogeneous charge transfer dynamics of protic solvents on rutile $\text{TiO}_2(110)$ surfaces by means of femtosecond time-resolved two-photon photoemission (TR-2PP) spectroscopy [2] [3].

1.1 TiO_2 Fundamentals

Minerals with TiO_2 stoichiometry come in many different polymorphic structures, of which rutile, anatase and brookite are most commonly found in nature and can be synthesized by different methods [1, 4]. The rutile polymorph is the primary component [5] in many important applications of TiO_2 and has been studied most extensively with surface science techniques, because it is readily available and low index crystalline surfaces can be readily prepared. The

rutile unit cell shown in Fig. 1.1, has the D_{4h}^{14} crystallographic structure ($a = b = 4.584 \text{ \AA}$, $c = 2.953 \text{ \AA}$), where titanium atoms are surrounded by six oxygen atoms in a distorted octahedral configuration.

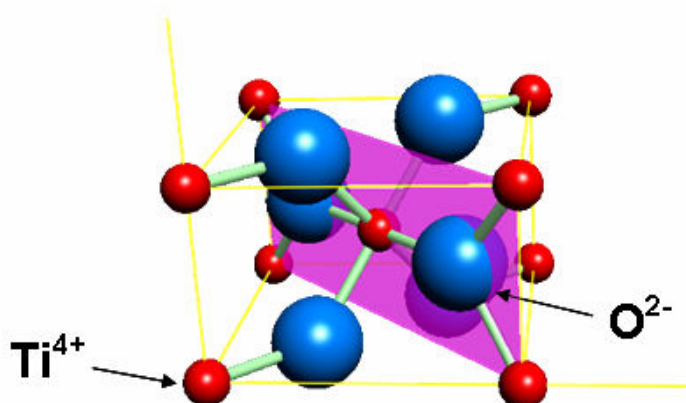


Figure 1.1 The unit cell structure of rutile TiO_2 .

Cutting through the TiO_2 crystal along the diagonal crossing surface in the unit cell structure in Fig. 1.1, we can obtain the most stable rutile- TiO_2 (110)-(1×1) crystal surface (Fig. 1.2). It contains two different types of Titanium atoms, which form rows along the [001] crystal orientation. Rows of 6-fold coordinated Ti ions alternate with the 5-fold terminal Ti ions, which are missing a single O atom ligand perpendicular to the surface. The surface also contains two kinds of oxygen atoms. Within the main surface plane, there are 3-fold coordinate oxygen atoms as in the bulk. In addition, there are the so-called bridging oxygen atoms that are above the main surface plane and form bonds to two six-coordinate Ti atoms in the surface plane. Due to the

coordinative under-saturation of the bridging oxygens, they are the subject to surface reconstruction and reaction. They are easily removed from the surface by thermal annealing or irradiation with high kinetic energy electrons or ions. Any $\text{TiO}_2(110)$ surface has some fraction of these bridging O atom vacancy defects, even what we will call stoichiometric surfaces. The defect concentration that depends on the surface preparation techniques affects the overall chemistry of the surface. Fig. 1.2 (a) and (b) demonstrate the nearly perfect stoichiometric $\text{TiO}_2(110)$ surface model and the defective surface model respectively, where the most general defective sites are the single bridging oxygen (BO) vacancies and the double BO vacancies [6].

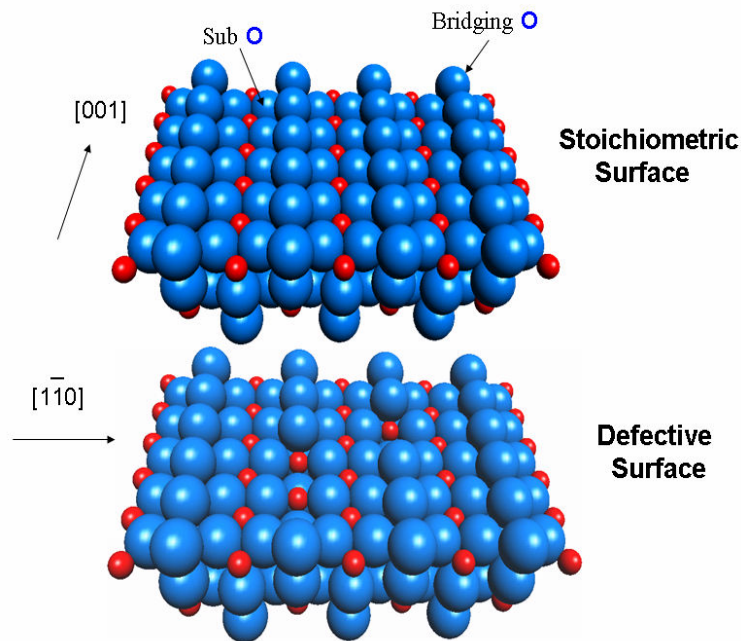


Figure 1.2 (a) The stoichiometric and (b) defective TiO_2 surfaces. Red balls represent Ti atoms and blue balls, the O atoms.

The electronic structure of TiO_2 , especially the stoichiometric surface has been calculated using a

wide variety of theoretical methods. There is a general agreement that the surface electronic structure is not much different than that of bulk. Here our main interest is in the energy states near to the Fermi level, i.e. the boundary separating the occupied and unoccupied states. The occupied states, especially the valence bands, are mostly formed by O 2p orbitals, where the unhybridized orbitals have three-fold degeneracy. The conduction bands are derived mostly from the Ti 3d orbitals. The interaction and hybridization in between O-2p and Ti-3d orbitals in the octahedral coordination cause a crystal-field splitting of the 3d orbitals into two sub-bands. The Ti d_{z^2} and $d_{x^2-y^2}$ orbitals point directly towards the O ligands and hybridize into e_g symmetry orbitals to form σ -type bonding, and at lower energy the d_{xy} , d_{xz} and d_{yz} orbitals point normal to the O ligands and hybridize into t_{2g} symmetry orbitals to form π -type bonding.

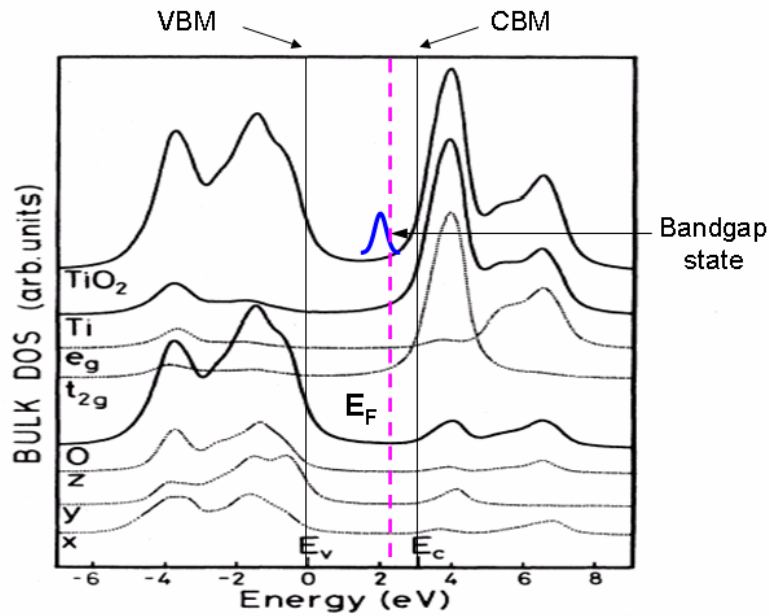


Figure 1.3 The calculated electronic structures of the bulk-reduced TiO_2 crystal, the bandgap states are indicated [7].

The calculated TiO₂ electronic structure using the tight-binding Hamiltonian by Munnix and Schmeits that is given in Fig. 1.3 [7] shows the wide band gap of TiO₂ (~3.0 eV), where the valence band maximum (VBM) is located at the highest energy level of the occupied O 2p band, and the conduction band minimum (CBM) appears as the lowest energy of the unoccupied Ti 3d band. For the stoichiometric surface, the Fermi level E_F is located approximately in the middle of the bandgap. However, undoped large band gap materials like TiO₂ are insulators, which complicate measuring photoemission spectra. The accumulation of charge on the sample surface can severely distort the photoemission signals. So a primary requirement for a successful photoemission measurement is to introduce n-type doping [8] into the insulating TiO₂ through a bulk reduction procedure. The reduction procedure by heating the crystal above 900 K creates oxygen vacancies in the sample, which increases the free-carrier concentration, and pins the Fermi level close to CBM. After this process, as shown in Fig.1.3, the sample becomes conductive, and a bandgap state appears about ~1 eV below CBM (Fig. 1.3) [9].

The Ultraviolet Photoemission Spectroscopy (UPS) spectra taken with $h\nu = 47$ eV in Fig. 1.4 show the occupied density of states (DOS) states of a reduced TiO₂ surface. The lowest binding energy of the main spectral feature at ~3 eV corresponds to the VBM in agreement with the theoretical prediction of 3 eV bandgap. However, as the sample is reduced, through exposure 500 eV electron irradiation to generate oxygen vacancies, the O 2p valence band edge shifts to higher binding energies. In addition, a distinct bandgap state appears near the Fermi level and its DOS is proportional to the concentration of the defective sites, that is, O atom vacancies that are

generated by the electron irradiation. This band gap state typically has the maximum DOS at 1 eV below the Fermi level.

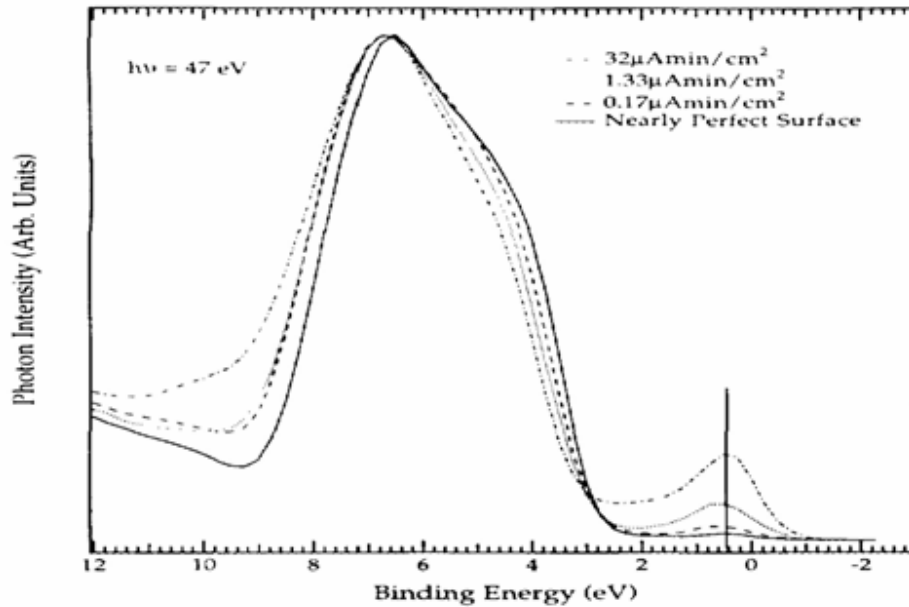


Figure 1.4 The UPS spectra of the reduced TiO₂ surfaces [9].

We have presented the model for the ideal TiO₂(110)-(1×1) surface previously, however, in reality, the surface structure depends subtle differences in the sample preparation conditions, e.g., the annealing temperature, the ambient residual gas pressure, the cooling process, and so on. We have developed a reproducible standard surface preparation procedure to obtain the well defined (110) crystal surface. As shown in Fig. 1.5, T. Minato et al. obtained an atomically resolved STM image that we expect is representative of our reduced surfaces [10]. On the left hand-side, the STM image with positive bias voltage gives the unoccupied DOS of the TiO₂ sample surface, where the bright rows are the 5-fold terminal Ti ions, and the dark rows are the BO rows. The BO vacancies appear as additional bright spots in the dark BO rows, because of

tunneling into unoccupied states of Ti ions. These BO vacancies induce the surface reduction of the 5-coordinate Ti ions at the terminal sites, associated with a bandgap state energy at ~ 1 eV below the Fermi level. The band gap states are responsible for the enhanced bright features in the occupied state image on the right side of Fig. 1.5, which is recorded with a negative bias. The small yellow dots in Fig. 1.5 indicate the BO vacancy sites which are responsible for those induced reduced Ti ions featured as enhanced bright slots (right side).

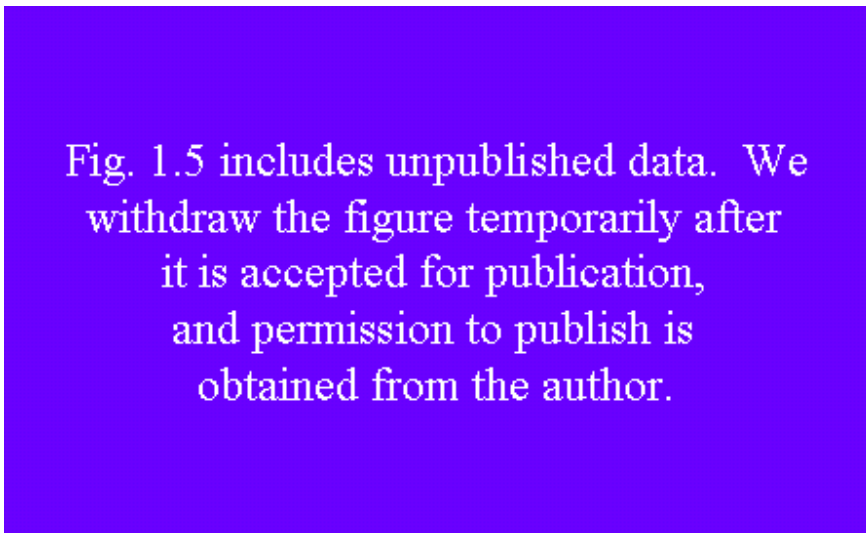


Figure 1.5 High resolution STM image of the TiO_2 (110)-(1 \times 1) crystal surface. The color-coded circles in the left figure are assigned as the identical spots in right side [10] (permission restriction).

1.2 Applications of TiO_2

Titanium dioxide (TiO_2) is a versatile material with multiple applications in science and technology [1, 11, 12]. For example, TiO_2 is widely used in photochemical and photocatalytic

reactions [3], mainly in the form of metal/TiO₂ systems, used for selective oxidation reactions [12]. Fujishima and Honda initially demonstrated the photocatalytic decomposition of H₂O on the TiO₂/Pt electrochemical system to generate O₂ and H₂, which has been of great interest as a potential energy source for the future [13]. TiO₂ is also chosen as the substrate material of the dye-sensitized photovoltaic solar cells, for converting the solar energy into electricity with efficiency as high as 10% [14]. TiO₂ is also used as photoreversible a super-hydrophilic material under UV irradiation, due to its ability to decompose hydrophobic organic molecules [15]. With the recent surge of interest in the nano-scaled field transistors, TiO₂ has become a very attractive candidate as the gate material of the next generation of MOSFETs [16]. Moreover, TiO₂ is a common white pigment in paints, ceramics, and cosmetic products [17], and can also be employed as a corrosion-protective and self-cleaning coating material [18]. It also finds applications in earth science, Li-based battery, electrochromic devices, and others [1]. In the following, we will briefly describe the two of the most relevant applications to the subject of this thesis, namely TiO₂ based photocatalytic splitting of H₂O and photovoltaic solar cells.

TiO₂ can be effectively photoexcited through band-gap irradiation to create the electron-hole charge separation. Under the circumstances when the electrochemical potentials of both the H₂/H₂O and O₂/H₂O redox couples (in Fig. 1.6) are overcome, the photosplitting of H₂O is feasible. In Fig. 1.6, we give an schematic of the photocatalytic splitting of H₂O through a composite catalyst, which includes the TiO₂ colloidal powder along with deposited metal particles for H₂ catalysis (e.g. Pt) and semiconductor particles for O₂ evolution (e.g. RuO₂·nH₂O)

[11, 12]. The proposed mechanism can be described by the following equations and shown in Fig. 1.6.

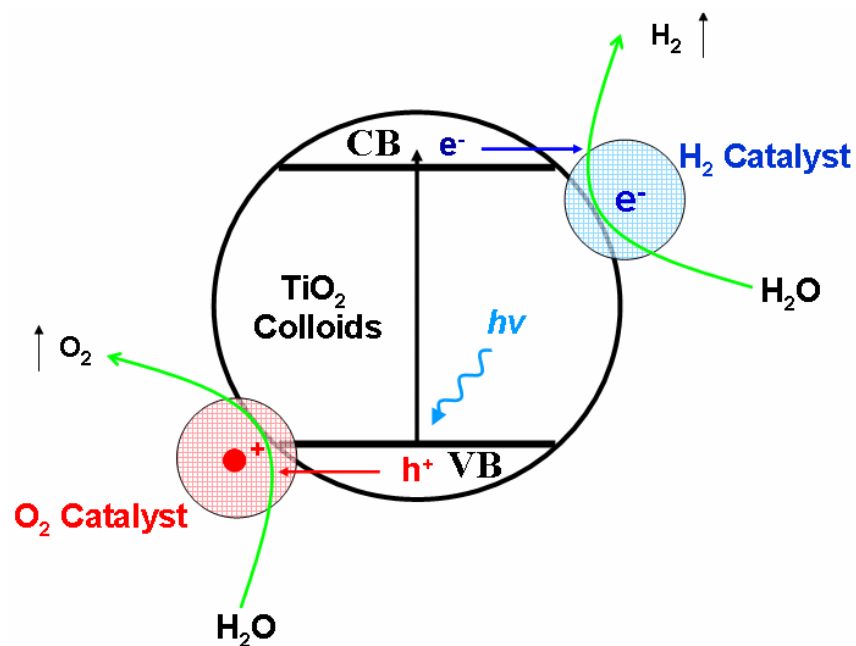
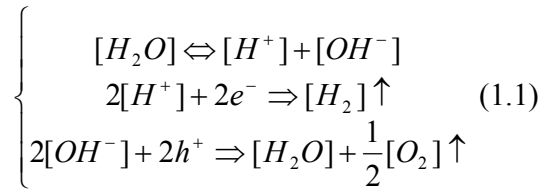


Figure 1.6 Photocatalysis of H₂O on a TiO₂ based composite catalyst.

Such a colloidal system behaves as a short-circuited nanophotocatalytic cell in which the metal H₂ catalyst is the cathode and the semiconductor O₂ catalyst works as the anode. The photoexcitation process generates an electron-hole pair across the bandgap of the TiO₂ colloid. The excess electrons in the conduction band (CB) of the colloidal TiO₂ transfer into H₂ catalyst, while the holes in the valence band (VB) are scavenged by O₂ catalyst. The presence of both H₂ and O₂ catalyst in the cathode or anode coupling with TiO₂ particle reduces the overall

electrochemical potentials for the redox pair significantly, so the trapped electrons in cathode reduce water to hydrogen while the trapped holes in anode oxidize water to oxygen. As is well known, the known fossil fuel energy resources on the Earth, especially the petroleum, will be depleted within this century, so how to obtain and store new sources of energy is serious problems facing mankind. The photocatalysis of H_2O on a TiO_2 catalyst system gives a convenient method to generate the H_2 , which represents a prospective source of inexhaustible clean energy.

Next, we introduce photovoltaic property of TiO_2 in a solar cell.

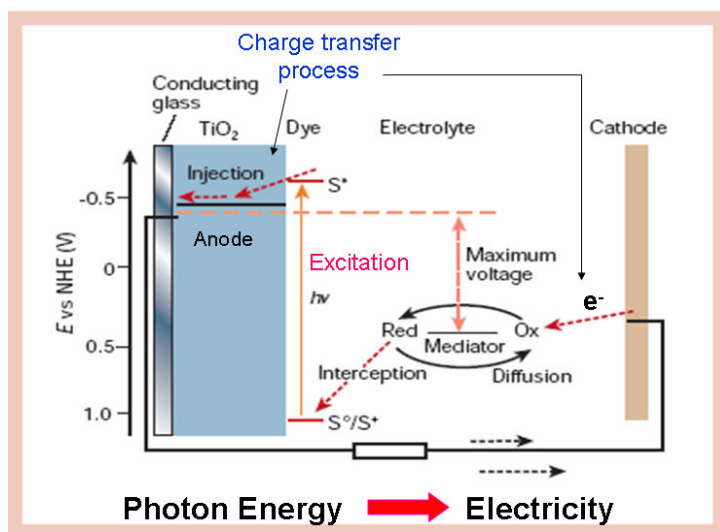
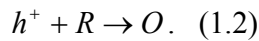


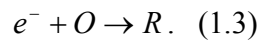
Figure 1.7 Schematic of the operation of a dye-sensitized TiO_2 solar cell [14].

Fig. 1.7 illustrates the main structure and operation of a dye-sensitized photovoltaic cell, also named as the regenerative Grätzel cell [14] in recognition of his pioneering work. Visible photons excite the dye molecules from the ground states (S^+/S) to the excited states (S^+/S^*),

generating electron-hole pairs in the surface space-charge layer. The negative charge carriers inject into the semiconductor conduction band (CB), move through the bulk to the current collector, then to the external circuit. The positive charges (holes) are driven to the surface and scavenged by the reduced form of the redox relay mediator (R/O) [5] in the electrolyte solution,



The oxidized form O is reduced back to R-form through a reversible process, where the electrons are re-entering the cell from the cathode electrode,



Typically, the redox pair of I_3^- / I^- is chosen to deliver charge from the cathode to the dye-molecules chemisorbed anode to complete the circuit. In Fig. 1.7, the mesoscopic nano-structured TiO_2 colloids are attached on a conducting substrate to form the anode electrode. The surface area with a porosity of 50% available for dye chemisorption is over a thousand times compared to a flat, unstructured electrode, allowing dye molecules adsorb most of the incident light.

One big advantage of TiO_2 based photovoltaic cells is their relatively high conversion efficiency (> 10%) and simplicity and cost of fabrication. Compared to the limited energy resources on the earth, the solar energy provides an infinite energy reservoir, and even collection over a small fraction of the Earth's surface can supply the human energy needs. TiO_2 based solar cells are

some of the most attractive candidates for solar-to-chemical and electrical energy conversion. However, due to the difficulty to find the stable dye molecules anchored on the mesoscopic TiO₂ nano-structures, and the challenge to further constrain the reverse charge transfer to achieve higher photon conversion current, the widely used commercial TiO₂ photovoltaic products are yet to come.

1.3 Application of Two-photon Photoemission (2PP) Technique to Molecule/TiO₂ System

The proposal of my thesis is not only to investigate the electronic structure of the bare TiO₂(110) surface, but also to explore the electronic structures of the adsorbate-covered surfaces. Such surfaces can exhibit molecular excited-state resonances, which participate in the heterogeneous charge transfer dynamics.

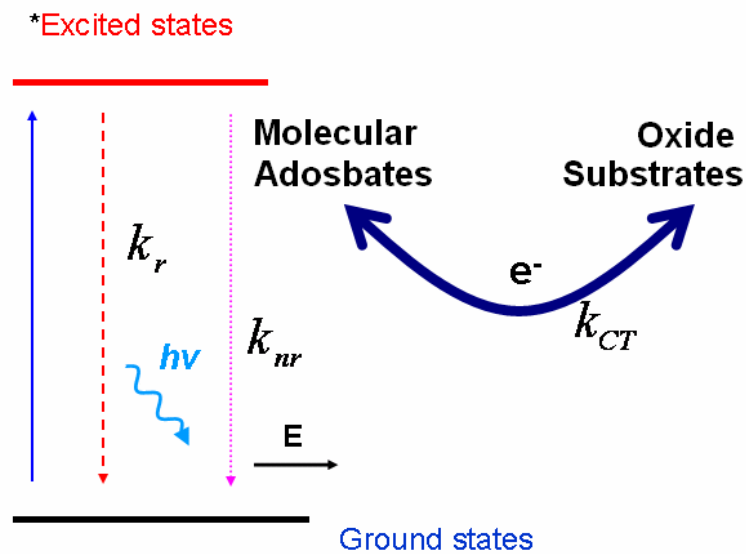


Figure 1.8 The electron transfer mechanism mediated by the molecular excited states, from the adsorbate overlayer to the oxide substrates.

For an isolated molecular system or molecules in the gaseous phase, the photons can induce an excitation transition from the ground state to the excited states. The excited electrons relax back to the stable ground state through radiative decay k_r , where an atom or molecule emits a photon by undergoing a downward transition conserving energy in the process (e.g. fluorescence) or non-radiative decay k_{nr} where the process does not involve the emission of a photon (e.g. inelastic energy transfer), and the decay time scales usually span from nanosecond up to millisecond time scales [19]. However, if the molecules are attached on an oxide substrate, and form a heterogeneous electronic system at the interface, there can be an additional ultrafast decay channel -charge transfer involving the injection of electrons to the conduction band and holes

into the valance band [20]. The charge transfer k_{CT} occurs in femtosecond to picosecond time scales at the adsorbates/oxide interfaces, establishing a much faster nonradiative decay process compared to the isolated molecules [21, 22]. Therefore, the femtosecond lifetimes of electronically excited states measured in our time-resolved photoexcitation are mainly determined by the interfacial charge transfer mechanism (in Fig. 1.8).

In Fig. 1.9, we show a typical time-resolved measurement used to explore the charge transfer mechanism from an aromatic adsorbate (bi-isonicotinic acid) to the TiO_2 substrate [23]. The energy alignment between the molecular states and the TiO_2 energy bands determines whether electron transfer into the conduction band is energetically feasible. The lowest unoccupied molecular orbital (LUMO) is located in the bandgap of the substrate, while the higher molecular states LUMO+1 and LUMO+2 have energy levels above the CBM of the substrate. So the charge transfer out of LUMO to the substrate is forbidden, but from LUMO+1 and LUMO+2 it is feasible. By combining the x-ray adsorption (XAS) illustrated in Fig. 1.9 and resonant photoemission spectroscopy (RPES) where in a core-excitation system, a valence electron fills the core hole, while another valence electron takes up the energy released in the former process and is ejected above vacuum level and measured (not shown), J. Schnadt et. al. measured the core hole decay rate and estimated the charge transfer from LUMO+1 state to the CB of TiO_2 occurs on a time scale of less than 3 fs [23]! This is the fastest reported time scale for an interfacial charge transfer process on oxides, however the results are obtained through an indirect measurement in the frequency domain.

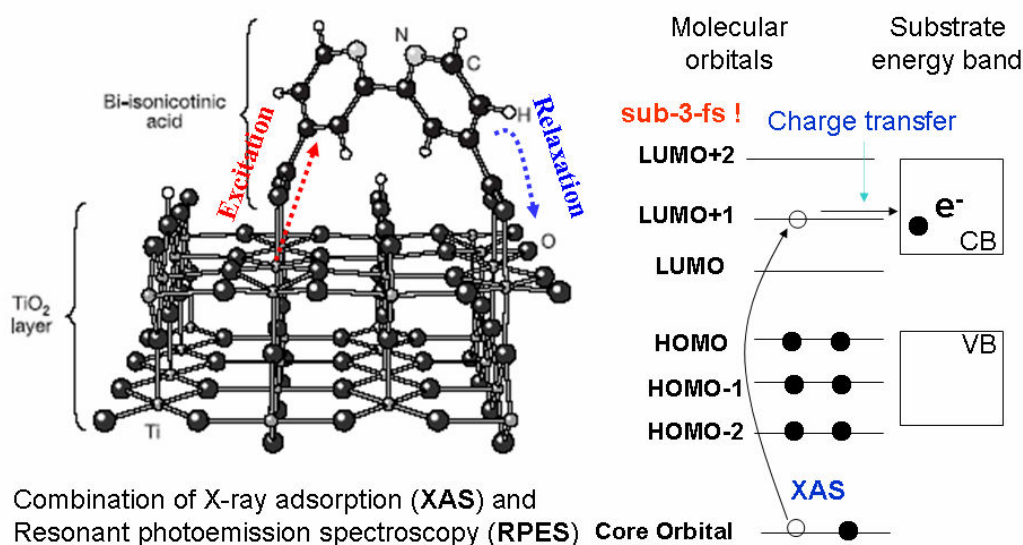


Figure 1.9 Charge transfer from the aromatic adsorbate to the TiO₂ substrate.

In another study, Rego and Batista performed molecular dynamics (MD) simulation for the electron transfer dynamics in the catechol/anatase system [24]. As illustrated in Fig. 1.10, the catechol molecule is anchored on the anatase TiO₂ surface, through two –CO– covalent bonds. Fig. 1.10 (a) shows the original orbital distribution of catechol LUMO+1. The calculated snapshots of the LUMO electron density in Fig. 1.10 describe the ultrafast charge transfer from the catechol molecular orbitals to the anatase substrate. The primary electron injection occurs within 6 fs through the –CO covalent bond to localize the charge on the Ti⁴⁺ ions next to the adsorbate molecule, then the isotropic delocalization of the injected charge occurs within the anatase crystal for the next 30 fs. Within ~12.5 fs time evolution, the LUMO+1 charge orbital distribution completely transferred to the anatase surface and started to disperse into the crystal bulk.

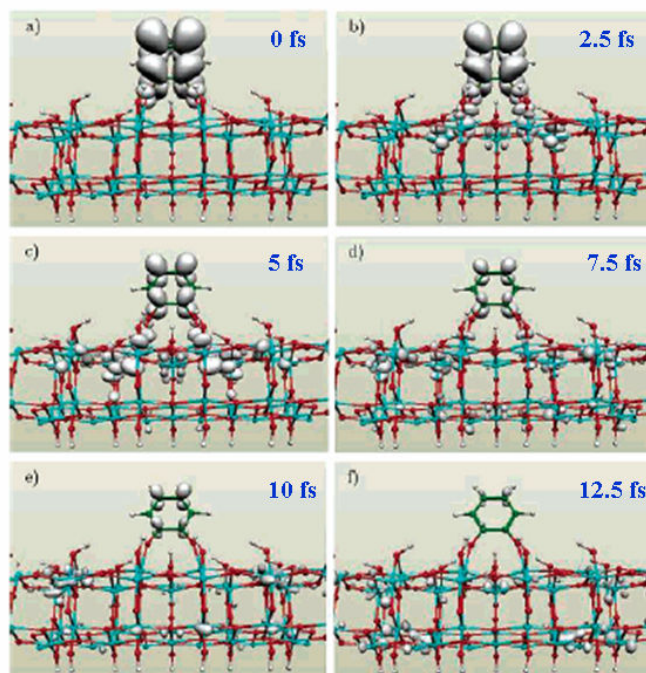


Figure 1.10 MD simulations for charge transfer in the catechol/anatase-TiO₂ structures.

From the previous discussion, we notice that the interfacial charge transfer at TiO₂ surfaces can be extremely fast, on the time scale of few femtoseconds! In order to measure the dynamical processes directly in the time domain requires an excitation laser source with extremely good time-resolution. Ti:Sapphire laser oscillator outputs a wide spectrum at the center wavelength of ~800 nm that supports femtosecond pulses (~10 fs) delivered with a typical repetition rate of 90 MHz [25].

The femtosecond laser pulses can be focused onto the sample surface and induce non-linear two-photon photoemission (2PP). A typical 2PP process is illustrated in Fig. 1.11, where the first photon (pump pulse) excites electrons from a bandgap state to an intermediate energy state, and the second delayed photon (probe pulse) further excites electrons from the intermediate state to above the vacuum level, where they can emit into vacuum [2]. One big advantage of the 2PP methodology compared with the single photon photoemission (1PP) as illustrated in Fig. 1.11 is that it can provide information not only on the DOS of the occupied electronic states below the Fermi energy E_F , but also that of the unoccupied states above E_F . Whenever the intermediate state is a virtual energy state, the 2PP maps only the occupied DOS in a same way as what 1PP does; on the other hand, when the intermediate state corresponds to a real molecular excited state, the 2PP intensities at the relevant energy levels would display the molecular resonance feature, which cannot be observed by 1PP spectroscopy [26]. Moreover, changing the arrival times between the pump and probe pulses enables us to record the dynamics of the intermediate state through the change of the 2PP intensities as a function of the time-delay. Analysis of the experimental time-resolved spectra, allows us to retrieve the time scales and mechanisms for various charge injection processes from the surface excited molecular states to the oxide substrate [2, 27].

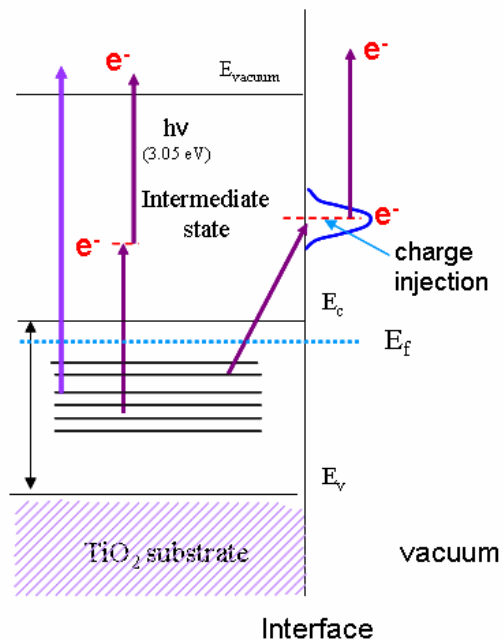


Figure 1.11 The 2PP process at TiO₂ surface and the charge injection between the surface molecules and the substrate.

Up to now, we have discussed the structure of TiO₂, its applications involving light, and the application of the femtosecond time-resolved two-photon photoemission (TR-2PP) technique compared to the conventional UPS methodology. These are the perspectives and tools for the study of the electronic structure and charge separation dynamics on molecule covered TiO₂ surfaces. In the following chapters, we will discuss the following topics: Chapter 2: the Experimental apparatus consisting of the excitation laser system and the UHV apparatus;

Chapter 3: the Fundamental theory of two-photon photoemission (2PP) process, including the methods for simulation of excited state electron dynamics [2, 27, 28]; Chapter 4: the 2PP investigation in the typical TiO₂ single crystal systems [29]; Chapter 5: Observation of “wet-electron states” at the H₂O/TiO₂(110) surface [30]; Chapter 6: Time-resolved studies of the ultrafast interfacial proton-coupled electron transfer dynamics in the CH₃OH/TiO₂ overlayer [31]; Chapter 7: Summary and Conclusions.

Chapter 2

Experimental Apparatus

In this Chapter, I discuss the major optical, vacuum, and electronic instrumentation used in the time-resolved photoemission experiment. Section 2.1, describes the ultrafast Ti:Sapphire laser excitation source; Section 2.2, the ultra high vacuum (UHV) apparatus; and Section 2.3, the diagnostic technology and the data acquisition process for the time-resolved photoemission experiment.

2.1 Laser Systems

The laser and optoelectronic systems are illustrated in Fig. 2.1. The optical system can be subdivided into three sub-units: 1) the Ti: Sapphire oscillator [32, 33], 2) the non-linear optical harmonic generation system [34, 35], and 3) the Mach Zehnder Interferometer [2]. They will be described individually in the following.

2.1.1 Ti:Sapphire Oscillator

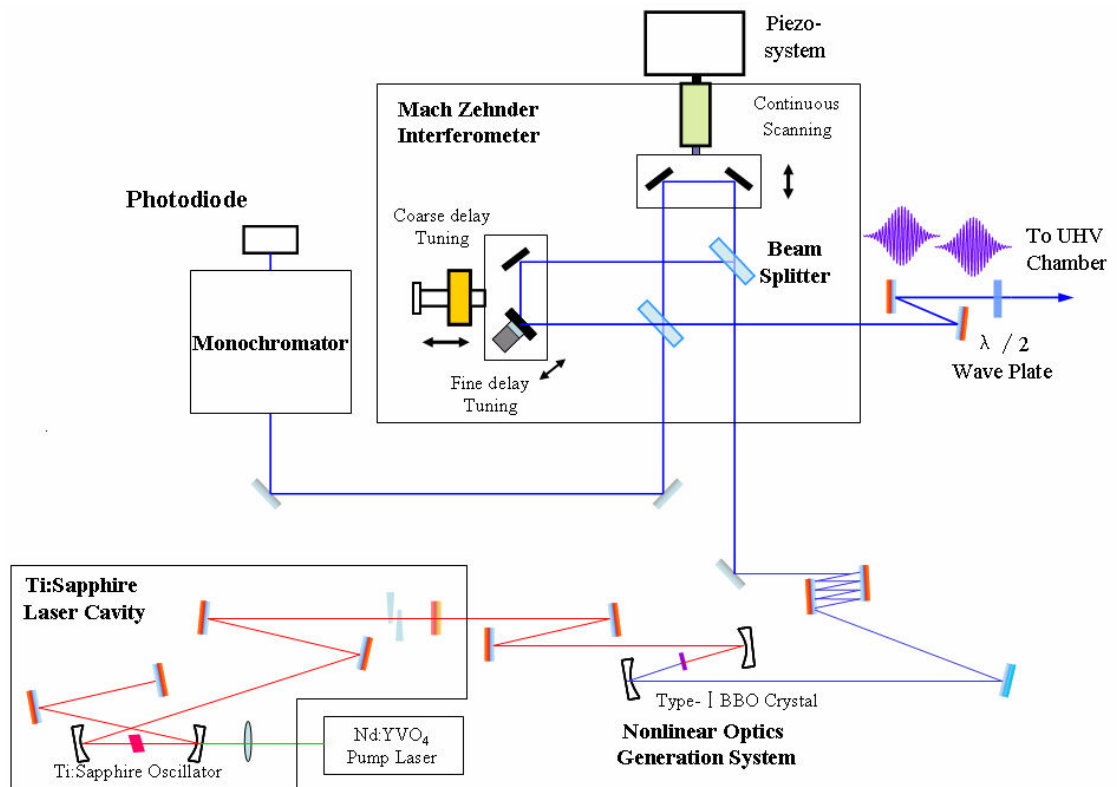


Figure 2.1 The optical system for the time-resolved photoemission experiment.

The left lower corner of Fig. 2.1 shows a schematic representation of the ultrafast Ti:Sapphire Laser cavity constructed in our laboratory. A commercial continuous wave (CW) solid state laser (Millennia Xs from Spectra Physics) is used as a pump for the Ti:Sapphire laser. Approximately 5 Watts output power of continuous green light at 532 nm incident at the Brewster's angle is

focused with a 50 mm focal lens onto the Ti:Sapphire crystal [36]. The resulting ~800 nm emission is amplified to generate a coherent beam with p-polarization, i.e. the transverse magnetic (TM) mode [37].

To generate a mode-locked fs laser pulses requires the oscillation of a large number of longitudinal modes underneath a broadband gain medium. In absence of mode-locking, corresponding to a CW operation in time domain, some of these different modes oscillate within the laser cavity independently. The term “mode-locking” refers to the procedure of forcing all the modes to oscillate with the same phase, so that all the waves of different frequencies add constructively at certain point in time, resulting in a very intense and short burst of light. In our laser system, we adopt self-phase modulation (SPM), which occurs via the 3rd order nonlinear interaction of a rapidly varying optical field of the laser pulse with the nonlinear intensity-dependent change in the refractive index of an optical material [38] to induce the mode-locking for various longitudinal modes. The nonlinear index change induces transient lens effect (Kerr effect) in the gain crystal. The Ti:Sapphire oscillator delivers an optimal pulse of ~10 fs time duration, with a repetition rate of around 90 MHz and an output power of ~650 mW.

2.1.2 Non-linear Optics

The photon energy of ~1.55 eV from the 800 nm laser is not sufficient to excite two-photon photoemission from typical metal or semiconductor surfaces. With typical work function of 4 ~ 5

eV [39], the minimum practical energy to excite 2PP and to observe the unoccupied electronic structure of the sample in a sufficiently large energy range corresponds to at least the second harmonic of the Ti:Sapphire oscillator. Even higher photon energies are desirable to study the electronic structure or dynamics of image states on metal surfaces [40], or the conduction bands of wide bandgap (~ 3 eV) semiconductors [41-43]. In this section, we describe the second order harmonic generation process [38], where the nonlinear optical susceptibility of a crystal is exploited to double the laser frequency or energy.

The second harmonic conversion efficiency of a non-linear optical crystal is described by [38]:

$$\frac{P^{(2\omega)}}{P^{(\omega)}} = 8 \left(\frac{\mu_0}{\epsilon_0} \right)^{3/2} \frac{\omega^2 (d_{ijk})^2 L^2}{n^3} \left(\frac{P^{(\omega)}}{Area} \right) \frac{\sin^2(\Delta k \cdot L / 2)}{(\Delta k \cdot L / 2)^2}, \quad (2.1)$$

where L is the effective conversion length in the crystal, d_{ijk} is the appropriate non-linear susceptibility tensor element for the incoming fundamental and outgoing second harmonic waves of specific polarization, and Δk is the wave vector difference between the fundamental and the second harmonic waves. In order to optimize the conversion efficiency, the non-linear crystal should be used under the phase matching condition where,

$$\Delta k = k^{(2\omega)} - 2k^{(\omega)} = \frac{2\omega}{c/n^{2\omega}} - 2 \frac{\omega}{c/n^\omega} = \frac{2\omega}{c} (n^{2\omega} - n^\omega) \quad (2.2)$$

In Fig. 2.2, we describe how to achieve the optimum phase matching condition $\Delta k = 0$ when $n^{2\omega} = n^\omega$ in a negative uniaxial birefringent crystal, where the extraordinary beam of the second

harmonic (blue dash oval) has a smaller index compared with the ordinary beam of the fundamental light (red solid circle), i.e. $n_e^{2\omega} < n_o^\omega$. In the diagram, when the red light with polarization vector normal to the plane of paper and blue light with a polarization lying in the plane of paper are propagating collinearly at an angle θ_m with respect to the optical axis, the indices of refraction $n(\theta_m)^{2\omega} = n_o^\omega$ for the two beams are the same, and the phase matching condition is achieved.

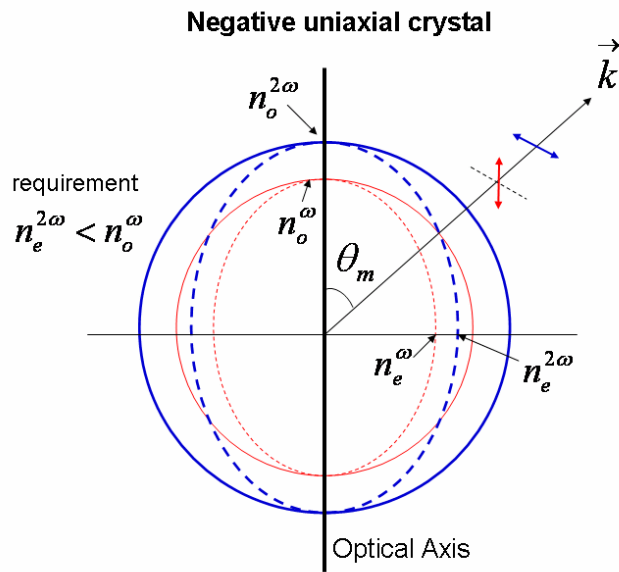


Figure 2.2 The phase matching condition for a negative uniaxial non-linear optical crystal.

From Eqs. 2.1, we can see that the incident power per unit area is also a very important factor for the efficient non-linear conversion. In Fig. 2.3, we describe the optical system for the second harmonic generation (SHG) in our lab employing type-I phase matching in β -BBO crystal, where the type-I phase matching is defined as: two input laser beams (ω_1 and ω_2) with parallel polarization (e.g. parallel or perpendicular to the optical axis), are converted to a sum-frequency of frequency-doubled output beam $\omega_3 = \omega_1 + \omega_2$ with orthogonal polarization (Fig. 2.3). A pair of spherical concave reflection mirrors with 50 mm focal length is used to focus the fundamental beam into the crystal to achieve high conversion efficiency and deliver second harmonic light with transverse electric (TE) mode and adjustable focusing. The reflection mirrors are mounted on and manipulated by optical translation stages in order to reach the best focusing as judged by the optimized SHG conversion efficiency. Especially, the BBO crystal is mounted on a gimbal mount, which allows for rotation along the tuning axis in order to maximize the SHG output power or to tune the output wavelength of a broad band input pulse through changing the phase match angle θ .

$$\frac{1}{(n_e^{2\omega}(\theta))^2} = \frac{\cos^2 \theta}{(n_o^{2\omega})^2} + \frac{\sin^2 \theta}{(n_e^{2\omega})^2} = \frac{1}{(n_o^\omega)^2} \quad . \quad (2.3)$$

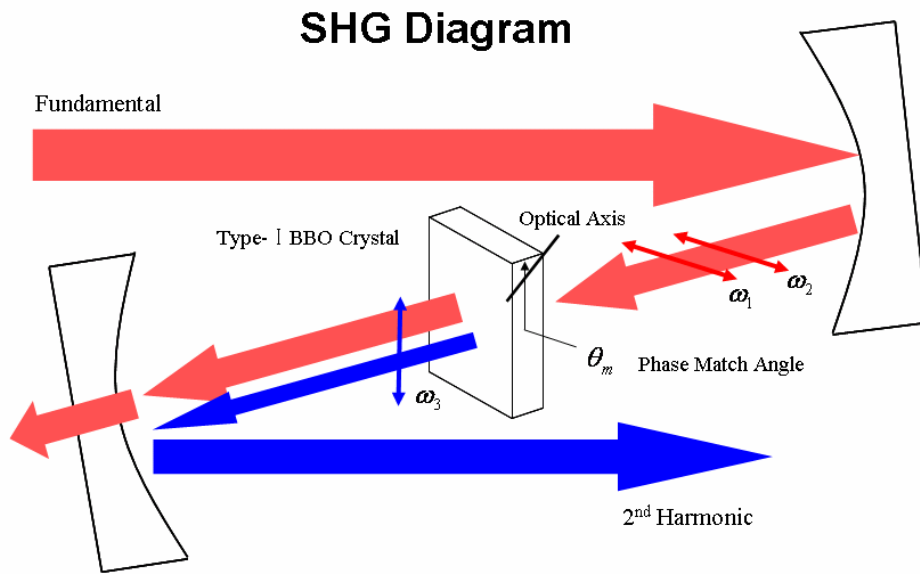


Figure 2.3 The diagram for the Type I SHG generation with a BBO crystal and where θ is defined in the formula:

In Fig. 2.4, we compare side-by-side the spectra of the fundamental laser output at the exit of the cavity and its second harmonic generated by the SHG optical system. The fundamental includes both a broadband of mode-locked femtosecond pulse component and a sharp Raman scattering component that is often observed in <10 fs laser pulses. The second harmonic spectrum displays near ideal Gaussian shape with a central wavelength at 395 nm.

The predicted pulse width (FWHM) of each mode-locked laser pulse due to the

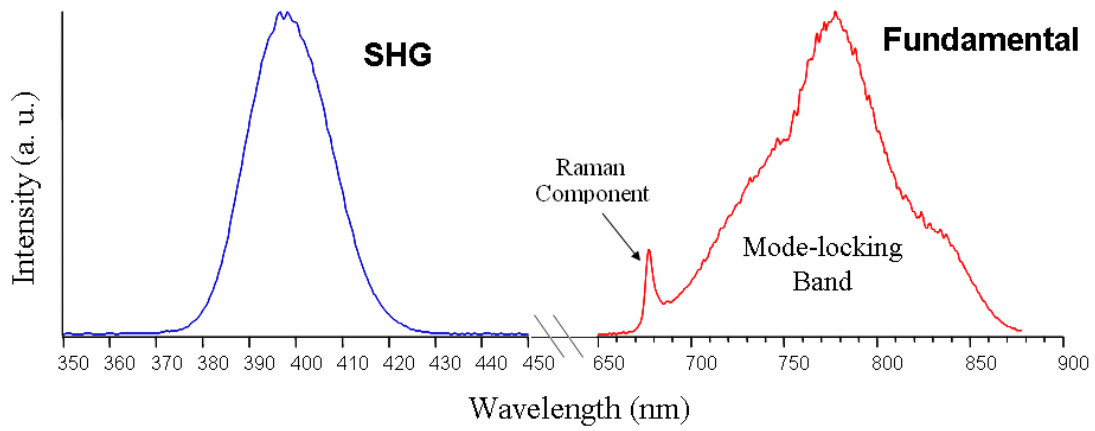


Figure 2.4 The fundamental and second harmonic spectra of the Ti:Sapphire laser.

Heisenberg uncertainty law, can be as short as the reciprocal of the emission frequency line band width

$$\Delta\tau = \frac{1}{\Delta\nu}, \quad (2.4)$$

Where the gain bandwidth is $\Delta\nu = \frac{c \cdot \Delta\lambda}{\lambda^2}$.

Using a central wavelength of 800 nm along with a wavelength bandwidth ~ 150 nm of the fundamental component of our Ti:Sapphire laser in Fig 2.4, the estimated pulse width is calculated as:

$$\Delta\tau = \frac{1}{\Delta\nu} = \frac{\lambda^2}{c \cdot \Delta\lambda} = \frac{(800 \cdot 10^{-9})^2 \cdot m^2}{3 \cdot 10^8 \cdot 150 \cdot 10^{-9} \cdot (m/s) \cdot m} \approx 14(fs). \quad (2.5)$$

This shows a femtosecond pulse can be achieved experimentally through a broad band gain emission profile.

2.1.3 The Variable Time-delay Generation with a Mach-Zehnder Interferometer

This section describes the Mach-Zehnder Interferometer for generation of identical phase correlated pump-probe pairs for the probing ultrafast electron dynamics in two-photon photoemission measurements.

The main structure of the Mach-Zehnder Interferometer (MZI) is shown in the upper part of Fig. 2.1. Inside the MZI, two broad band beam splitters designed for 50% reflection of s-polarized 400 nm light at 45° incidence separate and recombine a single pulse into a collinear pulse pair. One of the optical paths is fixed, while the other is scanned with a piezoelectric actuator to generate variable time delay between the pump and probe pulses. The MZI has two light outputs. The path for which the dispersion is balanced is used for the 2PP measurements, while the unbalanced part is used for the scan delay calibration. The calibration procedure will be described in the section 2.3.

Before entering the photoemission chamber, the excitation light passes through a $\lambda/2$ wave-plate to select p- or s-polarization. A differentially pumped CaF₂ lens with a nominal focal length of 200 mm mounted on the UHV chamber focuses the excitation light onto the sample and simultaneously serves as transparent vacuum seal. The focus size on the sample is estimated to be less than 100 μ m.

2.2 The UHV Chamber and Electronic Instruments

Time-resolved photoemission measurement are performed in a UHV chamber with a base pressure of $<1.0 \times 10^{-10}$ mbar. Gases to be adsorbed on the surface such as O₂, H₂O or CH₃OH can be introduced into the chamber by back-refilling method through a leak valve.

2.2.1 Overview of the UHV System

The schematic diagram of the UHV system for our experiment is shown in Fig. 2.5. The sample is mounted at the end of a custom UHV manipulator. The manipulator has the capability of 3D translation and rotation involving a differentially pumped stage. The manipulator is used to position the sample and to perform various functions such as Ar⁺ sputtering, e⁻ irradiation, adsorption of molecules, and photoemission measurements. The manipulator has a hollow center

with a Helium flow cryostat. However, it is mostly cooled with liquid nitrogen. The sample heating is accomplished through electron bombardment. When applying high voltage (~ 1 KV) with respect to the sample transfer plate, the electrons evaporated from a coiled tungsten wire, which is heated by passing a filament current of ~ 2 A, are accelerated into the transfer plate. The final sample temperature depends on the magnitude of both the acceleration potential and the electron emission current. Using the combination of liquid N_2 cooling and the electron bombardment heating, we can control the sample temperature from 85 up to 1000 K.

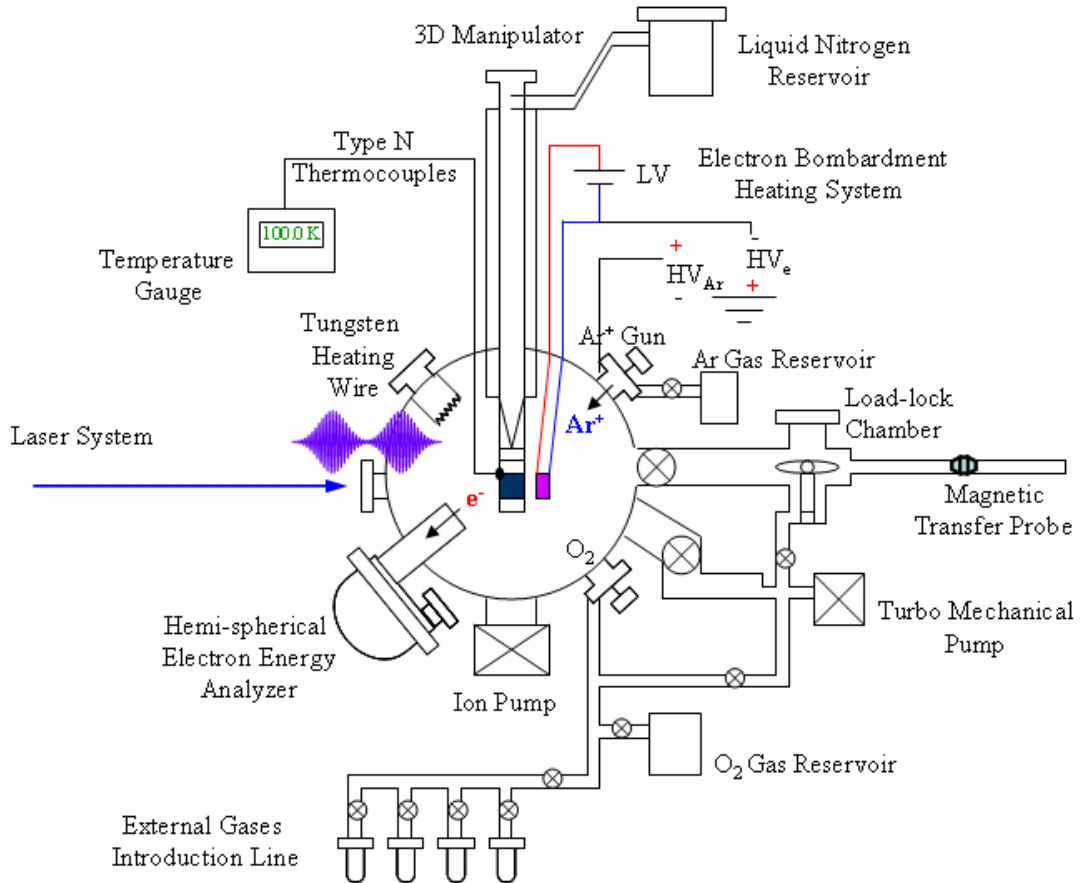


Figure 2.5 Overview of the UHV System.

The TiO₂ sample is clamped at the upper and lower edges by two flexible molybdenum springs and mounted onto the transferable sample plate. In order to measure the temperature in a wide range, an N-type thermocouple, which is made of a nonmagnetic material, is spot welded onto a fixed spring that holds the aforementioned sample plate. The UHV system is designed to allow for the transfer and storage of multiple samples. The load-lock chamber in Fig. 2.5 is separated from the main chamber by a gate valve, and has a rotatable sample holder, which is capable of storing up to 6 samples.

The main experimental measurement system in our UHV apparatus is the hemispherical energy analyzer (at lower left of Fig. 2.5). Its main function is to collect the photoemitted electrons from the sample surface, and to perform their energy and momentum analysis. The UHV apparatus is pumped by a combination of rotary vane pump, turbomolecular pump, VARIAN ion pump and Titanium sublimation pump [44]. The center part of the rotary vane pump is a steel cylinder rotator, which can rotate to pump out air through compression-expansion of the gas volume. The turbomolecular pump contains alternative rotating and stationary discs and plates, where the discs and plates of each are cut to form angled flaps. The rotary motion of one set of discs and plates can generate a projected force to drag the molecules moving towards the stator, then out of the system. These two kinds of pumps can usually evacuate the chamber from atmospheric pressure to intermediate vacuum level $\sim 1 \times 10^{-6}$ mbar. The VARIAN ion pump applies an extremely high voltage (~ 3 KV to 7 KV) between its anode and cathode. The molecules moving

between the electrodes are ionized and accelerated into the cathode where they are trapped. The ion pump can generate the ultra high vacuum level to $\sim 1 \times 10^{-10}$ mbar from the intermediate vacuum condition. Moreover, we also have a Ti-sublimation pump installed in our vacuum system. Activation of the pump evaporates Titanium getter material, which effectively adsorbs reactive gases. Practically, the Ti-sublimation pump operates intermittently to reduce the residual gas level significantly within a short period.

Finally, we describe the method for introducing molecular adsorbates onto the sample [44]. At the bottom division of Fig. 2.5, we show an oxygen reservoir and several inlets for introducing chemicals into the vacuum system. The oxygen gas is essential for preparing a well-defined stoichiometric TiO_2 surface. The other chemicals can be introduced into the UHV chamber in the gas phase through a leak valve by back filling method [45, 46]. Molecules are chemisorbed onto the sample surface by reducing the sample temperature to typically 90-100 K to form stable overlayer structures to be used in photoemission measurements. The oxygen reservoir and the other external gas reservoirs share a same introduction pipe, which is connected to turbomolecular pump through Swagelok gate valves. When the valves are open, the turbomolecular pump can evacuate the residual gases while the pipes and the manifold are baking; after the manifold is evacuated, new types of gases can refill the manifold and be introduced into the chamber.

2.2.2 The Hemispherical Electron Energy Analyzer and the Channeltron Detector

The Omicron-125 hemispherical electron energy analyzer with an inner radius of 125 mm is the heart of our UHV system. It is composed of two concentric electrostatic hemispherical shells. The photoemitted electrons from the source are collected by an electrostatic Universal Lens System (not shown), employing a design of two sequential lenses, and focused onto the entrance aperture of the analyzer.

The first lens of the electrostatic input universal lens system is the Einzel lens, which anchored in the analyze collection tube, the lens can be operated in three discrete magnification modes: high, medium and low. In high magnification mode, the focal plane is near to the sample and the lens accepts a wide cone angle of emitted electron from a small sample region. In the low magnification mode, the focal plane is further from the sample and the lens accepts only a narrow cone angle but from a larger area. The medium magnification mode is intermediate. The angular acceptance or angular resolution is solely determined by the magnification mode of the Einzel lens. In our photoemission measurement, we usually use “Low Magnification Mode” to reach the angular resolution as high as $\pm 1^\circ$. The second lens mainly adjusts the kinetic energy of the electrons, retarding or accelerating them to match the pass energy V_0 of the analyzer while preserving the electron energy distribution that existed before entering the lens system, and

employing a zoom lens function to ensure the focal point remains on the analyzer entrance aperture.

The trailing edge of the input lens system is directly connected to the entrance aperture of the hemispherical energy analyzer. Its dimensions are variable to satisfy the various requirements for momentum or kinetic energy resolution of electrons traveling between the two hemispheres of the analyzer. As shown in Fig. 2.6, our energy analyzer is able to work in a multi-channel mode. Electrons with an average energy V_0 follow slightly different trajectories between the hemispherical plates depending on their energy dispersion. At the exit slit of the hemispherical analyzer, the energy dispersed electrons are collected by an array of seven channeltron detectors. Similar to the entrance slit, the size of exit slit is also changeable: a larger size gives correspondingly higher signal intensity, but with worse energy resolution. The photoelectron currents at different energies are recorded as parallel photoemission spectra, which are combined into a single spectrum after parallel channel acquisition.

A remaining essential question is how to estimate the energy resolution. Here we use a simple formula to perform an approximate calculation,

$$\Delta E = E_p \cdot \left(\frac{d}{2R_0} + \alpha^2 \right), \quad (2.6)$$

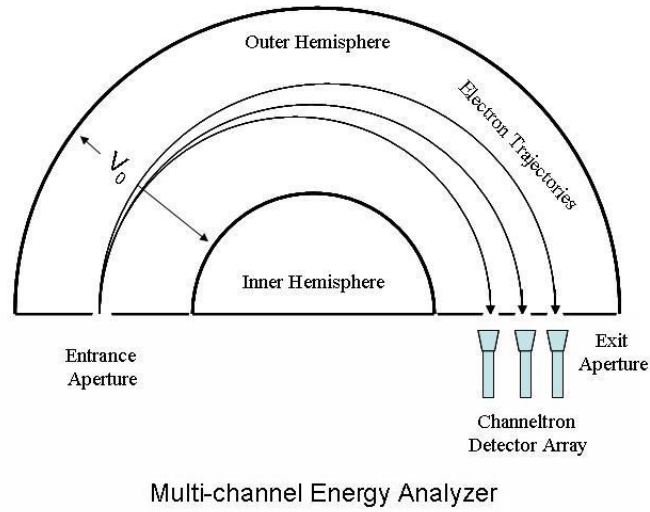


Figure 2.6 The diagram of the multi-channel energy analyzer.

where E_p is the pass energy of the analyzer (typically $E_p = V_0 = 5$ eV), d is the entrance slit width being used (~ 1 mm), R_0 is the mean radius of the hemisphere (~ 125 mm), and α is the half-acceptance angle of electrons entering the analyzer in radian units (in the “Low Magnification” mode, $\alpha \sim 1^\circ \approx \frac{\pi}{180}$). Under these conditions, the energy resolution can be as good as < 20 meV.

The signal intensity that is the electron count rate at the analyzer exit aperture is pretty low, especially from semiconductor surfaces like TiO_2 with a low DOS at the Fermi level. Usually, a channeltron is used as a single electron amplifier so that it is possible to count the single electron events. In Fig 2.7, we use a cartoon to show how electron amplification process occurs in a channeltron. Primary electrons that enter the channeltron with kinetic energy distribution at the

pass energy (~ 5 eV) are accelerated within the inner core of the channeltron by a bias of 1.2 \sim 1.5 KeV to generate several secondary electrons out of the emissive materials. As traveling down along the channeltron, those secondary electrons have been through several steps of serial amplification. Therefore, a single electron is amplified by a factor of 10^8 to a fast current pulse. Those fast current pulses are output to feed into a fast preamplifier. From there, the current pulse is further delivered through various electronic devices onto a pulse counter for processing. The further details relevant to this topic will be addressed in later section.

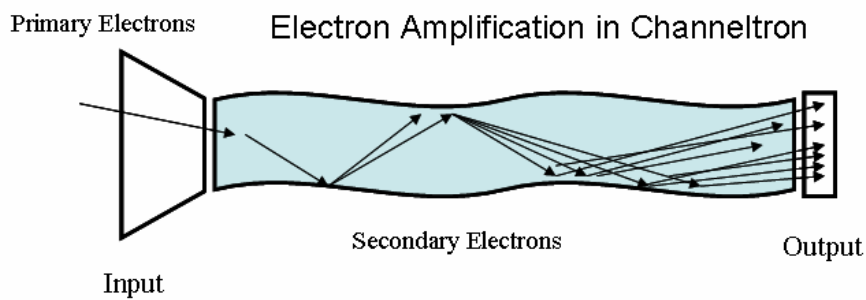


Figure 2.7 Single electron amplification in a channeltron.

2.2.3 The Fundamentals of Photoemission Experiments

The body of the electron energy analyzer is mounted to the main chamber wall, sharing the same electrical ground. The inner surface of the energy analyzer is coated with a layer of graphite to give a uniform work function of 4.5 eV. The photoemission sample is isolated electrically from the main chamber wall at the tip end of the cryogenic storage system by a sapphire plate, which

is an electrical insulator with a volume resistivity 10^{14} Ohm-cm, and a good thermal conductor with approximately constant thermal conductivity $0.065 \text{ cal cm}^{-1} \text{ s}^{-1} \text{ }^\circ\text{C}^{-1}$ at various temperatures. The electrical isolation allows us to directly apply a bias voltage of several Volts between the sample and the analyzer, which can enhance the capture of low energy electrons and the S/N ratio. In Fig. 2.8, we describe schematically a two-photon photoemission measurement for a typical wide bandgap semiconductor such as TiO_2 . The photoexcitation can occur from the occupied to unoccupied states. The bandgap of TiO_2 is $\sim 3 \text{ eV}$ and the work function is $4.4 \sim 5.8 \text{ eV}$ [47, 48]. The combined energy of two photons (6.1 eV) is not sufficient to excite the valence band electrons to above the vacuum level E_{vac} , so the photoemission is mainly contributed by the DOS of the bandgap energy states. The reference energy level (zero energy) for 2PP measurements is the Fermi level of the sample as convenience (Fig. 2.8).

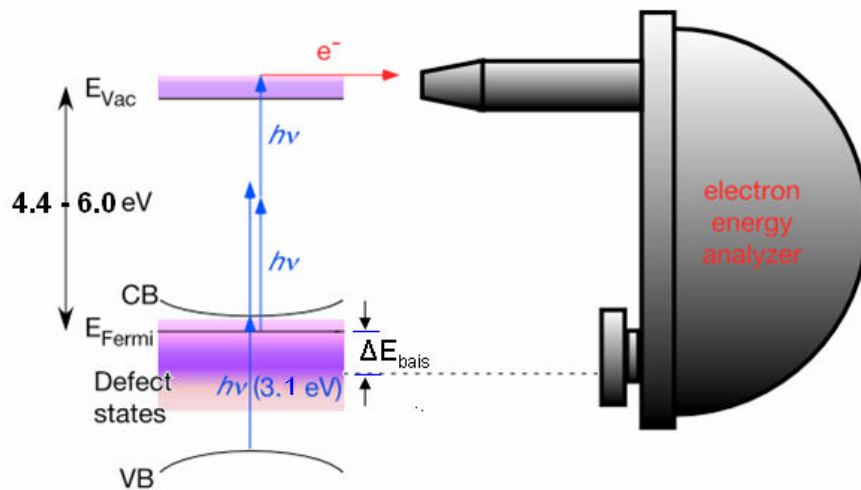


Figure 2.8 The schematic diagram of a 2PP measurement for a wide bandgap semi-conductor (TiO_2), and the energy alignment of the sample and the electron energy analyzer.

2.3 Data Acquisition and Diagnostic System

In this section, we give a detailed description of the data acquisition process and the optoelectronic devices used in our two-photon photoemission experiment.

2.3.1 Overview of the Data Acquisition System

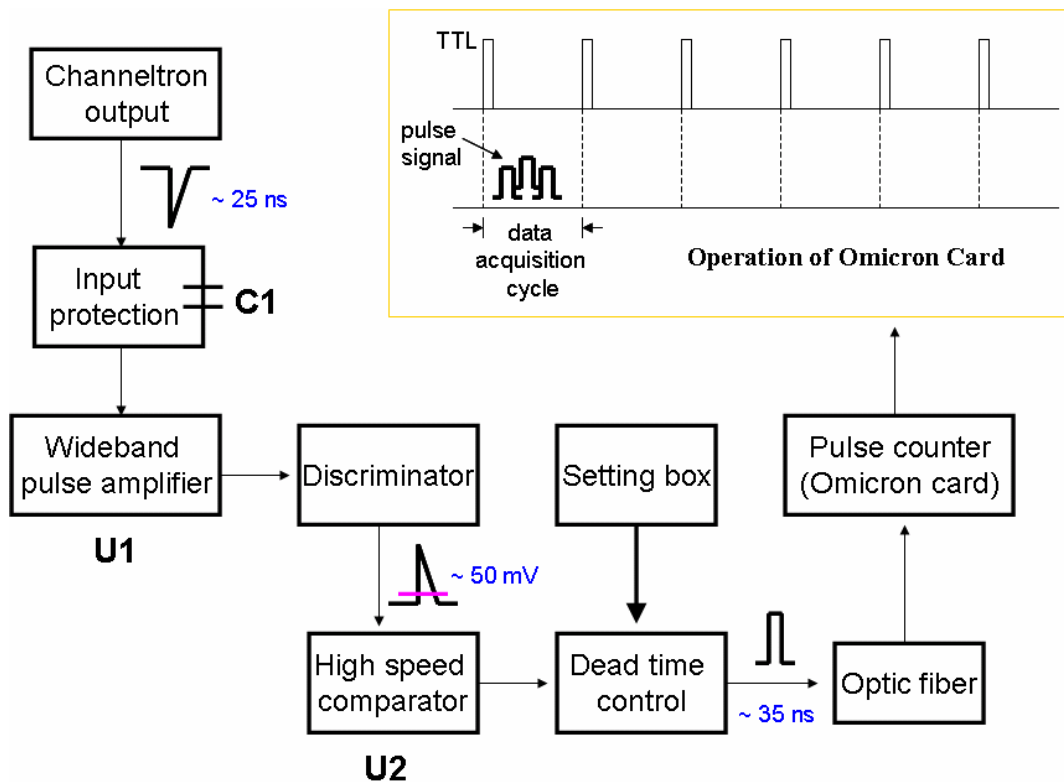


Figure 2.9 Overview of the electronics for data acquisition system.

In Fig. 2.9, we present the outline of the data acquisition and control electronics used in our experiment. The single photoelectron event transmitted by the hemispherical energy analyzer is

detected and amplified as an electron pulse by the channeltron detector. Those output pulses from the channeltron are passed through an input protection device, implemented a capacitor C1, which is used to isolate the high voltage (1.2~1.5 KV) of the channeltron multiplier and maintain the electron pulses having amplitude in the region of 300 mV to 1.3 V and time duration of ~ 25 ns. Afterwards the pulsed signals are further amplified by a wideband pulse preamplifier U1 and the outputs of the wideband pulse amplifier are delivered through a discriminator, whose threshold level is usually set as 50 mV to discriminate the true electron detection events from noise. Thereafter, the pulse signal is converted to a digital signal and sent into a high-speed comparator U2 and the dead time control system. The pulse width generated by the dead-time control actually depends on parameter settings. For example, the default settings are: 35 ns pulse width along with 70 ns dead time. Then the pulses are sent through the optic fiber to Omicron pulse-counter, where a computer card count the pulse events in a time interval that is defined in software (usually 0.5 s in spectroscopic measurements and 150 μ s in time-resolved measurements). The operation of the Omicron card is also briefly outlined in Fig. 2.9 as well. Triggered by a series of TTL signals, the Omicron card starts to count the number of signal digital pulse events in a data acquisition cycle. When the next TTL signal comes, it clears the memory and proceeds the counting for the next interval. More details regarding to the data acquisition along with the participation of Omicron computer board will be discussed in our time-resolved measurement section.

2.3.2 Spectroscopy and 7-channel Data Acquisition

According to the discussion in the previous sections, we illustrate a complete picture of photoemission measurement and data acquisition process: the photoelectrons are measured by

the hemispherical energy analyzer, and detected at different energies by an array of 7 parallel channeltron detectors. The signals for each channel are counted and processed separately by the Omicron computer card, as explained above, and are stored as a separate data-flow in the PC and displayed either as separate spectra, or summed spectra by the acquisition software. In Fig. 2.10, a screenshot of EAC software window is given, showing individual spectra along with the acquisition parameters in the 7-channel acquisition mode. The detailed information regarding to the spectroscopic parameters in Fig. 2.10 is given in Appendix A.

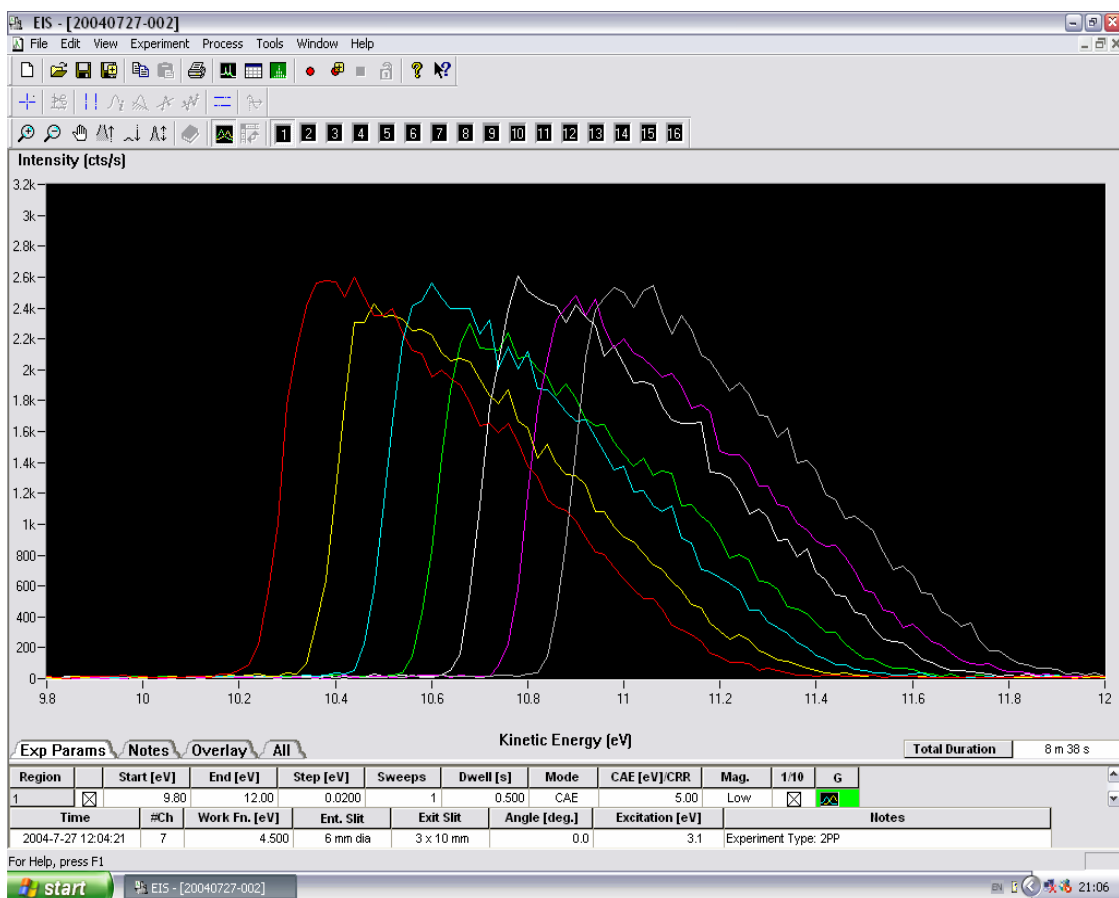


Figure 2.10 the screenshot of the software window during a 7-channel data acquisition.

2.3.3 Time-resolved Dynamics Measurement and Signal Synchronization

The previous section discussed the data acquisition for a typical spectroscopic measurement. We also acquire data in a time-resolved mode that is particular to our experiment. The operation of the dynamic data acquisition process is outlined in Fig. 2.11: the PC performs all the control and acquisition functions.

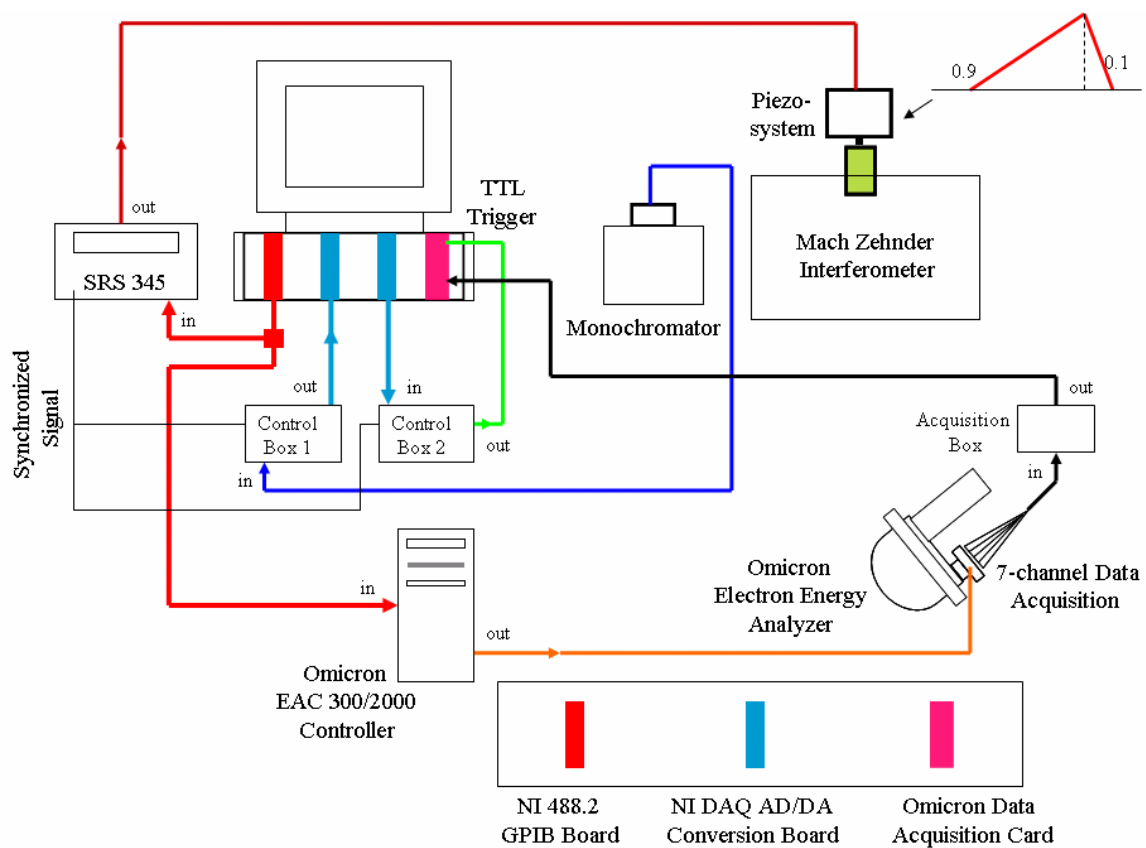


Figure 2.11 The electronic system for the interferometric two-pulse correlation measurements.

In a time-resolved measurement, the PC sends a command through the GPIB board to a Stanford Research Systems SRS345 arbitrary functional generator, which outputs a vector waveform (sawtooth wave) to the piezoelectric system control electronics. The signal is amplified and supplied to the piezo-actuator in order to scan a flexure stage in the Mach-Zehnder Interferometer. The translation of a pair of mirrors on that stage by $\pm 30 \mu\text{m}$ provides a variable delay of ± 200 fs. The scanning is performed continuously in synchronization with the data acquisition. From section 3.1.3, the MZI has two output components: one is delivered to the sample in the UHV chamber to work as the photoexcitation source, the other is sent into a monochromator to optimize the beam alignment and calibrate the time-delay. The monochromator takes the broadband input light and selects a single frequency (usually the spectral intensity maximum) that is detected with a photodiode. The effect of narrowing the spectrum is that the ~ 10 fs input pulses are stretched to the picosecond time scale. As a result, the pump and probe pulses at the output of the monochromator overlap in space and time throughout the delay scan, and the optical interference between the pulses provide sinusoidal signal where one period corresponds to one optical cycle of the monitored light (Fig. 2.12).

The scan is performed repeatedly with a saw tooth waveform with a frequency of ~ 1.34 Hz. Synchronously, the photodiode voltage is read every $150 \mu\text{s}$ by an A/D board corresponding to a typical delay interval of < 0.1 fs per data point. In Fig. 2.11 we show how this operation is performed: the PC sends a command to one of the A/D-D/A boards, requesting the control box 1

to acquire analog interfering fringes from the photodiode. The digitized waveform is then stored into different time bins. Since displacement of the piezoelectric actuator is non-linear with the input voltage, the recorded fringes are used to linearise the time axis and determine the phase of the coherent photoemission signals. Simultaneously, another A/D-D/A board sends a TTL signal

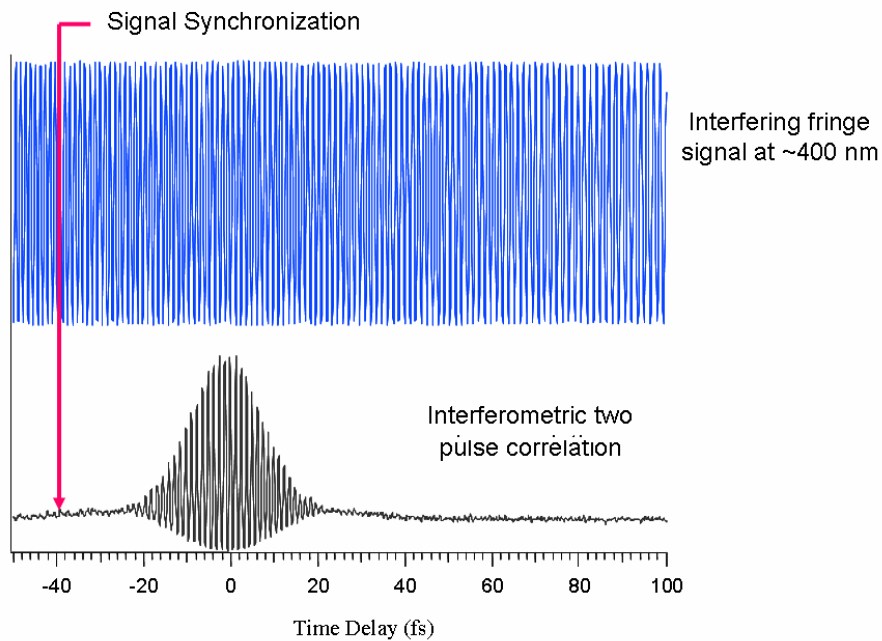


Figure 2.12 Signal synchronization between the calibration interference fringes and the two-pulse correlation signals.

to the control box 2 to trigger the Omicron data acquisition board to start counting the photoelectron counts for each of the 7 channels. The counts are summed for the same time interval as for the reference fringe signal (150 μ s). The counts for each pump-probe scan are

summed with those of the previous scans for the same interval in order to acquire an interferometric two-pulse correlation trace of two-photon photoemission. Because the acquisition of the interference fringes and photoelectron counts are synchronized in the data acquisition (Fig. 2.12), we can obtain very precise delay time and phase information that is essential for performing <10 fs time resolution polarization and population dynamics measurements. Also, the 7-channel acquisition mode allows us to compare dynamics under exactly the same conditions for different measurement energies. The details of the interferometric pump-probe measurement control software are given in the Appendix B.

Chapter 3

2PP Background

This chapter will cover the fundamental physical processes involved in a time-resolved two-photon photoemission (TR-2PP) process [26, 41, 49]. Time-resolved photoemission spectroscopy [2] is one of several techniques that has developed in recent years for studying ultrafast charge carrier dynamics with a unique capability of directly observing electrons with specific energy and momentum within the skin depth of a solid surface [40, 50-53]. It is the primary method in our project for investigation the electron solvated and charge transfer dynamics [54-56] in molecular overlayers on metal-oxide surfaces [30, 31]. The main advantage of 2PP methodology is that it can be used to study the electronic structure and dynamics of materials in otherwise unoccupied states.

3.1 Hot Electron Dynamics

3.1.1 Laser Pulse Induced Electron Distribution at the Intermediate Unoccupied States

Fig. 3.1 describes the electronic structure of both the occupied and unoccupied states for a typical metal surface. In a two photon photoemission (2PP) process, the photoexcitation can

populate the originally unoccupied states and modify the electron distribution by further exciting to higher energies. Considering an energy E above the Fermi level but below the vacuum level, the pump laser $\hbar\omega_1$ changes the electronic distribution by populating E from a lower energy level $E - \hbar\omega_1$ and by depopulating E in the next step by inducing excitation to a higher energy state $E + \hbar\omega_1$. This final state is usually a free electron state above the vacuum level. Therefore, the total contribution of the laser excitation to the electronic distribution at the intermediate energy level E can be approximately described as:

$$H(k,t) = A \cdot I_p(t) \times [D(E - \hbar\omega_1)f(E - \hbar\omega_1)(1 - f(E)) - D(E)f(E)(1 - f(E + \hbar\omega_1))], \quad (3.1)$$

where $I_p(t)$ is the photon flux, $D(E)$ the density of states (DOS), and $f(E)$ the Fermi-Dirac distribution function [57].

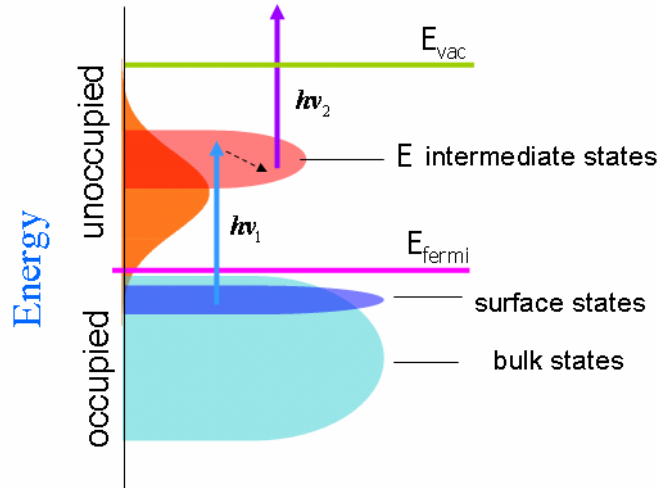


Figure 3.1 Excitation scheme in two-photon process.

As shown in Fig. 3.1, recording the “photoelectron current” vs. “scanning the electron energy” gives the 2PP energy spectrum, which contains information on the joint DOS of both the occupied and unoccupied states. Especially, the red energy bands in Fig. 3.1 represent the unoccupied intermediate states.

Moreover, by performing the pump-probe experiments with femtosecond pulses having a variable time delay, we can measure the electron population dynamics in the unoccupied states. The time-dependent intermediate state population can be described by Eq. 3.2 quantitatively [57], involving various electron population and decay mechanisms in the k-space:

$$\frac{d(n(k,t))}{dt} = H(k,t) + \frac{d(n(k,t))}{dt} \Big|_{e-e} + \frac{d(n(k,t))}{dt} \Big|_{e-ph} + \{\text{sec.} - \text{process}\}. \quad (3.2)$$

The first term on the right side of Eq. 3.2 describes the hot-electron distribution induced by the laser excitation that we just addressed; the second term describes the electron population decay through electron-electron (e-e) scattering process, where an electron in the measured unoccupied state scatters with an electron in an occupied state [58, 59]; the third term describes the electron-phonon scattering, which is generally much slower and removes much less energy so it is less important than e-e scattering [60]; the last term represents the overall secondary processes, such as the Auger electron process, or the ultrafast interfacial charge transfer, which can also affect the population dynamics [61-63]. In the following sections, these relevant processes will be discussed separately.

3.1.2 Fermi-Liquid Theory Description of Electron-electron Scattering

The electron-electron (e-e) scattering process through the screened Coulomb interaction [58, 59] can be extremely fast, causing the excited state population decay on femtosecond time scales. Fig. 3.2 describes the constraints on e-e scattering imposed by energy and momentum conservation within the Fermi liquid theory [58]. Typically, an electron excited to an energy E above the Fermi level with a momentum \vec{k} scatters with an electron at Energy E_1 with a momentum \vec{k}_1 state inside the Fermi sea. The scattering process generates two secondary electrons above the Fermi level with momenta \vec{k}_2, \vec{k}_3 . The overall e-e scattering rate can be described by

$$\frac{df(k)}{dt} \Big|_{e-e} = (1 - f(k))S_e^+(\vec{k}) + f(k)S_e^-(\vec{k}), \quad (3.3)$$

where $f(k)$ and $1 - f(k)$ are electron and hole occupation factors; $S_e^+(\vec{k})$ and $S_e^-(\vec{k})$ represent the electron scattering rates into and out of the \vec{k} state, respectively. The in and out scattering rates are given by

$$S_e^+(\vec{k}) = \frac{2\pi}{\hbar} \sum_{k_1, k_2, k_3} |M(k, k_1, k_2, k_3)|^2 (1 - f(k_1))f(k_2)f(k_3)\delta_k \delta_E, \quad (3.4)$$

and

$$S_e^-(\vec{k}) = \frac{2\pi}{\hbar} \sum_{k_1, k_2, k_3} |M(k, k_1, k_2, k_3)|^2 (-f(k_1))(1 - f(k_2))(1 - f(k_3))\delta_k \delta_E, \quad (3.5)$$

where the delta functions δ_k and δ_E in the above equations indicate the momentum and energy conservation in an e-e scattering process.

To obtain the e-e scattering rate, requires the calculation of the matrix terms $|M(k, k_1 | k_2, k_3)|$ in Eqs. (3.4) and (3.5) given by the screened Coulomb potential [64]

$$|M|^2 = \frac{e^4}{q^4 \epsilon_0^4 |\epsilon(\vec{q}, E_{ex})|^2}, \quad (3.6)$$

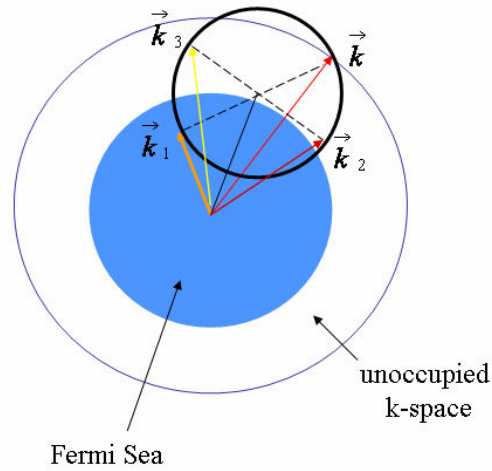


Figure 3.2 The electron-electron scattering process according to the Fermi-Liquid theory. The inner solid circle represents Fermi sea, while the outer bigger circle represents the momentum \vec{k} space.

where ε_0 is the vacuum dielectric constant, $\vec{q} = \vec{k} - \vec{k}_2$ and $E_{ex} = E(\vec{k}) - E(\vec{k}_2)$ are the momentum and energy exchanged through the e-e scattering. The cross section represents the probability of the hot electron originally having $E(\vec{k})$ in the energy/momentum space scattering with an electron having $E(\vec{k}_1)$ within the Fermi sea, to create two new electrons above the Fermi level having energies $E(\vec{k}_2)$ and $E(\vec{k}_3)$ after the scattering [57]. The long wavelength static approximation gives $\varepsilon(\vec{q} = 0, E_{ex} = 0) = \varepsilon_b$, which can be estimated from the tabulated dielectric constant of the metal [65].

By using the Thomas-Fermi approximation, the dielectric coefficient can be expressed as,

$$\varepsilon(\vec{q}, E_{ex} = 0) = \varepsilon_b \left(1 + \frac{q_s^2}{q^2}\right), \quad (3.7)$$

where $q_s = \beta \cdot q_{TF}$, Thomas-Fermi screening wave vector $q_{TF} = \frac{e^2}{\varepsilon_0 \varepsilon_b} \sum_k \frac{\partial f(k)}{\partial E_k}$ and β is the adjustable scale parameter used to fit the experimental result.

The free-electron scattering matrix element given by Thomas-Fermi screening is

$$|M|^2 = \frac{e^4}{q^4 \varepsilon_0^2 |\varepsilon[\vec{q}, E_{ex}]|^2} = \frac{e^4}{q^4 \varepsilon_0^2 \varepsilon_b^2 \left(1 + \frac{\beta^2 e^2}{\varepsilon_0 \varepsilon_b q^2} \sum_k \frac{\partial f}{\partial E_k}\right)^2}. \quad (3.8)$$

Applying derivations in Eqs. (3.3-3.5) and (3.8), as well as integration in the k-space near the Fermi surface region (typically $|k_i| = k_F$, $i = 0 \rightarrow 3$), thus the overall e-e scattering rate at $T = 0$ K is given by [2]:

$$\frac{1}{\tau_{ee}} = \frac{e^4 k_F^2}{16\pi^3 \hbar^4 \varepsilon_0^2 v_F^3 q_s^3} \times \left[\frac{2k_F q_s}{4k_F^2 + q_s^2} + \tan^{-1}\left(\frac{2k_F}{q_s}\right) \right] (E - E_F)^2. \quad (3.9)$$

Eq. 3.9 can be employed to predict the energy dependence of the electron decay rates through screened Coulomb interaction in different metals. The hot-electron lifetimes are predicted to follow an inverse-square rule of electron energy: as the electron energy approaches the Fermi energy, the electron scattering time becomes infinite; at a higher energies, electron scattering times decrease as:

$$\tau_{ee} \propto \frac{1}{(E - E_F)^2}. \quad (3.10)$$

The free electron Fermi-liquid theory (FLT) gives only an upper limit for e-e scattering rates in real metals, since the hot electron near the Fermi level is significantly screened by virtual valance band excitations and the ionic nuclear cores, so the screening length calculation in (3.7) can be modified as following when the band structure (especially the metal d-band) and the density of state (DOS) at the Fermi level are taken into account:

$$q_s = q_{TF} = \left(\frac{e^2}{\epsilon_0} D(E_F) \right)^{\frac{1}{2}} \quad (3.11)$$

Ogawa et al. applied both the free-electron FLT model and the band structure calculation to calculate the hot electron lifetimes and compared with the experimental data [50]. Where in the free-electron model, the screening length q_{TF}^{-1} they used is 0.55 Å, while in band structure calculation, the scaled screening length is decreased to 0.27 Å through Eq. (3.11). It turns out the band structure calculation reproduced the hot-electron lifetimes for the low index surface of Cu

better than the free electron model (Fig. 3.3). FLT calculation either implementing free electron approximation or involving the electronic band structure for the specific metals with different crystal faces usually gives reasonable predictions for the hot-electron lifetimes in the low energy range (0.3~2.2 eV) [52, 66]. And more advanced theories employing the recent developed techniques to calculate the e-e inelastic scattering mechanism and hot electron lifetimes are extensively discussed by Echenique et al. and in the references therein [67]. The study of the electron dynamics through e-e scattering process employing the FLT approximation shows the ultrafast electron process within several to several tens of femtoseconds and opens a window to the investigation of the electron dynamics in a semiconductor.

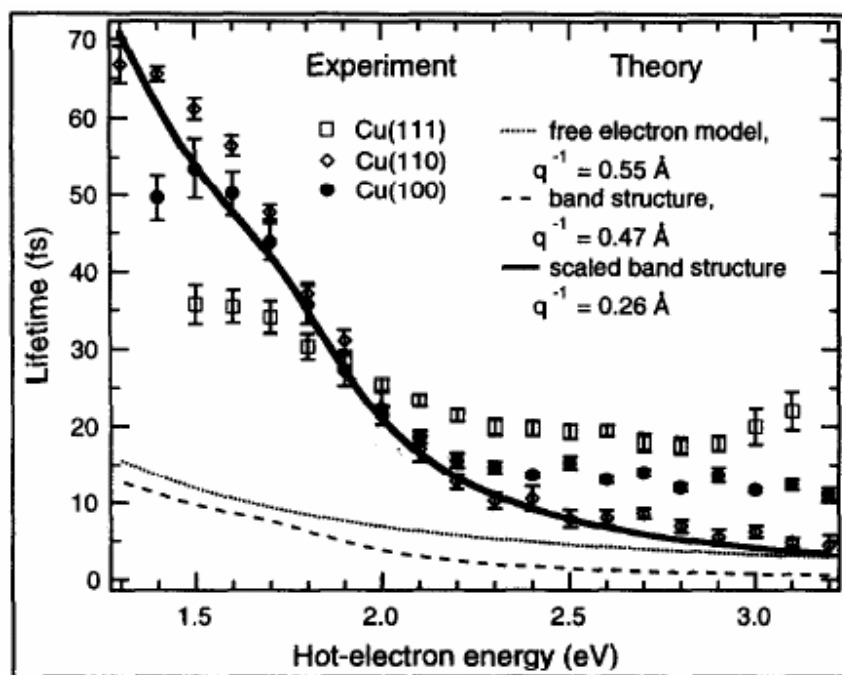


Figure 3.3 The experimentally measured hot-electron lifetimes for the low index surfaces of Cu are compared with theoretical calculations, by free electron model or the band structure calculation [2].

3.1.3 Other Electron Dynamical Pathways

The e-e scattering rate is not the only factor that determines the electron decay time scale at the intermediate energies above the Fermi level. Sometimes other processes can have influence on the intermediate state lifetime as detected by the 2PP method resulting in deviations from predictions of the Fermi liquid theory.

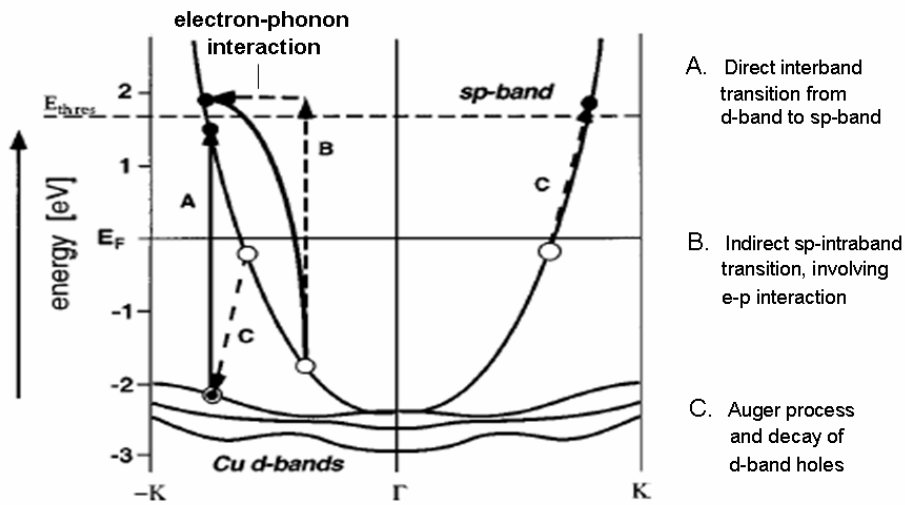


Figure 3.4 Various electron excitation mechanism in copper [62].

Fig. 3.4 describes the different electron excitation pathways within a typical metal such as Cu. The direct interband transition from the occupied d-band located 2 eV below the Fermi level to an unoccupied upper sp-band is denoted as process A. With a photon energy of $h\nu = 3.6$ eV, the interband excitation can generate electrons with a threshold value E_{thres} of 1.6 eV. This leads to a dramatic drop in the 2PP intensity above the 1.6 eV intermediate energy level. Nevertheless, electrons can still be excited above E_{thres} by an indirect sp-intraband transition, denoted as process B in Fig. 3.4. But in this case, the electron must scatter with a defect in the crystal lattice or through a phonon to satisfy the constraint of momentum conservation. Because of the difference in the DOS and the order of the excitation process, the process A is much more likely to generate hot electrons than process B. Because the process A is more probable, it can generate a large amount of d-band holes. The Auger decay of these photogenerated d-band holes results in

the creation of hot (secondary) electrons. The Auger decay mechanism for generation of hot electrons is denoted as process C in Fig. 3.4.

So the generation rate of the hot electrons excited via interband or intraband transitions (process A/B) follows the time duration of pump pulse. Meanwhile, the generation of the d-band holes in process C also follows the pump pulse, but the secondary electron population excited through Auger decay builds up with a time delay that is related to the average lifetime of the holes. So when the electron dynamics is also involves the Auger decay of d-band holes, the delayed excitation has to be included in the hot electron lifetime analysis [50, 62].

Another important electron dynamic pathway, which we should keep in mind, is the electron transport from the surface into the bulk. Evidence for electron transport effect was reported previously from the sample thickness dependence of time-resolved photoemission measurements [68]. In a photoemission experiment, the sample is illuminated by the excitation light and the light penetration depth is mainly determined by absorption coefficient for certain wavelength and usually in the order of 100 nm. However, not all the accelerated (excited) electrons in the illuminated region are able to escape to surface as photoemitted electrons. Only those which do not lose energy significantly by inelastic scattering on their passage to the surface will eventually escape and finally appear in the photoemission spectrum. The escape depth of electrons for a broad range of materials is described by the electron kinetic energy by the empirically determined “Universal Curve” [69] (Appendix C). In a typical photoemission experiment, the final state energy of a photoexcited electron energy relative to E_F is around 4 ~ 10 eV, corresponding to an escaped depth $<100 \text{ \AA}$.

So the relevant length scale for the transport of electrons from the observation region is below 100 \AA . As shown in Fig. 3.5, the nonequilibrium electron can move out of the illuminated region in all directions till they are cooled down via the interaction with the crystal lattice, and an electron with $\sim 1 \text{ eV}$ energy is approximately corresponding to a Fermi velocity of $\sim 10^4 \text{ m/s}$. In a relatively thicker sample (e.g. 100 \AA , the left diagram of Fig. 3.5), the electrons which originally have the ability to escape as photoelectrons, could however partially transport down to the bulk, which represents an additional loss mechanism of hot electrons. On the other hand, in the much thinner sample (e.g. $< 20 \text{ \AA}$, the diagram on the right side), the excess electrons are well confined to be photoemitted [68]. This causes the measured electron lifetimes by using various thicknesses ($< 100 \text{ \AA}$) of samples are different.

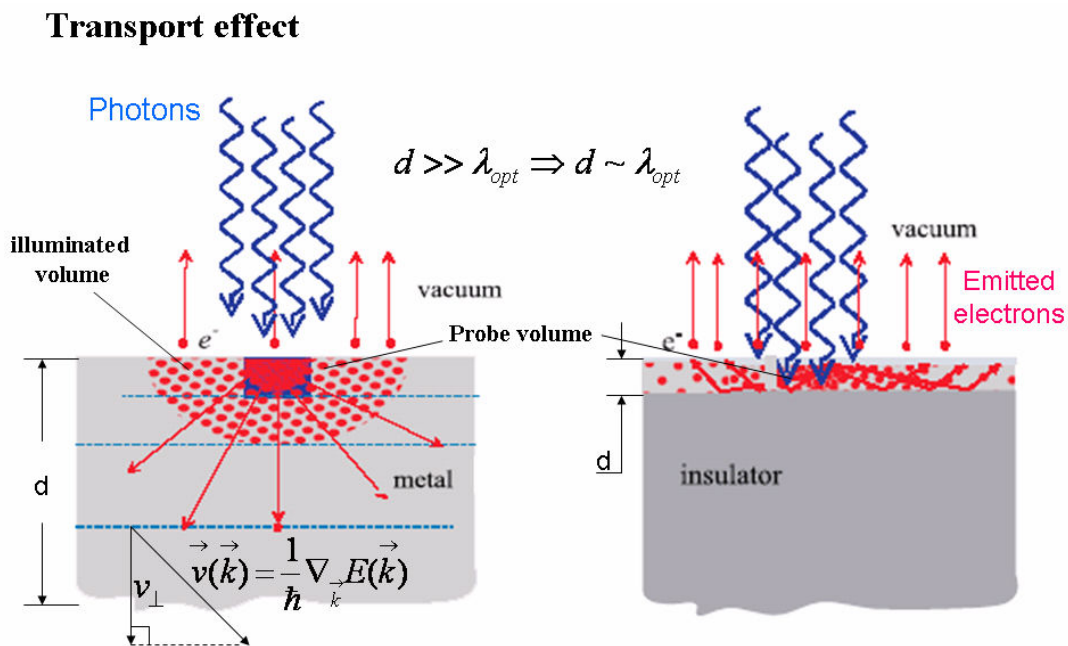


Figure 3.5 Excited electron transport into the bulk [68].

At the circumstance when the electron transport effects are non-negligible, the measured overall electron decay rate is faster than the true population decay kinetics, and can be described as

$$\frac{1}{\tau_{Measured}} = \frac{1}{\tau_{Dynamics}} + \frac{1}{\tau_{Transport}}, \quad (3.12)$$

where $\tau_{Measured}$, $\tau_{Dynamics}$ and $\tau_{Transport}$ are the measured electron decay time scale, the intrinsic electron decay time scale and the addition transport related time scale respectively. Theories and experiments have been addressed the effect of electron transport on the hot electron lifetimes, but a satisfactory understanding is not available yet.

3.2 Diagnostic Measurement of the Laser Excitation Source

3.2.1 Nonlinear Autocorrelation Characterization of the Laser Pulse

Before performing a time-resolved measurement, we need to optimize and characterize the photoexcitation pulse. The pulse is optimized by minimizing of the overall dispersion in the optical path length. The pulse is characterized by a nonlinear autocorrelation diagnostic technique [28]. In a nonlinear autocorrelation signal, a pair of pulse replicas is overlapped in a nonlinear crystal to generate the second harmonic signal. Scanning the delay between the two pulses and recording the second harmonic signal provides the autocorrelation trace, which contains the information on the time duration and the phase of the pulse.

Overlapping of two orthogonally polarized or noncollinear pulses results in an intensity autocorrelation signal [28]:

$$A_c(\tau) = \int_{-\infty}^{+\infty} I_{pump}(t-\tau)I_{probe}(t)dt. \quad (3.13)$$

The intensity autocorrelation provides only very little information on the pulse shape, since different symmetric and asymmetric pulse shapes can give very similar autocorrelation profiles. Moreover, there is no information on the phase of the excitation field. The intensity autocorrelation is widely used as the diagnostic technique because it is simple to implement, however to get more detailed information on the pulse shape more complex methods have to be employed.

If two pulses with same polarizations propagate collinearly, such as the two identical pulses $E_1(t-\tau)$ and $E_2(t)$ generated by the MZI [37] an interference pattern is observed when scanning τ and detecting the light intensity. This gives the electric field autocorrelation,

$$\begin{aligned} I(\tau) &= \int_{-\infty}^{+\infty} [E_1(t-\tau) + E_2(t)]^2 dt \\ &= |E_1|^2 + |E_2|^2 + \tilde{A}_{12}^+(\tau) + \tilde{A}_{12}^-(\tau), \quad (3.14) \end{aligned}$$

where the intensity consists of constant amplitudes $|E_1(t-\tau)|^2 + |E_2(t)|^2$, and interference terms

$\tilde{A}_{12}^+(\tau) \sim E_1^*(t-\tau)E_2(t) \cdot e^{i\omega_l t}$ and its complex conjugate $\tilde{A}_{12}^-(\tau)$, which oscillate about an

average frequency ω_l . The Fourier transformation of $\tilde{A}_{12}^+(\tau)$ is,

$$\begin{aligned}\tilde{A}_{12}^+(\omega) &= \int_{-\infty}^{+\infty} \tilde{A}_{12}^+(\tau) \cdot e^{-i\omega\tau} d\tau = \int_{-\infty}^{+\infty} d\tau \cdot e^{-i(\omega-\omega_l)\tau} \left[\int_{-\infty}^{+\infty} dt \cdot \tilde{\varepsilon}_1(t-\tau) \tilde{\varepsilon}_2(t) \right] \\ &= \tilde{\varepsilon}_1(\omega - \omega_l) \cdot \tilde{\varepsilon}_2^*(\omega - \omega_l) \\ &\propto \tilde{E}_1(\omega) \tilde{E}_2^*(\omega)\end{aligned}\quad (3.15)$$

For two identical inputs we have $\tilde{A}_{12}^+(\omega) \propto I(\omega)$, which is actually the laser intensity spectrum.

Thus, the electric field autocorrelation provide information on the pulse spectrum, which can also be obtained by more conventional means. In order to learn more details about the laser pulse shape and phase, the nonlinear autocorrelation technique has to be involved.

The non-linear interferometric autocorrelation can be measured by surface second harmonic generation (SSHG) from a metal surface. In Fig 3.6, we describe the SSHG autocorrelation measurement from a Cu surface [2, 70, 71]. Since Cu is a homogenous media, only at the surface, the symmetry is broken to satisfy one of the most essential requirements for the non-linear optics generation. Two fundamental pulses with p-polarization induce second harmonic generation the metal near the surface region, and the harmonic signal with s-polarization is selected by a high-pass filter. Since in a SSHG process, the frequency doubling occurs usually within surface depth of < 100 nm, so the phase-matching condition is always satisfied.

Therefore, the main concern in a surface harmonics generation process is trying to find an appropriate axis for the incident light under certain crystalline geometry to maximize the nonlinear electric susceptibility for the substrate materials being used for SSHG, e.g. Cu or BBO crystal.

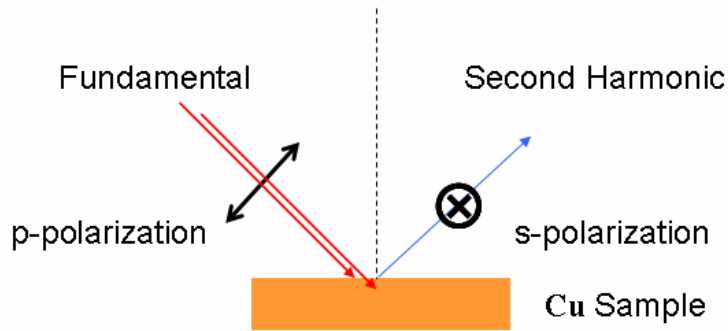


Figure 3.6 SSHG at a metal surface.

The non-linear interferometric autocorrelation signal [28] is given by

$$G_2(\tau) = \int_{-\infty}^{+\infty} \{ [E_1(t-\tau) + E_2(t)]^2 \}^2 dt. \quad (3.16)$$

Inserting electric field $E(t) = E^+(t) + E^-(t) = \frac{1}{2} \tilde{E} \cdot e^{i\omega t} + \frac{1}{2} \tilde{E}^* \cdot e^{-i\omega t}$ in Eq. (3.16) and performing several steps of derivation leads to

$$G_2(\tau) = A(\tau) + 4 \operatorname{Re}\{B(\tau) \cdot e^{i\omega\tau}\} + 2 \operatorname{Re}\{C(\tau) \cdot e^{2i\omega\tau}\}, \quad (3.17)$$

where $\tilde{E} = |E(t)| e^{i\varphi(t)} = \varepsilon(t) \cdot e^{i\varphi(t)}$, ω_l is the central frequency of the laser pulse, and the A, B and C terms are the fundamental, the first order and the second order envelopes respectively, given by the following three equations:

$$\begin{aligned}
A(\tau) &= \int_{-\infty}^{\infty} dt \{ \varepsilon_1^4(t-\tau) + \varepsilon_2^4(t) + 4\varepsilon_1^2(t-\tau)\varepsilon_2^2(t) \} \\
\tilde{B}(\tau) &= \int_{-\infty}^{\infty} dt \{ \varepsilon_1(t-\tau)\varepsilon_2(t) [\varepsilon_1^2(t-\tau) + \varepsilon_2^2(t)] \cdot e^{i[\varphi_1(t-\tau) - \varphi_2(t)]} \} \quad (3.18) \\
\tilde{C}(\tau) &= \int_{-\infty}^{\infty} dt \{ \varepsilon_1^2(t-\tau)\varepsilon_2^2(t) \cdot e^{2i[\varphi_1(t-\tau) - \varphi_2(t)]} \}
\end{aligned}$$

Both the first and the second order envelopes include the phase terms and can be used as diagnostic signals of the dispersions of the input laser pulses. The more detailed and concrete discussions regarding to the interferometric autocorrelation will be given later.

From the equations (3.17) and (3.18) it is evident that at the zero delay $G_2(0) = 16 \int \varepsilon^4(t)$; while at infinite delay $G_2(\infty) = 2 \int \varepsilon^4(t)$. So the peak to background ratio in the second order interferometric autocorrelation is 8:1.

3.2.2 Dispersion and Linear Chirp for a Gaussian Pulse

Dispersion is defined as the relationship between the wave number and the frequency,

$k(\omega) = \frac{\omega}{c}n(\omega)$ of an electromagnetic field propagating through a dispersive medium, where

$n(\omega)$ is the frequency dependent index of refraction. Using Taylor expansion at the central

frequency up to the second-order, we have

$$k(\omega) = k(\omega_l) + \left. \frac{dk}{d\omega} \right|_{\omega_l} (\omega - \omega_l) + \frac{1}{2} \left. \frac{d^2k}{d\omega^2} \right|_{\omega_l} (\omega - \omega_l)^2 + \{higher - order\}. \quad (3.19)$$

The first-order term is the trivial time delay, but it has to be retained for the discussion of the effect of the 3rd-order term. Only considering the first-order dispersion, the laser electrical field in the frequency domain is

$$E^{(1)}(\omega) = A \cdot e^{i[\omega \frac{L}{c} - k(\omega)L]} = A \cdot \exp\{-i[(k_l - n \cdot \frac{\omega}{c})L + k_l'(\omega - \omega_l)L]\} \quad (3.20)$$

After the Fourier transformation,

$$E^{(1)}(t) = A \cdot \exp[i\omega_l(t - (\frac{k_l}{\omega_l} - \frac{n(\omega)}{c})L)] \cdot \delta[t - (k_l' - \frac{n(\omega)}{c})L]$$

Therefore, the first-order dispersion term is actually a time delay without involving any phase information:

$$\Delta\tau = (\omega \cdot \frac{dn(\omega)}{d\omega} |_{\omega_l}) \cdot \frac{L}{c}. \quad (3.21)$$

Then let us look at the second-order dispersion for a Gaussian pulse $A(t) \propto e^{-\frac{1}{2}(\frac{t}{T_0})^2}$. The corresponding amplitude in the frequency domain is

$$A(\omega) = \int A(t) \cdot e^{-i(\omega-\omega_l)t} = \exp[-\frac{1}{2}(\omega-\omega_l)^2 \cdot T_0^2].$$

$$\begin{aligned} \text{So } E^{(2)}(\omega) &= A(\omega) \cdot \exp[-i \frac{1}{2} \frac{d^2k}{d\omega^2} |_{\omega_l} (\omega-\omega_l)^2 L] \\ &= \exp[-\frac{1}{2}(\omega-\omega_l)^2 T_0^2 (1 + i \frac{k_l''}{T_0^2} L)] \approx \exp[-\frac{1}{2}(\omega-\omega_l)^2 T_0^2 (1 + i \frac{k_l''}{2T_0^2} L)^2] \quad (3.22) \end{aligned}$$

Assuming the second-order dispersion term or group velocity dispersion (GVD) is a small, the Fourier transformation of (3.22) gives

$$E^{(2)}(t) = F^{-1}[E(\omega)] = \exp[-\frac{1}{2}(\frac{t}{T_0})^2 (1 - i \frac{k_l''}{T_0^2} L)] = e^{-\frac{1}{2}(\frac{t}{T_0})^2 (1+a-i)} \quad (3.23)$$

So apparently, the GVD corresponds to the linear chirp defined for a Gaussian pulse as:

$$a = -\frac{L}{T_0^2} \frac{d^2k}{d\omega^2} |_{\omega_l} = -\frac{L}{cT_0^2} [\omega_l \frac{d^2n(\omega)}{d\omega^2} |_{\omega_l} + 2 \frac{dn(\omega)}{d\omega} |_{\omega_l}] \quad (3.24)$$

Combining the 1st order dispersion and GVD, we have

$$E^{(1,2)}(t) \approx e^{-\frac{1}{2}\left(\frac{t-\Delta\tau}{T_0}\right)^2(1+a \cdot i)} \quad (3.25)$$

Let us also briefly discuss the higher orders of dispersion. The 3rd order dispersion in Eq. (3.19) is

$$E^{(3)}(\omega) = \exp\left[-i \frac{1}{6} \frac{d^3 k}{d\omega^3} \Big|_{\omega_l} (\omega - \omega_l)^3 L\right]. \quad (3.26)$$

$$\begin{aligned} \text{Then } E^{(3)}(t) &= \int_{-\infty}^{+\infty} E^{(3)}(\omega) \cdot e^{-i(\omega - \omega_l)t} d\omega = \int_{-\infty}^{+\infty} e^{-\frac{i}{6} \frac{d^3 k}{d\omega^3} \Big|_{\omega_l} (\omega - \omega_l)^3 L} \times e^{-i(\omega - \omega_l)t} d\omega \\ &= \int_{-\infty}^{+\infty} e^{-i(b \cdot x^3 + c \cdot x)} = \int_{-\infty}^{+\infty} \cos[f(x)] dx, \quad (3.27) \end{aligned}$$

where $f(x) = b \cdot x^3 + c \cdot x$ with $b = \frac{L}{6} \frac{d^3 k}{d\omega^3} \Big|_{\omega_l}$ and $c = t$.

It seems impossible to obtain an explicit result from the integration in Eq. (3.27), however if the third-order dispersion is considered, the overall analytic electrical field is

$$E(t) = E^{(1,2)}(t) \otimes E^{(3)}(t) = \exp\left[-\frac{1}{2}\left(\frac{t-\Delta\tau}{T_0}\right)^2(1+a \cdot i)\right] \cos(\omega_l t) \otimes E^{(3)}(t) \quad (3.28)$$

To summarize, the 1st-order dispersion gives the time delay; the GVD is proportional to the linear chirp for a Gaussian pulse; and the 3rd-order dispersion is essentially equal to a convolution with the lower order term, usually giving sub-pulse in the wings of the main pulse. And the sub-pulse gives symmetrically displaced secondary pulse structure in the corresponding autocorrelation signal.

Applying a Gaussian pulse with a linear chirp term $\varepsilon(t) = e^{-\frac{1}{2}(\frac{t}{T_0})^2(1+a \cdot i)}$ into the Eqs. (3.17) and (3.18), the calculated SHG signal is given by

$$G_2(\tau) = \{1 + 2 \exp[-(\frac{\tau}{T_0})^2] + 4 \exp[-\frac{a^2 + 3}{4}(\frac{\tau}{T_0})^2] \cos[\frac{a}{2}(\frac{\tau}{T_0})^2] \cos(\omega_l \tau) + \exp[-(1 + a^2)(\frac{\tau}{T_0})^2] \cos(2\omega_l \tau)\} \quad (3.29)$$

Apparently, it consists of three primary components: the fundamental 0ω , the first order envelope 1ω and the second order envelope 2ω . Using the center wavelength of 400 nm corresponding to an optical cycle $T_l = \frac{2\pi}{\omega_l} = 1.33$ fs, the pulse width $T_0 = 10$ fs and a dimensionless linear chirp term “a” with various values, we can get a series of stimulated autocorrelation signals in Fig. 3.7.

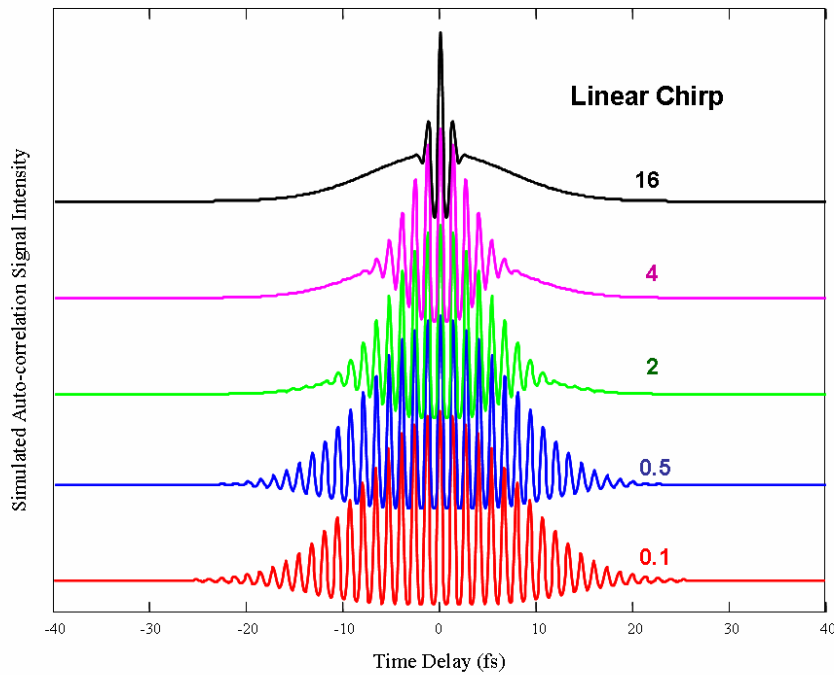


Figure 3.7 Calculated second order interferometric autocorrelation signals for Gaussian pulses with different linear chirp parameters indicated in the figure.

Experimentally, the non-linear interferometric autocorrelation signals can be obtained either through a pure optical method: e.g. the surface second harmonic generation process as we discussed previously, or through a time-resolved two-photon photoemission. Here, we employed the latter to assess and optimize the experimental pulses. Typically, we perform the nonlinear autocorrelation experiment on a polycrystalline molybdenum surface in the UHV chamber. Before the laser pulse is delivered into the UHV chamber, it has been through a dispersion compensation set-up, in which the positive group velocity dispersion in the optical elements (lens

and beamsplitter) and air is compensated by inserting optical elements with negative dispersion. In our laboratory, we use two sets of two mirror-pairs, where each of the mirror-pairs is coated with multi-layer negatively dispersive materials. And each mirror is coated to provide in combination well-balanced (constant) negative GVD across through the entire laser emission spectrum. So the amount of dispersion compensation is purely determined by the number of laser reflection times between the mirror pairs. Fig. 3.8 shows a representative experimental interferometric autocorrelation signal, which appears as good as the simulated autocorrelation signal for Gaussian pulse with minor third-order dispersion. Therefore the nonlinear interferometric signal serves as an excellent diagnostic method for adjustment and balance of the dispersion of the laser pulse.

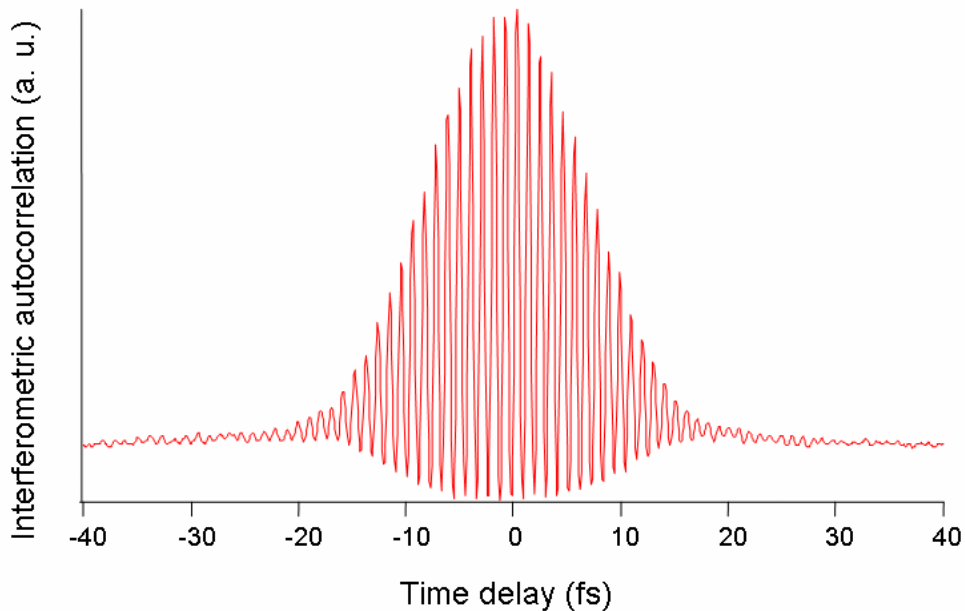


Figure 3.8 Experimental autocorrelation signals for excitation laser pulse.

3.3 Optical Bloch Equation Approach to Simulating Electron Dynamics

This section presents the Optical Bloch Equation (OBE) [2, 27, 28, 72] approach to simulation the electron dynamics in a two-photon photoemission experiment.

Fig. 3.9 shows the excitation scheme for two-photon absorption in metal and semiconductors. The excitation, in its simplest form, can be described by a scheme involving three energy levels: the energy level 0 is below the Fermi level, corresponding to an occupied state; the energy level 1 is above the Fermi level, but below the vacuum level, corresponding to an unoccupied state; and the energy level 2 is a free electron state above the vacuum level. With photon energy satisfying the resonance energy between the initial and intermediate states, and the intermediate and final states, femtosecond pulses can induce the two-photon absorption process between 0 and 2 states, probing the one and two-photon coherences between different energy levels and the population in the intermediate state. In particular, the OBE scheme is applied to TiO_2 as described on the right side of Fig. 3.9. For the n-doped semiconductor the Fermi level is located in the bandgap, just below the CBM. The band gap states below the Fermi level constitute the DOS of the initial energy levels 0 [9, 73].

Now, Let us consider an electronic system of discrete energy states within a set of normalized orthogonal basis ϕ_k , having a non-perturbated Hamiltonian

$$H_0 \phi_k = E_k \phi_k = \hbar \omega_k \phi_k. \quad (3.30)$$

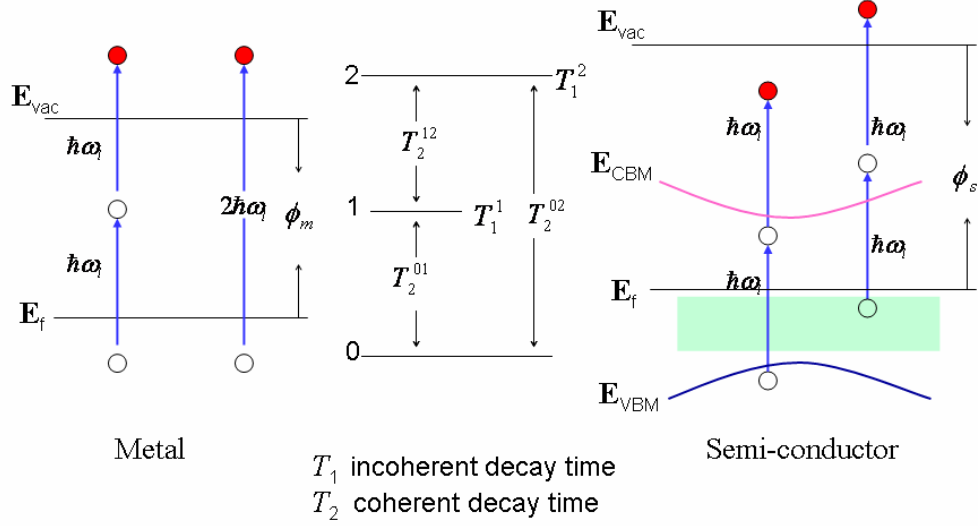


Figure 3.9 OBE in a metal or semi-conductor system.

The excitation laser pulse introduces a time-dependent perturbation term that couples the eigenstates of the system. Then the total Hamiltonian is $H(t) = H_0 + H'(t)$, and the new wave function can be expressed using the original basis set, $\psi(t) = \sum_k a_k(t) \phi_k = \sum_k e^{-i k \cdot \omega_l t} c_k(t) \phi_k$ in a rotating coordinate with an angular frequency ω_l (the central frequency of the laser pulse) [27].

Solving the time-dependent Schrödinger equation: $i\hbar \frac{\partial \psi(t)}{\partial t} = H(t) \psi(t)$, we get

$$\sum_k \phi_k [c_k(t)(-i k \omega_l) e^{-i k \omega_l t} + \dot{c}_k(t) e^{-i k \omega_l t}] = \frac{-i}{\hbar} \sum_k c_k(t) (H_0 + H'(t)) \phi_k e^{-i k \omega_l t} \quad (3.31)$$

Eq. (3.31) is multiplied by the complex conjugate ϕ_k^* and integrated in the wave packet space, resulting in

$$\dot{c}_n = -i(\omega_n - n\omega_l)c_n - \frac{i}{\hbar} \sum_k H'_{nk} e^{i(n-k)\omega_l t} c_k, \quad (3.32)$$

where the matrix element $H'_{nk} = \int \phi_n^* H'(t) \phi_k d^3 r$ and the perturbation term can be approximated in the electric dipole approximation:

$$H'(t) = -e \cdot r \cdot E(t) = -e \cdot r \cdot A(t) \cos(\omega_l t).$$

In ladder representation $r \propto (\hat{a} + \hat{a}^+)$ only the two adjacent matrix elements in the Eq. (3.32) do not vanish. If we just consider a three-energy-level system, 0-1-2, coupled by a two-photon transition (where δ indicates the time-delay between the pump and probe pulses), the various occupation coefficients are:

$$\begin{aligned} \frac{\partial c_0(t)}{\partial t} &= -i\omega_0 c_0 - \frac{i}{\hbar} [E_1(t) \cos(\omega_l t) + E_1(t - \delta) \cos[\omega_l(t - \delta)]] \cdot e^{-i\omega_l t} c_1 \\ \frac{\partial c_1(t)}{\partial t} &= -i(\omega_1 - \omega_l) c_1 - \frac{i}{\hbar} [E_2(t) \cos(\omega_l t) + E_2(t - \delta) \cos[\omega_l(t - \delta)]] \cdot e^{-i\omega_l t} c_2 \\ &\quad - \frac{i}{\hbar} [E_1(t) \cos(\omega_l t) + E_1(t - \delta) \cos[\omega_l(t - \delta)]] \cdot e^{i\omega_l t} c_0 \\ \frac{\partial c_2(t)}{\partial t} &= -i(\omega_2 - 2\omega_l) c_2 - \frac{i}{\hbar} [E_2(t) \cos(\omega_l t) + E_2(t - \delta) \cos[\omega_l(t - \delta)]] \cdot e^{i\omega_l t} c_1 \end{aligned} \quad (3.33)$$

Where the amplitudes E_1 or E_2 in the above equations are relevant to the transition coefficients either between 0 and 1, or between 1 and 2 respectively. When the energy level 1 corresponds to a real excited state rather than a virtual state, the transition coefficient E_1 becomes a much larger quantity than that for a virtual state.

Usually, we would rather consider the density operator elements $\rho_{mn} = c_m c_n^*$, which have more physical meanings, where the diagonal elements ρ_{mm} correspond to the population at the energy level m , and the off-diagonal elements ρ_{mn} represent the coherence between energy states m and n .

Taking the first-order derivative of $c_m(t)c_n(t)^*$, we get

$$\frac{\partial(c_m(t)c_n(t)^*)}{\partial t} = \frac{\partial c_m(t)}{\partial t} c_n(t)^* + c_m(t) \frac{\partial c_n(t)^*}{\partial t} \quad (3.34)$$

Because the energy levels 1 and 2 are unoccupied states, their transient populations will decay back to zero. Moreover, the optical excitation creates coherences through the dipole coupling that oscillate at the single photon pulse $\hbar\omega_l$ or a two-photon $2\hbar\omega_l$ frequencies. To describe the time dependence of the density matrix elements we define the time scales T_1^1 and T_1^2 as the

population decay times at energy level 1 and level 2; T_2^{01} , T_2^{12} as the first-order decoherence times (in between states 0 and 1 or states 1 and 2), and T_2^{02} as the second-order decoherence time (in between states 0 and 2) [2]. Using derivative formula (3.34) and these time scales, we can construct 9 first-order differential equations for the three level system. However, some of them are complex conjugates, resulting in only 6 independent equations.

$$\begin{aligned} \frac{\partial \rho_{11}}{\partial t} = & -\frac{1}{T_1} \rho_{11} + \frac{i}{\hbar} f_1(t, \delta) [e^{-i\omega_1 t} c_1 c_0^* - e^{i\omega_1 t} (c_1 c_0^*)^*] \\ & - \frac{i}{\hbar} f_2(t, \delta) [e^{-i\omega_2 t} c_2 c_1^* - e^{i\omega_2 t} (c_2 c_1^*)^*] \end{aligned} \quad (3.35.1)$$

$$\frac{\partial \rho_{22}}{\partial t} = -\frac{1}{T_1^2} \rho_{22} + \frac{i}{\hbar} f_2(t, \delta) [e^{-i\omega_2 t} c_2 c_1^* - e^{i\omega_2 t} (c_2 c_1^*)^*] \quad (3.35.2)$$

$$\frac{\partial \rho_{00}(t)}{\partial t} = -\frac{\partial \rho_{11}(t)}{\partial t} - \frac{\partial \rho_{22}(t)}{\partial t} \quad (3.35.3)$$

$$\begin{aligned} \frac{\partial (c_1 c_0^*)}{\partial t} = & -[i(\Delta_1 - \omega_0) + \frac{1}{T_2^{01}} + \frac{1}{2T_1}] c_1 c_0^* \\ & + \frac{i}{\hbar} f_1(t, \delta) e^{i\omega_1 t} (\rho_{11} - \rho_{00}) - \frac{i}{\hbar} f_2(t, \delta) e^{-i\omega_2 t} c_2 c_0^* \end{aligned} \quad (3.35.4)$$

$$\begin{aligned} \frac{\partial (c_2 c_1^*)}{\partial t} = & -[i(\Delta_2 - \Delta_1) + \frac{1}{T_2^{12}} + \frac{1}{2T_1} + \frac{1}{2T_1^2}] c_2 c_1^* \\ & + \frac{i}{\hbar} f_2(t, \delta) e^{i\omega_2 t} (\rho_{22} - \rho_{11}) + \frac{i}{\hbar} f_1(t, \delta) e^{-i\omega_1 t} c_2 c_0^* \end{aligned} \quad (3.35.5)$$

$$\begin{aligned} \frac{\partial(c_2 c_0^*)}{\partial t} = & -[i(\Delta_2 - \omega_0) + \frac{1}{T_2^{02}} + \frac{1}{2T_1^2}]c_2 c_0^* + \frac{i}{\hbar} e^{i\omega_1 t} [f_1(t, \delta)c_2 c_1^* \\ & - f_2(t, \delta)c_1 c_0^*] \end{aligned} \quad (3.35.6)$$

Where

$$f_1(t, \delta) = E_1(t) \cos(\omega_1 t) + E_1(t - \delta) \cos(t - \delta) = A_1 [e^{-\frac{t}{T_0}} \cos(\omega_1 t) + e^{-\frac{t-\delta}{T_0}} \cos[\omega_1(t - \delta)]]$$

and

$$f_2(t, \delta) = E_2(t) \cos(\omega_1 t) + E_2(t - \delta) \cos(t - \delta) = A_2 [e^{-\frac{t}{T_0}} \cos(\omega_1 t) + e^{-\frac{t-\delta}{T_0}} \cos[\omega_1(t - \delta)]]$$

are time-delayed pump-probe excitation transition functions. $\Delta_1 = \omega_1 - \omega_l$, $\Delta_2 = \omega_2 - 2\omega_l$ are the first- and second-order resonance detuning frequencies, respectively.

Applying a set of appropriate initial values for the density matrix elements, reasonable incoherent and coherent decay time scales, and suitable values for the excitation transition amplitudes and resonance detuning energies, we can perform the OBE simulation for the overall electronic system.

In our experiment, we use electron energy analyzer to measure the time-resolved 2PP data at the final state energies above the vacuum, so the experimental time-resolved 2PP spectrum measures

the value of density operator element $\rho_{22}(t, \delta)$ integrated over the pump probe sequence. Since the time scale of ~ 11 nanosecond corresponding to the interval between our ~ 90 MHz repetition laser pulses, is much longer than the relevant population and polarization time scales, we only need to integrate over a single pump- probe cycle T_A ,

$$2PP(\delta) = \int_0^{T_A} \rho_{22}(t, \delta) dt \approx \int_0^{\infty} \rho_{22}(t, \delta) dt. \quad (3.36)$$

However, the fitting the coherent and incoherent dynamic parameters of an electronic system by solving OBE is quite complicated, requires large amount of computational resources, and is usually restricted to single exponential decay kinetics (Eqs. 3.35). Instead of fitting to OBE equation, we use a special fitting procedure based on the Fourier transformation, which involves much simpler routine to calculate the various dynamical decay time scales.

3.4 Hot Electron Dynamics and the Fitting Procedures

Although the interferometric two-pulse correlation (I2PC) measurements of two-photon photoemission are very similar to the nonlinear interferometric autocorrelation signal (IAC), but in addition they contain information on the hot electron population and polarization dynamics, which broaden the signal. The photon pulse incident on the sample surface induces linear or non-linear polarization, which oscillates coherently at the excitation frequency or its higher harmonics, meanwhile the photoexcited electron decay incoherently through e-e elastic scattering. Coherent interaction with linear or non-linear polarization gives interference at both

1ω and 2ω frequencies; and incoherent excitation of hot electrons above the Fermi energy gives a phase independent component.

Therefore the I2PC signal can be decomposed into three different parts: the phase average 0ω , the 1ω envelope component, and 2ω envelope component. All three envelopes can be extracted from the experimental I2PC signal $I(\delta)$ (δ same as before is the time-delay between pump and probe pulses) by Fourier transformation over each optical cycle, which is demonstrated in Fig. 3.10, as [74]:

$$I_{2\omega}^{\text{exp}}(\delta) = \frac{4\lambda}{c} \sqrt{\left[\int_{\delta-\lambda/4c}^{\delta+\lambda/4c} I^{\text{exp}}(t) \cos(2\omega t) dt \right]^2 + \left[\int_{\delta-\lambda/4c}^{\delta+\lambda/4c} I^{\text{exp}}(t) \sin(2\omega t) dt \right]^2} \quad (3.37.1)$$

$$I_{1\omega}^{\text{exp}}(\delta) = \frac{2\lambda}{c} \sqrt{\left[\int_{\delta-\lambda/2c}^{\delta+\lambda/2c} I^{\text{exp}}(t) \cos(\omega t) dt \right]^2 + \left[\int_{\delta-\lambda/2c}^{\delta+\lambda/2c} I^{\text{exp}}(t) \sin(\omega t) dt \right]^2} \quad (3.37.2)$$

$$I_{pa}^{\text{exp}}(\delta) = \frac{\lambda}{c} \int_{\delta-\lambda/2c}^{\delta+\lambda/2c} I^{\text{exp}}(t) dt, \quad (3.37.3)$$

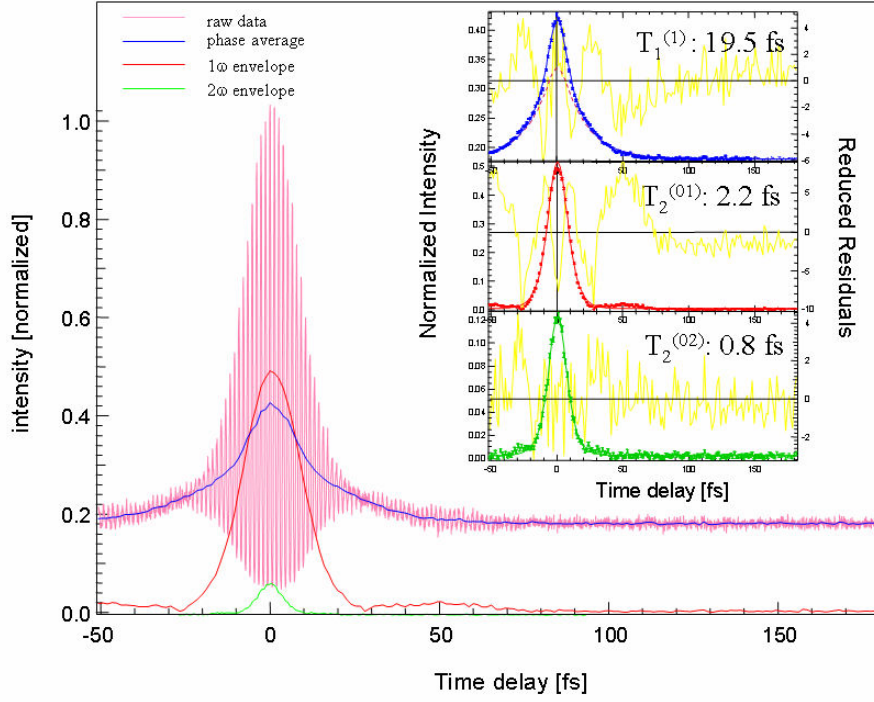


Figure 3.10 A typical I2PC signal for adsorbate covered TiO_2 surface is decomposed into three components: 0ω , 1ω , and 2ω . Fitting of the envelopes provides the polarization and population decay times.

which correspond to the green (2ω), red (1ω) and blue (0ω) curves in Fig. 3.10 respectively. The temporal width and shape of these components are determined both by the energy and phase relaxation time scales of the hot electrons in the sample and by the excitation laser pulse width. From the IAC signal for a Gaussian pulse in Eq. (3.29), neglecting the dispersion, we have

$$G_2(\delta) = \left\{ 1 + 2 \exp\left[-\left(\frac{\delta}{T_0}\right)^2\right] + 4 \exp\left[-\frac{3}{4}\left(\frac{\delta}{T_0}\right)^2\right] \cos(\omega_1 \delta) + \exp\left[-\left(\frac{\delta}{T_0}\right)^2\right] \cos(2\omega_1 \delta) \right\} \quad (3.38)$$

Therefore the FWHM pulse widths for the three components of an I2PC signal are:

$$I_{2\omega} \propto \exp(-4 \ln(2) \left(\frac{\delta}{T_0}\right)^2) \quad I_{1\omega} \propto \exp(-3 \ln(2) \left(\frac{\delta}{T_0}\right)^2) \quad I_{0\omega} \propto \exp(-4 \ln(2) \left(\frac{\delta}{T_0}\right)^2)$$

As compared to the pulse autocorrelation function in Eq. (3.37), the decomposed component $I_{2\omega}(\delta)$ gives the coherent dephasing time scale $T_2^{(02)}$ between energy states $|0\rangle$ and $|2\rangle$; the component $I_{1\omega}(\delta)$ contains the dephasing time scale $T_2^{(01)}$ between $|0\rangle$ and $|1\rangle$ states, and the phase averaged component $I_{0\omega}(\delta)$ has contribution from both the coherent polarization decay $T_2^{(01)}$ and the incoherent population decay T_1^1 at the intermediate state $|1\rangle$.

So the fitting formulas for all three components are constructed as the convolution between the coherent or incoherent dynamical decay and the phase-averaged laser auto-correlation, where single exponential decay kinetics in a regular OBE function is used and the FWHM pulse width is τ .

$$I_{2\omega}^{fit}(\delta) = c_0^{2\omega} \int_{-\infty}^{\infty} e^{-\frac{|\delta-t|}{T_2^{02}}} e^{-4 \ln(2) \left(\frac{t}{\tau}\right)^2} dt \quad (3.39.1)$$

$$I_{1\omega}^{fit}(\delta) = c_0^{1\omega} \int_{-\infty}^{\infty} e^{-\frac{|\delta-t|}{T_2^{01}}} e^{-3 \ln(2) \left(\frac{t}{\tau}\right)^2} dt \quad (3.39.2)$$

$$I_{pa}^{fit}(\delta) = c_0^{pa} \left(1 + c_1 \int_{-\infty}^{\infty} e^{-\left|\frac{\delta-t}{T_1}\right|} e^{-4\ln(2)\left(\frac{t}{\tau}\right)^2} dt + c_2 \int_{-\infty}^{\infty} e^{-\left|\frac{\delta-t}{T_2}\right|} e^{-3\ln(2)\left(\frac{t}{\tau}\right)^2} dt \right) \quad (3.39.3)$$

Therefore through the fitting process, we can determine the various coherent and incoherent kinetic decay time scales. Compared with solving the complicated OBE, this fitting procedure is much simpler and requires much smaller computation resources along with much shorter computation time.

Nessler et. al. first applied this fitting procedure to the study the hot electron dynamics in a High T_c superconducting material Bi2212 [74] and observed the temperature dependent electron lifetimes; their results exhibit apparently inverse square rule due to e-e scattering predicted by Eq. (3.10) [51, 75].

Chapter 4

2PP Measurements on TiO₂ Surfaces

This chapter gives a fundamental discussion about the two-photon photoemission spectroscopy of bare TiO₂ surfaces. Results are reported for nearly perfect, i.e. stoichiometric surfaces and reduced surfaces. The stoichiometric rutile crystal has a band gap of 3.05 eV. The sample reduction can be accomplished by introducing surface or bulk oxygen vacancy defects. For each O atom removed, two electrons are transferred to the lowest unoccupied states corresponding to the t_{2g} symmetry Ti 3d-orbitals. The excess surface charge is distributed over more than ten five-coordinate surface terminal sites [10]. Although no single Ti ion receives the full one electron charge, we adopt the conventional Ti³⁺ label for the reduced ions [1, 42]. The DOS of these Ti³⁺ defect states is distributed in a broad band at 0.7 ~ 1.0 eV below the Fermi level as already introduced in Chapter 1 [10, 76]. The introduction of oxygen defects raises the Fermi level from the midgap, where it would be for the stoichiometric sample, to 0.1 eV below the conduction band [77]. The energy diagram for a defective TiO₂ crystal along with its 2PP spectrum is illustrated in Fig. 4.1.

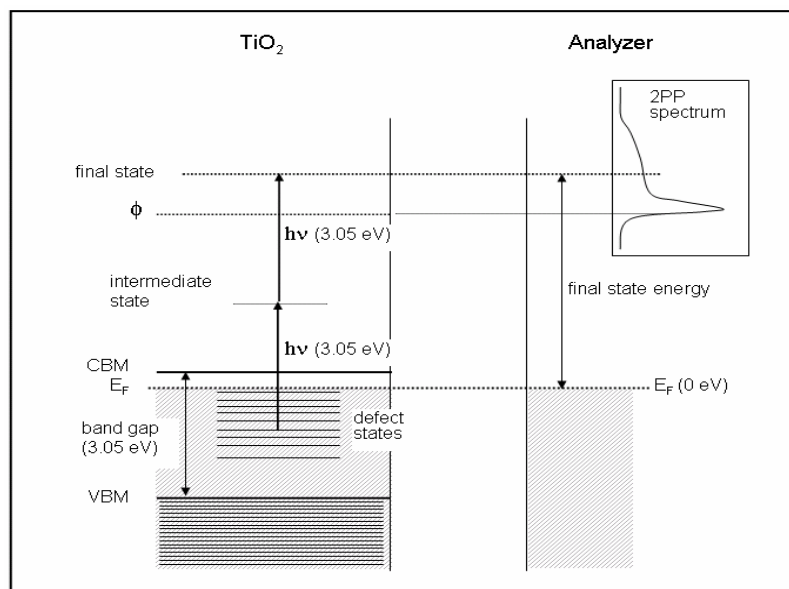


Figure 4.1 Energy diagram for a defective TiO_2 crystal and 2PP measurement with the electron energy analyzer. E_F , Φ , CBM and VBM represent the Fermi level, the work function, the conduction band minimum and the valence band maximum, respectively.

4.1 2PP Spectra for Various Bare TiO_2 Surfaces

Typical 2PP spectra of bare $\text{TiO}_2(110)$ surfaces prepared by four different methods, are plotted in Fig. 4.2. All the data are measured at 90 K. For each surface, we prepare first the stoichiometric surface through a standard recipe. The surface is sputtered by 1000 eV Ar^+ ion with a flux of $10 \mu\text{A}/\text{cm}^2$ for about 15 minutes to remove surface impurities, and then it is annealed for 45 minutes at about 900 K under an oxygen atmosphere (O_2 partial pressure 4×10^{-7} mbar). Following the annealing procedure, the sample is cooled down to the room temperature under the

same O₂ environment). Other surfaces are generated through additional UHV treatment, e.g. vacuum annealing or electron bombardment.

The weakest spectrum in Fig. 4.2 rising from the vacuum edge at 5.5 eV is that of a stoichiometric surface. Other spectra reflect different degrees of surface reduction by various methods. The second weakest spectrum starting at 5.0 eV is of the electron-irradiated surface prepared by exposure of the stoichiometric surface to a 0.5 mC/cm² dose of 500 eV electrons. The spectrum starting at 4.8 eV is that of an annealed surface prepared by heating the stoichiometric surface at 1000 K in vacuum for 30 min. Finally, the strongest and broadest spectrum is prepared by Ar⁺ sputtering the stoichiometric surface for 20 min (1000 eV energy, with a 2 μA/cm² sample current). Note that the 2PP spectra in Fig. 4.2 are typical for these specific preparation methods; however, the intensities and work functions exhibit some variation between the same preparations due to factors that are difficult to control.

As shown in the energy diagram in Fig. 4.1, the high-energy edge in 2PP spectra in Fig. 4.2 at around 6.1 eV corresponds to two-photon photoemission of electrons from the Fermi level. Photoemission from the Fermi level is observed for all preparation methods, but the intensity near the Fermi level increases with the defect concentration. This is to be expected since the initial annealing procedure, which changes the sample color from transparent to blue and makes the sample conductive, introduces bulk defects that cannot be removed by subsequent surface preparation procedures. The low-energy edge corresponds to the minimum energy for excitation of an electron to a freely propagating state in vacuum, i.e., the vacuum level. We confirmed this

assignment by demonstrating the low-energy edge coincides with the threshold energy for the secondary electron emission when the sample is irradiated by 500 eV electrons. The vacuum energy range of 4.3 to 5.5 eV sets the limit for the lowest energy of initial states that can be accessed by 2PP of 1.7 to 0.6 eV below the Fermi level. Considering the large band gap and the pinning of the Fermi level close to the conduction band minimum, photoemission can only occur from the defect states within the band gap; carriers excited from the top of the valence band to the bottom of the conduction band indicated in Fig. 4.1, have insufficient energy to be excited above the vacuum level by subsequent absorption of another 3.05 eV photon.

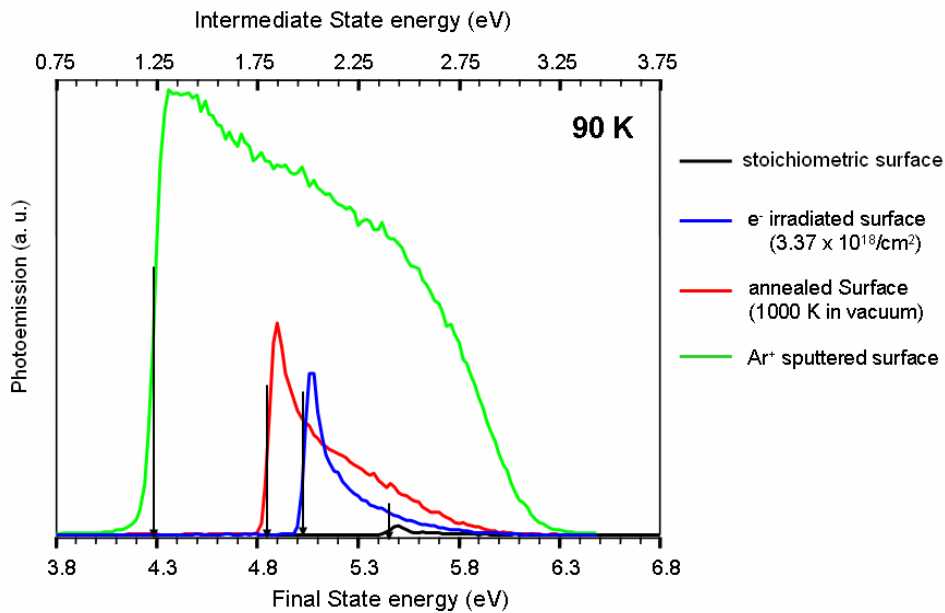


Figure 4.2 2PP spectra of stoichiometric, electron-irradiated, vacuum annealed, and Ar⁺ sputtered surfaces at 90 K. The top and bottom axes give the intermediate and final state energy respectively, in two-photon excitation from occupied states below the Fermi level. Energies are given with respect to the Fermi level throughout the thesis.

The work function for each surface is defined as the half maximum of the lowest energy edge of the 2PP spectra. Based on this definition, work functions for the stoichiometric surfaces in our measurements range between 5.5-5.7 eV. Work function is one of the most fundamental properties of a solid surface, which has rarely been studied for metal oxides [48]. It is usually discussed in terms of a sum of potentials required to overcome the bulk electrostatic chemical potential and to transport electrons through the surface dipole layer [78]. The difference in work functions between different surface preparations can be explained by a simple model, which considers how the surface defects and adsorbates modify the surface potential. As in the standard models for work functions of metals, the electron density extends beyond the image plane into the vacuum. The excess negative charge extending into vacuum is compensated by a net positive charge on the surface ions [78]. Since oxygen has strong electron affinity, which generates a negatively charged surface, the removal of oxygen reduces the negative charge, and therefore, reduces the work required to transport electrons into vacuum. Consequently, lower work function correlates with higher concentration of surface oxygen vacancies.

Compared with the changes in the work function, the difference in intensity distributions of 2PP spectra is not as easy to explain. Since the estimated electron escape depth at ~ 6 eV is ~ 100 Å [78], the 2PP spectra are sensitive to both surface and bulk defects. The intensities in 2PP spectra depend on the joint occupied and unoccupied DOS, and to a lesser extent, the energy dependence of transition moments coupling the initial, intermediate and final states, as well as the intermediate state lifetimes. In addition to the primary photoexcitation process, the 2PP spectra

can also have contributions from secondary electrons, which suffer energy and momentum exchanging collisions in the intermediate or final states prior to being emitted into vacuum. In resonant UPS spectra, the Ti^{3+} defect DOS forms a peak symmetrically distributed about a binding energy of 0.8 eV [9, 73]; however, in our spectra the defect induced signals decrease monotonically from the vacuum edge corresponding to the initial energy state of 1.7 eV below the Fermi level up to the Fermi level. The reason why a distinct peak may not be observed can be attributed to several factors including the overlap of the Ti^{3+} feature with the secondary electrons, the convolution of the initial and intermediate state DOS in the 2PP spectra, the different final state resonance conditions, energy dependent intermediate state lifetimes, and the higher spectral resolution than in the previous studies.

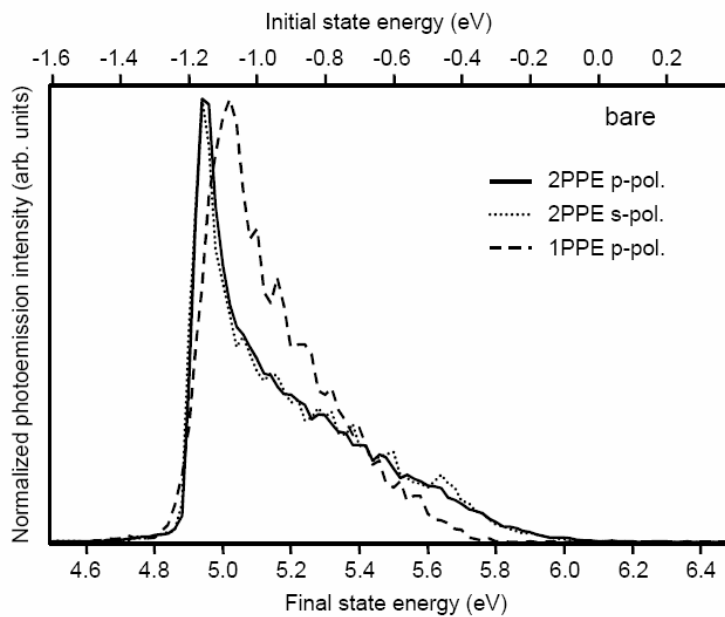


Figure 4.3 Photoemission spectra of bare Ar^+ sputtered surface at 100 K measured with different modes of excitation. The solid and dotted lines represent 2PP measured with p- and s-polarized 3.05 eV light. The dashed line represents one-photon photoemission measured with p-polarized 6.1 eV light [29].

In order to further characterize the defect DOS, we measure photoemission with different polarizations and employ one or two-photon excitation to the same final state. Fig. 4.3 compares the normalized 2PP spectra of Ar⁺ sputtered surface excited with 3.05 eV p- and s- polarized light and one photon photoemission (1PP) excited by 6.1 eV p-polarized light. The surface was generated through 1000 eV Ar⁺ sputtering the stoichiometric surface for 10 min with a sample current of 2 $\mu\text{A}/\text{cm}^2$. The 2PP spectra are independent of the polarization and quite similar to the 1PP spectrum. The similarity of the 2PP spectra with the 1PP spectra indicates that the later is mainly determined by the occupied DOS. However, the enhancement of 2PP spectra near the Fermi edge with respect to the 1PP may reflect a weak contribution to the joint DOS from the e_g symmetry of the Ti⁴⁺ intermediate state at ~ 2 eV above the CBM. It is interesting to note that the p- and s-polarized spectral distributions are identical. The similarity may indicate random direction of the one-photon transition moment with respect to the surface normal, which can happen for a disordered surface, or it indicates that the same initial and final states are coupled by a coherent two-photon transition [50].

Through the study of the photoemission spectra from the bare surfaces in Fig. 4.2 and Fig. 4.3, we conclude that they are mainly due to the initial states present in the band gap of TiO₂ on account of the O atom vacancy defects. These states can be generated with different distributions by various preparation techniques. The low-energy edge of the 2PP spectra gives an accurate value of the work function averaged over the irradiated spot on the surface. The 2PP spectra are

quite sensitive to the work function changes. The photoemission intensities are approximately proportional to the DOS of the occupied band gap states.

4.2 Oxygen Adsorption on TiO₂ Surfaces

In this section, we mainly discuss about the interaction of O₂ with TiO₂ surfaces after various preparation procedures and compare our experimental data with the existing model for O₂-TiO₂ interaction. Because Ti is such a reactive element, oxygen-deficient surfaces are clearly expected to react with O₂ and other adsorbates. Also, in order to investigate the photocatalytic reactions on TiO₂ surfaces, we also study how O₂ affects the defect concentration and the work function of TiO₂.

Molecular oxygen is adsorbed on TiO₂ surfaces through a leak valve into the UHV chamber to achieve specific exposures measured in Langmuir (L) (1 L = 10⁻⁶ Torr×s) at ~100 K. The changes in the surface structure are deduced from 2PP spectra taken immediately after the exposure. Fig. 4.4 shows the model for how O₂ molecules adsorb on TiO₂(110) surfaces proposed by Henderson et. al. [79]. Oxygen molecules strongly bind to oxygen-deficient surfaces to fill the bridging oxygen vacancy sites. However, after the O atom vacancy defects are titrated (removed by reaction with O₂) they are not adsorbed on stoichiometric surfaces under our experimental conditions (~ 90 K) [79]. The reduced Ti ions associated with a bridging oxygen (BO) vacancy site, i.e. $Ti^{+4-\delta}$ which are active in the O₂ adsorption and relevant photocatalytic reactions on TiO₂ surfaces. By introducing an O atom vacancy or other means of surface

reduction (e.g. H atom forming a bridging -OH species) the excess electrons are spread over several Ti sites indicated in Fig. 4.4, as $Ti^{+4-\delta}$ instead of more commonly, but less accurately Ti^{3+} . These reduced Ti ions are the adsorption and reaction sites of electrophilic molecules such as O_2 .

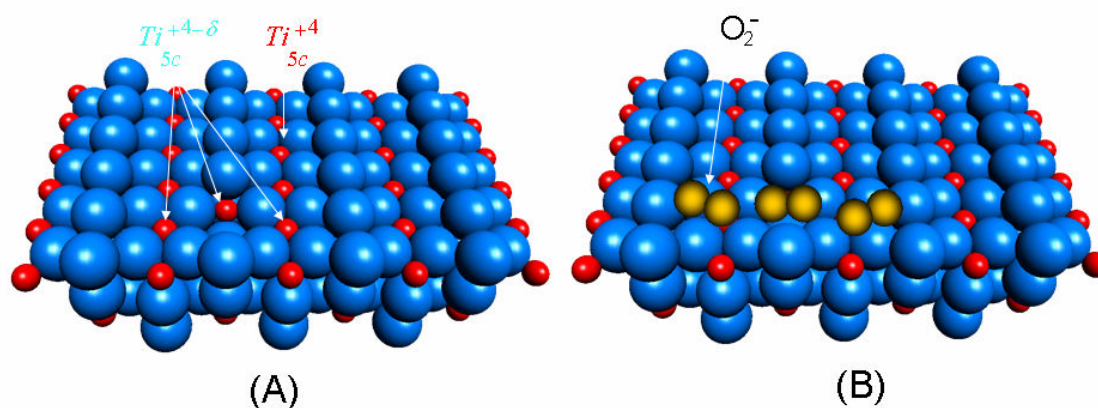


Figure 4.4 Diagram of the O_2 adsorption on an Oxygen-deficient $TiO_2(110)$ surface. (A) An O atom vacancy is surrounded by reduced Ti ions. (B) O_2 binding and interacting with the reduced Ti ions ultimately to remove O atom vacancies..

In Henderson's model, O_2 molecules bind in the vicinity of an O atom vacancy and form O_2^- species surrounding the vacancy. Those O_2^- species are very active in photo-oxidation of CO or NH_3 , and dissociation of H_2O , which were discussed in O_2 co-adsorption studies with these molecules [1, 80, 81]. According to Henderson, these oxygen molecules and species are stable at room temperature, and desorb at around 400 K. This model, however, is not supported by our observations.

4.2.1 O₂ does not Adsorb at the Stoichiometric Surface

First, let us look at the interaction of O₂ molecules with a stoichiometric TiO₂ surface. The concentration of O atom vacancies is minimum because the sample is annealed and cooled in O₂ atmosphere, as discussed previously. In Fig. 4.5, we observe that exposing the perfect surfaces oxygen to up to above 30 L of O₂ barely changes the 2PP spectra. The spectrum shows weaker emission just above the vacuum level. The upturn of emission at the vacuum level is most likely due to the secondary electron scattering on a rough surface. The effect of exposure is to reduce this secondary emission possibly indicating that the surface becomes less rough, however, the negligible up-shift in the vacuum level indicates that O₂ does not adsorb on stoichiometric surfaces. This result is consistent with other observations and theoretical predictions that O₂ does not adsorb on perfect surfaces even at 90 K [82, 83].

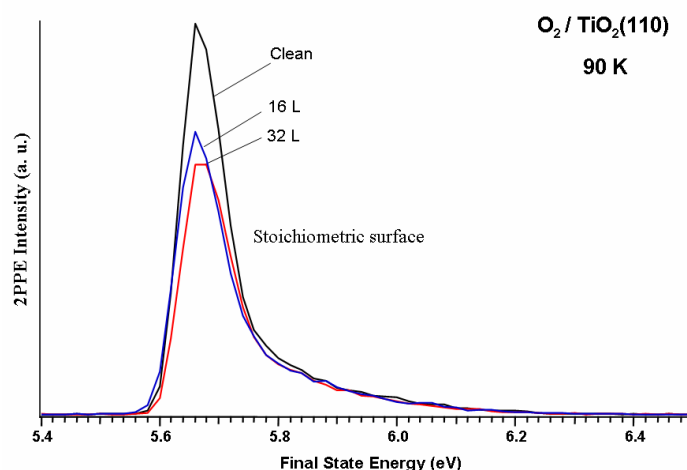


Figure 4.5 The effect of O₂ exposure on the 2PP spectra of the stoichiometric surface.

4.2.2 O₂ Adsorption at the TiO₂ Sample with Surface Defects

By contrast to the stoichiometric surface, the O₂ oxygen adsorption on reduces surfaces, such as the electron-irradiated surface shown in Fig. 4.6, produces dramatic changes in the 2PP spectra. The electron-irradiated surface is prepared by irradiating the stoichiometric surface with a dose of 0.5 mC/cm² 500 eV electrons. The thick solid line in Fig. 4.6 (a) shows the bare electron irradiated surface, while the much less intense spectra are the O₂ oxygen exposed surfaces. In order to display the 2PP spectra with substantially diminished intensity after the O₂ exposure, in Fig. 4.6 (b), we give the expanded spectra in the indicated region of Fig. 4.6 (a). The thin solid lines in Fig. 4.6 (b) represent photoemission after exposing the surface with 0.06 and 0.3 L O₂, while the dashed line represents the stoichiometric surface before electron irradiation. Further O₂ dosing does not change the 2PP spectra. Remarkably, exposure to only a fraction of one monolayer of O₂ restores the stoichiometric surface spectrum at 100 K. After it is restored by oxygen dosing, the surface is further heated up to 450 K for a 5 min. and cooled back to 100 K. The 2PP spectrum after this heating-cooling procedure cycle is shown by the thin dotted line in Fig. 4.6 (b). There is almost no change in the 2PP spectra after this procedure, indicating the surface is restored to the stoichiometric condition by exposing to sub-monolayer dose of O₂ at 100 K.

Our observation of defect healing at 100 K contrasts with those of Henderson and Lu et al. [79, 83] who report that vacuum annealed surface healing of oxygen vacancies requires heating of the surface to temperature in the range of 150 to 400 K. We will show in the next section that these

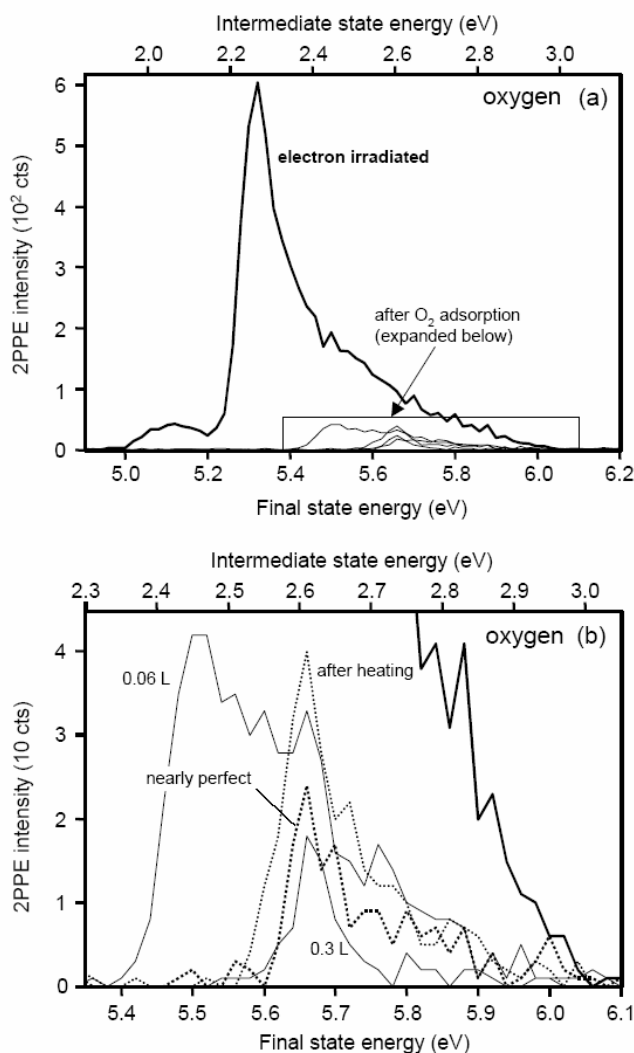


Figure 4.6 (a) 2PP spectra of electron-irradiated surface at 100 K before and after exposure to oxygen molecules. The thick solid line is the bare surface after electron irradiation with a 0.5 mC/cm^2 at 500 eV. (b) is the expanded spectra in the indicated region of (a). The thick dotted line gives the stoichiometric surface. Thin solid lines give the electron-irradiated surface after exposure to 0.06 and 0.3 L of O_2 . The dotted line represents the spectrum after heating the oxygen exposed surface to 450 K and subsequent cooling to 100 K.

activated healing processes may involve subsurface oxygen defects that exist on annealed sample surfaces, but not on electron irradiated surfaces. Our observation of efficient healing at 100 K after submonolayer exposure suggests that O₂ is adsorbed with a high probability in a weakly bound state with high surface mobility. And this efficient healing implies that mobile, weakly bound O₂ is irreversibly trapped most likely by dissociation into O²⁻ at the bridge O atom vacancy sites.

4.2.3 O₂ Adsorption at the Sample with Both Surface and Sub-surface Defects

The same O₂ adsorption/heating procedure is repeated for the vacuum annealed surface (1000 K for 30 min), which is cooled to 100 K before the measurements. The 2PP spectra (thick solid line) in Fig. 4.7 (a) show that this treatment reduces the work function by 0.7 eV and significantly increases the intensity compared with the stoichiometric surface (dashed line). The annealed surface is exposed to a range of O₂ doses (0.1 to 4.0 L) and 2PP spectra shown by thin solid lines are taken after each exposure. By contrast with the electron irradiated surface, the work function of oxygen-exposed surface increases more gradually as the dosage is increased, and even after exposure to 4.0 L of O₂, the spectrum does not return to the original stoichiometric surface. The work function saturates at 5.2 eV at the high exposure of oxygen, which is substantially below that of the stoichiometric surface. Moreover, the 2PP intensities change in a different manner during the O₂ exposure, and do not decrease like for the electron-irradiated surface. The behavior of this surface after the heating procedure (dotted line) is also

substantially different with the electron irradiated surface: the work function reverts to that of the original bare annealed surface, although the intensity at high energies is decreased by this procedure.

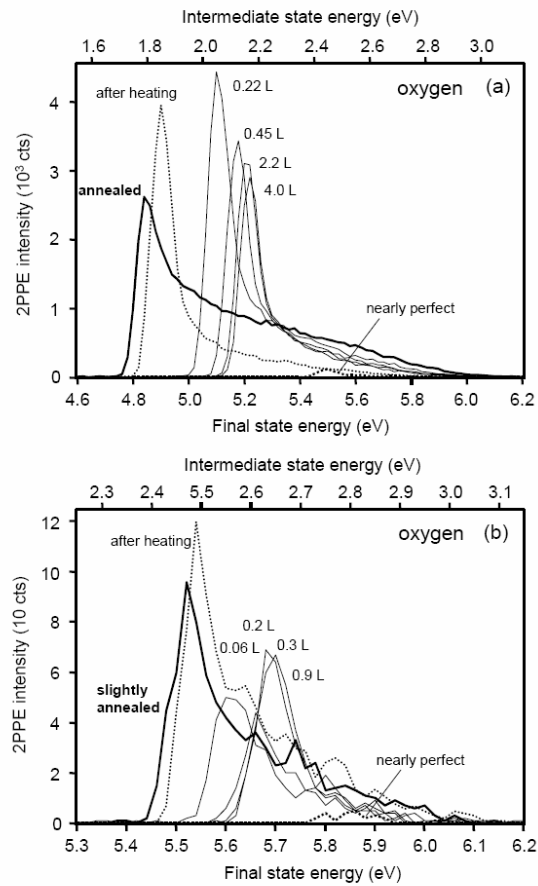


Figure 4.7 2PP spectra of vacuum annealed surfaces before and after exposure to O_2 . (a) The annealed surface prepared by heating to 1000 K for 30 min in vacuum. (b) Mild annealing condition by heating surface to 900 K for 10 min. In both figures, dashed lines represent the clean surface taken at 100 K immediately after the preparation. The thin solid lines represent spectra of oxygen-exposed surfaces for different dosages. The dotted lines represent spectra of surfaces that have been exposed to O_2 , annealed briefly to 450 K and subsequently cooled to 100 K.

Since the heavy annealing procedure probably creates a drastically different surface compared to the electron-irradiated surface, we also prepared a “slightly annealed” surface by heating the sample in vacuum at 900 K for 10 min, followed by oxygen dosing. In Fig. 4.7 (b), we can easily observe this procedure generates more modest changes in 2PP spectra. The work function change (-0.4 eV) is comparable to the electron-irradiated surface, however, the behavior upon O₂ dosing and heating is entirely consistent with the trends observed for the heavily annealed surface. The only difference is the dosage of O₂ at which the spectral changes saturate decreases to ~ 1 L. The different behavior of electron irradiated and vacuum annealed surfaces in Fig. 4.6 and Fig. 4.7 demonstrate that the two reduction procedures create different defect distributions.

Thermal annealing of the surface will produce a distribution of defects at the surface and diffusion into the bulk; while with electron irradiation, the defects are generated mainly at the surface, and below 100 K their diffusion into the bulk is suppressed. Thus, on the bare electron irradiated surface, the work function and intensity distribution of 2PP spectra are determined by the surface defects, mainly bridging oxygen vacancies. Molecular oxygen effectively heals the surface defects at 100 K, and therefore, the 2PP spectra are restored to that of a stoichiometric surface. By contrast, the 2PP spectrum of the vacuum annealed surface is dominated by subsurface defects. The escape depth of 6 eV electrons corresponds to 30 layers ($\leq 100 \text{ \AA}$) according to the universal curve for the electron scattering lengths. The integration of the bulk defect signal over this escape depth can easily overwhelm the surface contribution. Evidence for the strong contribution from the bulk defects can also be seen in the large signal from the

secondary electrons at the work function edge. Oxygen adsorption on the annealed surface can heal the surface defects and produce a substantial increase in the work function. However, the secondary electron intensity does not decrease indicating that the sub-surface region is still disordered. According to Lu and Henderson, molecularly adsorbed oxygens are photochemically labile at 100 K, and dissociate to atomic species with thermal activation to heal defects in the temperature range of 150-400 K. This activated dissociation may arise from the diffusion of existing subsurface defects to the surface where they can be healed with the pre-adsorbed O₂ molecules, regenerating the surface defects [79, 83]. This interpretation is comparable to the STM images of the annealed TiO₂(110) surfaces, where two types of oxygen vacancies with densities of 7 and 1-2% that have been assigned, respectively, to the surface bridging oxygen vacancies, and to subsurface vacancies [84].

4.2.4 O₂ Adsorption on the Heavily Damaged TiO₂ Surface

Finally, in Fig.4.8, we present the spectral changes following the interaction of O₂ with Ar⁺ sputtered surface (1000 eV, for 3 mC/cm²) using the same procedures as above. Exposing the bare Ar⁺ sputtered surface to O₂ can eventually increase the work function to 0.1 eV above that of the stoichiometric surface. However, the 2PP spectra after O₂ exposure have much higher intensity than the stoichiometric surface indicating that some defects cannot be healed at 100 K. By heating up to 400 K, the work function is reduced in a similar feature as the annealed surface, but this shift does not reach as low as the original sputtered surface.

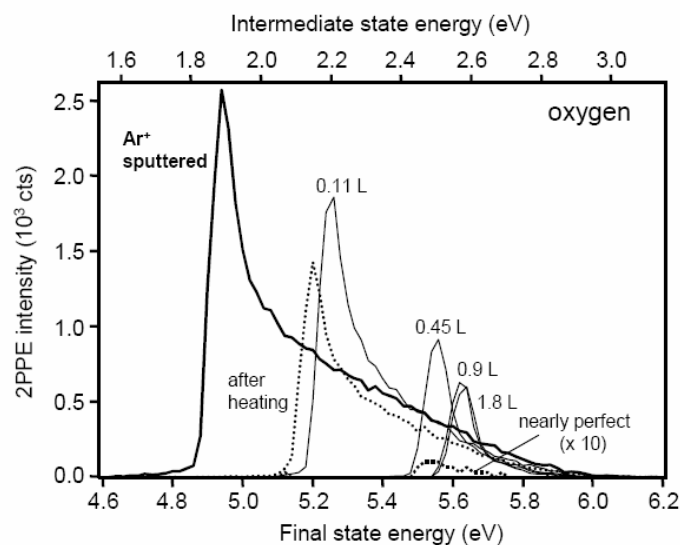


Figure 4.8 2PP spectra of Ar^+ sputtered surfaces before and after exposure to oxygen. The dashed line is the amplified spectrum of the stoichiometric surface by 10 times. The thick solid line is the bare Ar^+ sputtered surface. The thin solid lines represent the spectra of oxygen-exposed surface for several dosages. The dotted line represents the oxygen-exposed surface spectra after heating to 450 K and subsequent cooling to 100 K.

Argon ions, similar to electrons, cause non-thermal damage to the surface. However, Ar^+ can transfer much larger momentum to the surface and therefore induce much more damage, including subsurface defects. Previous XPS measurements of Ar^+ sputtered surfaces show evidence for defects with the valence of titanium Ti^{n+} , n ranging from 0-3 [85]. These vacancies cause strong intensity and very low work function in the 2PP spectra. When exposed to oxygen, a significant fraction of vacancies is healed because they exist mainly at the outmost layer. The

reason why the work function exceeds that of the stoichiometric surface is not understood, but it is possible that the concentration of oxygen on the sputtered surfaces after saturation exposure is even larger than for the stoichiometric surface, leading to a higher work function. When the sample is heated to 450 K, the work function substantially decreases indicating that the reduction of surface oxygen concentration is facile. This can happen either by diffusion to the surface of the shallow defects remaining after the low temperature exposure to O₂ or desorption of weakly bound oxygen species from the disordered surface.

The above experimental results on interaction of oxygen molecules with stoichiometric and damaged surfaces demonstrate that the high sensitivity of 2PP to the work function and the concentration of near surface defects. The 3.05 eV excitation can only induce two-photon photoemission from the defect states hence it provides considerably higher sensitivity to defects as compared with the other standard surface science techniques. The characterization of surface defects is important because they serve as the initial states in the 2PP process, and they govern how molecules like H₂O and CH₃OH chemisorb on TiO₂ surfaces.

Chapter 5

Observation of Wet Electrons at the $\text{H}_2\text{O}/\text{TiO}_2$ (110) Surface

The following chapter will cover the 2PP spectroscopy and dynamics of the $\text{H}_2\text{O}/\text{TiO}_2$ system. For many reasons, water is probably the most important adsorbate at the TiO_2 surfaces. For example, photocatalytic processes usually are performed in an aqueous environment, where both the molecular water and the surface hydroxyl (-OH) species can easily affect adsorption and reaction processes [1, 11]. Moreover, water molecules comprise one of the main residual gas components in UHV environment, hence it is a typical adsorbate even in under well-controlled conditions. Recent STM measurements have demonstrated that O atom vacancy defects and bridging -OH species formed by the dissociation of residual water are difficult to distinguish in the unoccupied state STM images [86]. Because water is central to many applications of TiO_2 , its adsorption on TiO_2 surface has been intensively investigated with a variety of experimental and theoretical techniques.

5.1 The Model for H₂O Adsorption on the TiO₂(110) Surface

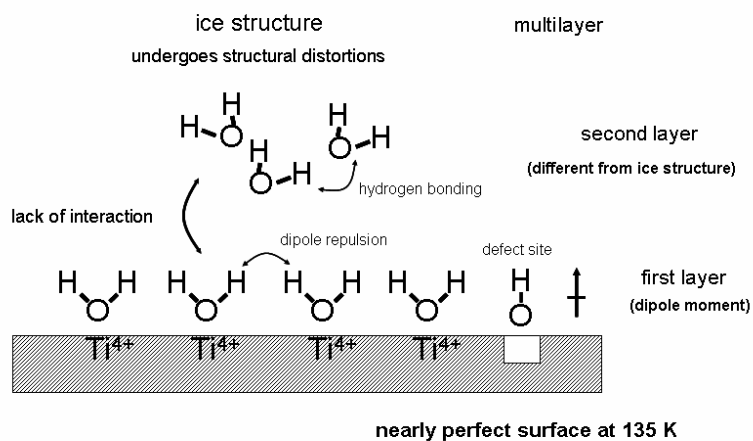


Figure 5.1 The model for H₂O/ TiO₂ interface.

A cartoon of the adsorbed multilayer H₂O interaction with TiO₂ (110) rutile surfaces is shown in Fig. 5.1, and the strongest interaction between H₂O and TiO₂ occurs at the bridging O atom vacancies. For each vacancy, single H₂O molecule dissociates to form two uncorrelated surface -OH species on the bridging O atom rows. Based on Temperature Programmed Desorption (TPD) and High Resolution Electron Energy Loss Spectroscopy (HREELS) measurements, Henderson proposed a structure for multilayer H₂O adsorbed on TiO₂(110) surface in Fig. 5.1 [46]. According to this model, after the existing O atom vacancy defects are removed by water dissociation, the subsequent first layer of water molecules adsorbs in channels between the bridging oxygen atoms. H₂O forms bonds through its oxygen and single H atom to the terminal

five-coordinate Ti^{4+} sites (Fig. 1.2) and the bridging O atoms, respectively. The remaining H atoms form hydrogen bonds (HB) with neighboring water molecules, thereby forming linear hydrogen chains along the [001] rows (Fig. 5.2). The second layer of water adsorbs on top of the first monolayer, however, since almost all the H atoms in the first monolayer are engaged in favorable hydrogen bonds, the interaction between the first and second monolayers is weak. Thus, Henderson concluded that water molecules make separate hydrogen bonding networks between the first and second layers, which lead to the formation of amorphous ice structure. According to Henderson, the hydrogen bonding within the second layer occurs with retention of the non-hydrogen bonded OH stretch of the -OH species on the bridging O rows [46]. Those -OH species drastically change the surface charge distribution, and thus have essential different influence on the upper layer structures of H_2O compared to the molecular H_2O [87, 88].

Fig. 5.2 (a) gives the density functional theory (DFT) calculated electronic structures of 1 monolayer (ML) H_2O covered rutile $TiO_2(110)$ surface to show in detail of how the surface provides a template for the first and subsequent H_2O monolayer chemisorption, and to provide more quantitative information regarding to intermolecular hydrogen bonds at the surface [76, 89]. More specifically, the distance between two adjacent five coordinate terminal Ti_{5c}^{4+} ions (indicated by blue arrows) of 2.96 Å on rutile (110) surface is slightly longer than the 2.76 Å maximum in the radial distribution function between two oxygen molecules in liquid H_2O [90]. As shown in Fig. 5.2 (a), this slight mismatch favors formation of stronger molecule-surface HBs involving the bridging O atoms and weaker intermolecular HBs, leaving one H atom of each adsorbed H_2O remain weakly hydrogen bonded.

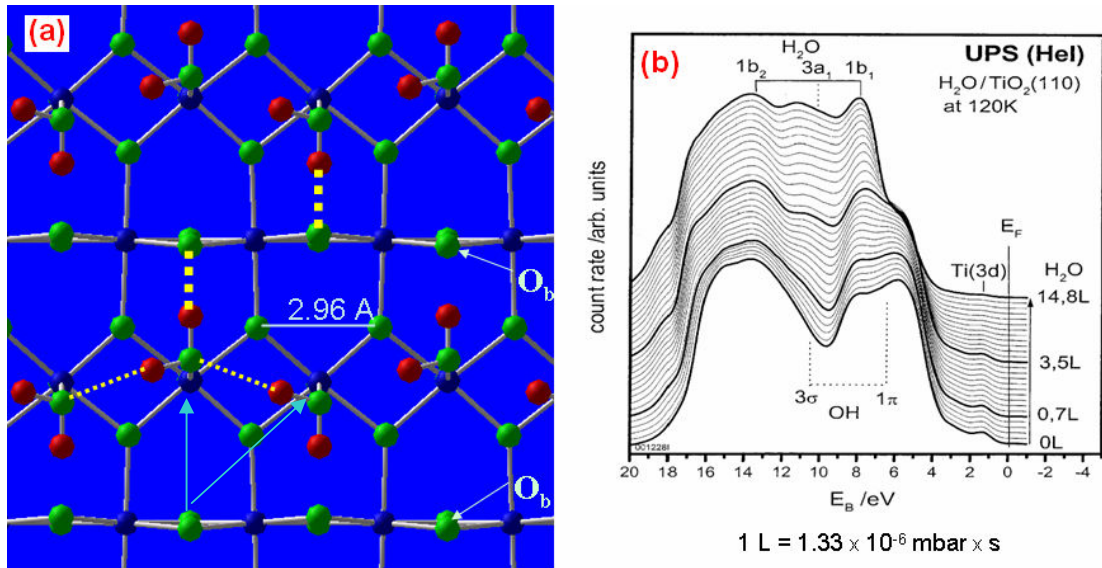


Figure 5.2 (a) The calculated structure for chemisorption of 1ML H₂O on TiO₂(110) surface, where Ti atoms are blue, O atoms are green and H atoms are red. Dotted lines indicate strong (thick) and weak (thin) hydrogen bond, the blue arrows indicate the terminal Ti_{5c}^{4+} ions and the white arrows indicate the bridging O atoms [89]. (b) UPS (HeI) spectra for TiO₂ (110) surface exposed to water at 120 K [45].

In Fig. 5.2 (b), we show the reported UPS spectra following the adsorption of H₂O on TiO₂ surface by Krischok et al. [45]. In these measurements, the contribution from both the dissociated and molecular water are displayed, which mainly modify the DOS of the O (2p) valence band structure, and to some extent the defect related Ti³⁺ band gap states. Initially, the spectra are dominated by the -OH species (3σ or 1π orbitals in Fig. 5.2 (b)) generated through the dissociation of H₂O at the O atom vacancy defect sites (Fig. 5.1). When these defect sites are titrated, water adsorbs molecularly at the terminal Ti sites (1b₂, 3a₁ and 1b₁ orbitals in Fig.5.2 (b)). So the UPS spectra show a clear trend of switching from being dominated by the

dissociative species (OH) at low coverage, to the molecular species (H₂O) at high coverage. This feature however provides a complementary quantitative evidence to support the proposed model of monolayer H₂O chemisorption and dissociation at the TiO₂ (110) surface discussed in Fig. 5.1.

5.2 H₂O Adsorption on Various TiO₂ Surfaces: the Work Function Change

In this section, we investigated how the chemisorption of water affects the work function of TiO₂ surfaces after different preparation techniques. Figure 5.3 shows the work function change in 2PP spectra (p-polarized excitation) as a function of H₂O adsorption at the stoichiometric TiO₂ surface. We can see that water causes the work function to decrease. The shift is in the opposite direction compared to oxygen, indicating that H₂O acts as an electron donor rather than an acceptor on TiO₂ surfaces. As the dosage is increased, the work function decreases and 2PP intensity increases. The work function change saturates at a high dose of ~ 5 L (data not shown). In order to study the polarization dependence of the 2PP spectrum, we also performed 2PP measurements using s-polarized light, as well as single-photon photoemission with 6.0 eV light (data not shown). The p-polarized light mainly induces the perpendicular dipolar transition to the surface, while s-polarized light induces the parallel dipole transition. The polarization dependence of the 2PP spectra is a reflection of the geometry of the surface electronic structures of both the occupied initial state and the unoccupied intermediate state. Usually, the p-polarized excitation involves a larger transition dipole matrix element, which gives much higher photoemission intensity. These additional spectra are almost identical to those measured by p-

polarized light, except for relatively smaller emission intensity. From this we conclude that the spectra in Fig. 5.3 mainly give the electronic features of the occupied Ti bandgap-states near to the Fermi level.

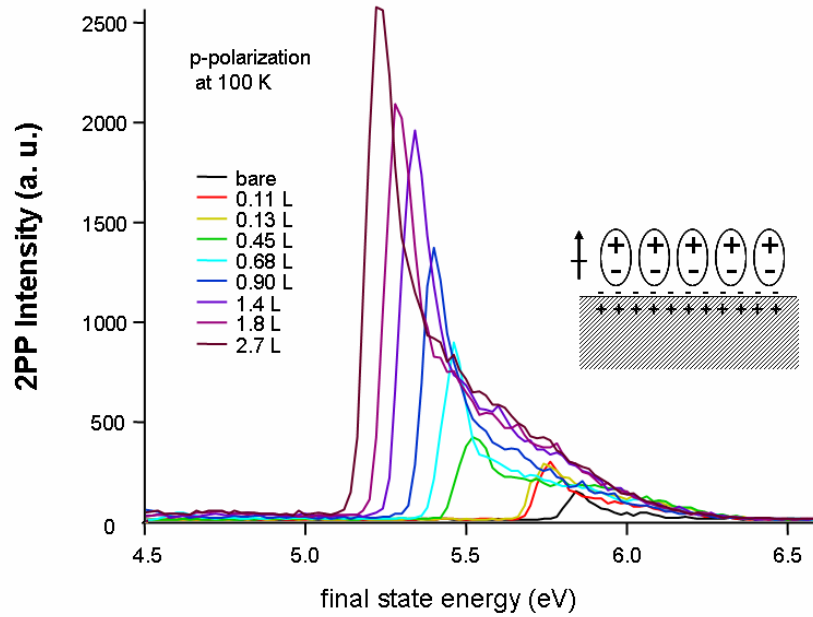


Figure 5.3 2PP spectra for the progressive H₂O adsorption onto a stoichiometric TiO₂ surface.

In order to further characterize the work function change upon water adsorption and quantify the dosage associated with one monolayer coverage, we employ the Helmholtz model to our analysis, where the adsorbate molecules are treated as a surface dipole layer. Therefore, the change in the surface chemical potential through the molecular adsorption affects the work function according to [78, 91]

$$\Delta\phi = \frac{Ne\mu_{eff}}{\epsilon}. \quad (5.1)$$

So the work function change $\Delta\phi$ is proportional to the density of adsorbed molecules N and their effective dipole moment μ_{eff} . Assuming molecules adsorb at every terminal Ti^{4+} site, at the full monolayer coverage the surface density of molecules is $N_0 = 0.52 \times 10^{15} \text{ cm}^{-2}$ [46]. According to the Langmuir adsorption equation $\theta = 1 - \exp(-k \cdot x)$ the coverage density is defined by $N = N_0 \cdot \theta$, where θ gives the coverage in monolayer, k is the adsorption coefficient representing all the effects that determine the adsorption probability and x is the molecular exposure (dosage) measured in Langmuir (Section 4.2).

Moreover, the dielectric constant of a water film is given by $\varepsilon = \varepsilon_0(1 + \chi)$, where the susceptibility χ of the monolayer of molecules has been derived by MacDonald and Barlow in terms of the molecular polarizability α [92]

$$4\pi\chi = \alpha\Lambda N^{3/2}, \quad (5.2)$$

where Λ is the molecular structure parameter with approximate value of 9. By combining all of the above equations (Eqs. (5.1-5.2) and those in text), we can obtain the change in the work function as a function of H_2O exposure,

$$\Delta\phi(x) = \frac{e\mu_{eff}N_0[1 - \exp(-k \cdot x)]}{\varepsilon_0 \left\{ 1 + \frac{\Lambda}{4\pi} \alpha [N_0(1 - \exp(-k \cdot x))]^{3/2} \right\}}. \quad (5.3)$$

Because, the polarizability of free water molecules α is very small $\sim 1.45 \times 10^{-24} \text{ cm}^3$ [93], the denominator of Eq. 5.3 can be approximated as ε_0 , thus the Helmholtz model simplifies to:

$$\Delta\phi(x) = \frac{e\mu_{eff} N_0 [1 - \exp(-k \cdot x)]}{\varepsilon_0}. \quad (5.4)$$

The same approach also is used to study the adsorption of water on the electron-irradiated, UHV annealed, and Ar^+ sputtered surfaces. We record the 2PP spectra for each of these surfaces with various amounts of water adsorption, and monitor the “work function change” vs. “ H_2O dosage”, which is plotted in Fig. 5.4 (a). The work function change has a range of -0.8 to -1.2 eV, and saturates after exposure to $\sim 5 \text{ L}$ of water. By contrast to oxygen, adsorption of H_2O appears to be weakly dependent on the defect concentration. The saturation behavior indicates that only the initial growth forms a film with ordered dipole moments and in the subsequent layers, the dipole moment is random or parallel to the surface. The range of work function changes (-0.8 to -1.2 eV) reflects the properties of surfaces prepared by different procedures. The largest work function change is observed for the most electron withdrawing stoichiometric surfaces. Removing surface O atoms by various techniques decreases the electron transfer from H_2O molecules, and therefore, the saturated magnitude of the work function change becomes smaller. As discussed above, water also dissociates at defective surfaces to form pairs of surface $-\text{OH}$ species, and the dissociative chemisorption at defects does not seem to have substantial effect on the work function change [1, 46, 73, 94-96].

The solid curve in Fig. 5.4 (b) represents the least-square fit of the work function change with water coverage to the functional form of Eq. (5.4) for the electron-irradiated surface. The curve reproduces our experimental data well validating the Helmholtz model and Langmuir adsorption kinetics. The derived dipole moment μ_{eff} is 0.48 ± 0.05 Debye and the adsorption coefficient k is $1.49 \pm 0.07 L^{-1}$. Dipole moments derived by fitting the data for other surfaces (different preparation methods) range between 0.45-0.6 D. Our results are consistent with a previous (X-ray photoemission spectroscopy) XPS measurement of $\mu_{eff} = 0.5$ D for water on a stoichiometric $TiO_2(110)$ surface [94], and with 0.4 – 0.8 D for water adsorbed on Ir(110) [97] and Cu(110) [98] surfaces. The effective dipole moment on the metal and metal oxide surfaces is considerably smaller than for free water molecules in the gas phase, where $\mu = 1.8$ D [99]. The similarities between the effective dipole moments on metal and metal oxide surfaces can in part be attributed to the dipole-dipole depolarization, though the structures of water can be considerably different [6, 100]. Finally, we note that the agreement with the Langmuir adsorption kinetics for at least the first monolayer implies that well-ordered $TiO_2(110)$ surfaces under UHV are hydrophilic [101]. According to the similar saturation feature displayed in the various work function change curves in Fig. 5.4 (a) and the data fitting analysis in Fig. 5.4 (b), we tentatively assign the exposure of 1.2 ~ 1.5 Langmuir corresponds to 1 ML coverage of H_2O . We will discuss this further in the next section.

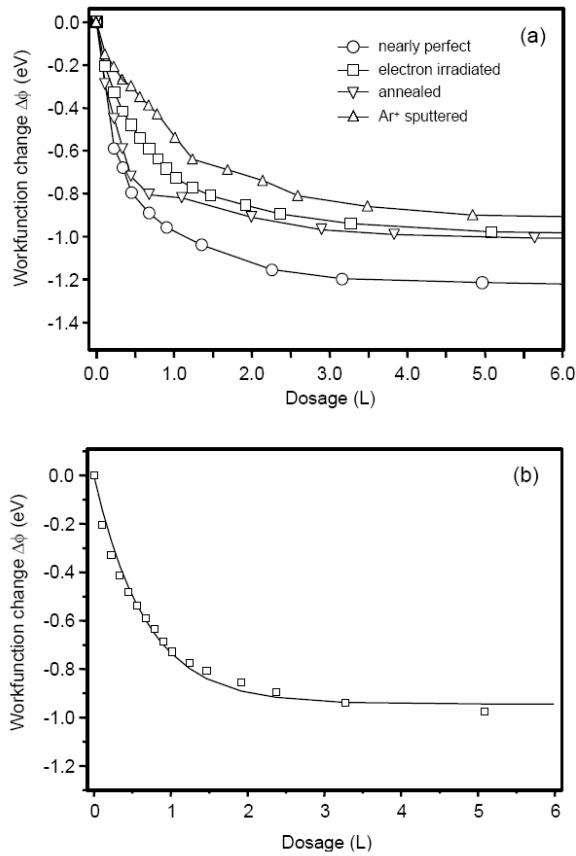


Figure 5.4 (a) The work function change as a function of water dosage for the stoichiometric, electron-irradiated, vacuum annealed, and Ar⁺ sputtered surfaces at $T = 100$ K. Individual data points for each surface are connected to guide the eye. (b) Experimental data (squares) and fitted curve (solid line) of the work function change as a function of dosage for the electron-irradiated surface according to the Helmholtz model (Eq. 5.4) [29].

5.3 The Unoccupied Electronic Structure for H₂O Adsorbed on Defective TiO₂ Surfaces

In addition to the work function change, the adsorption of water leads to another more notable spectral feature that exclusively appears in 2PP spectra of reduced TiO₂ surfaces. Figure 5.5 shows the change in 2PP spectra when reduced TiO₂ surfaces are exposed to H₂O. By contrast to the stoichiometric surface in Fig. 5.3, a new peak at the final energy of ~ 5.5 eV appears from sub-monolayer to multilayer coverages. The peak reaches the maximum intensity for the exposure of ~ 1.3 L water, and decreases to ~ 25% of its maximum value above 3 L H₂O exposure. This new feature is never observed on stoichiometric TiO₂ surfaces. Here, we assign that the dosage of 1.3 L at which coverage the 2PP spectrum shows the maximum resonance intensity is corresponding to the one monolayer (1 ML) coverage of H₂O on the reduced TiO₂ surface [30]. This resonance intensity, proportional to the DOS of the unoccupied states of the specific system, is essentially associated with the available free H atoms i.e. dangling H in the H₂O overlayer structures. The monolayer structure will present the largest population of dangling H, which would be partially consumed through the hydrogen bonding with the second layer of H₂O. The more quantitative discussion regarding to the precise definition of one monolayer (1 ML) H₂O coverage will be involving the DFT calculation of H₂O/TiO₂ surface (Fig. 5.10) given in Section 5.5 [76].

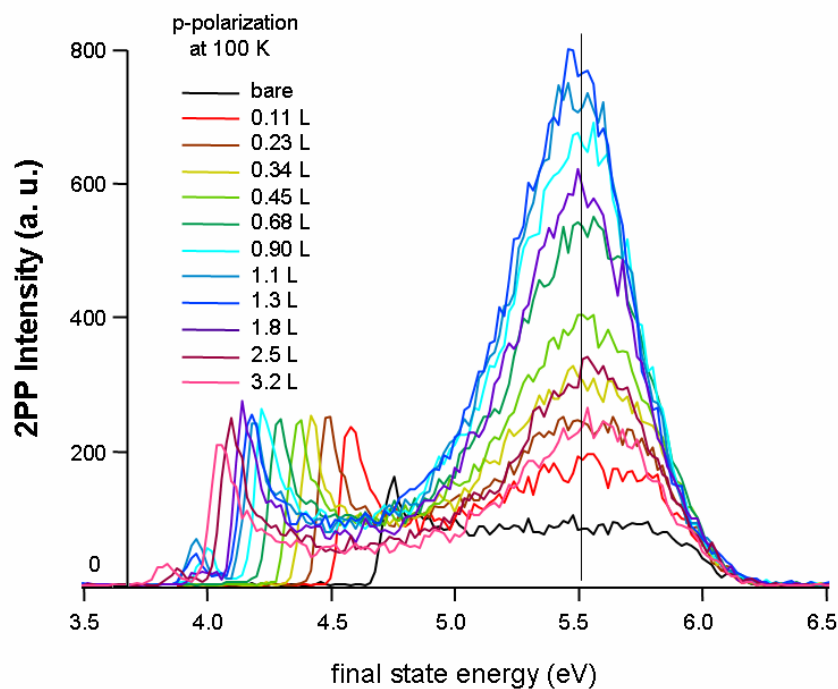


Figure 5.5 2PP spectra for successive exposures of reduced (annealed)TiO₂(110) surface to H₂O.

In Fig. 5.6, we plot the 2PP spectra excited either by p- or s-polarized light for the exposure TiO₂ of ~1.3 L i. e. approximate 1 ML coverage H₂O. The comparison shows that the water-induced peak is mainly excited by p-polarized light. In order to separate the water-induced peak from the bulk 2PP signal, we also show the difference between the p- and s-polarized spectra that have been normalized in the 4.1-4.3 eV region. Such polarization dependent differences do not occur when H₂O is adsorbed on stoichiometric TiO₂ surfaces, or when O₂ is adsorbed on the stoichiometric or reduced TiO₂ surfaces. Furthermore, one-photon photoemission (1PP) spectra excited with 6.0 eV light of the H₂O covered reduced TiO₂ surfaces do not show this resonance, indicating that it is due to an unoccupied intermediate state resonance with a transition dipole

moment normal to the surface. These observations clearly point to assignment to a resonance at an unoccupied state energy of 2.45 eV that is induced by water adsorption [30].

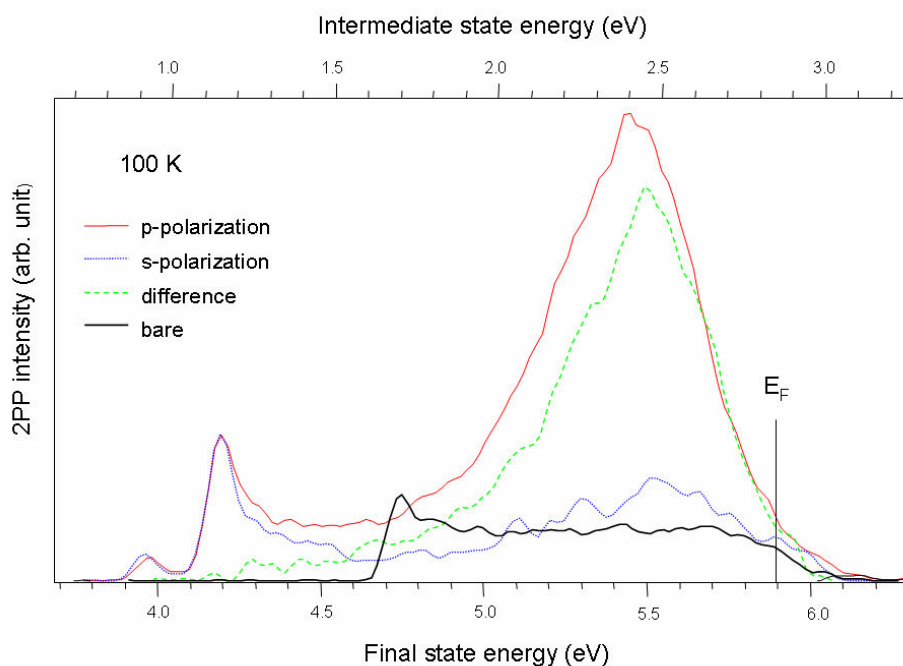


Figure 5.6 2PP spectra of the reduced TiO_2 surface before and after deposition of ~ 1 ML of H_2O . The $\text{H}_2\text{O}/\text{TiO}_2$ spectra are taken with p- and s-polarized light, and are normalized at the intensity of the work-function edge. The difference between the normalized p- and s-spectra (green) for the reduced surface isolates the additional DOS of the wet-electron state. The final energy is measured for the photoelectrons with respect to E_F , whereas the intermediate-state energy is obtained by subtracting the photon energy of 3.05 eV.

Because the H₂O induced electron resonance appears only on the reduced surfaces, where the H₂O molecules dissociate at O atom defects, we consider its assignment based on its dependence on adsorption of both H₂O and OH. This electron resonance states, in which the non-hydrogen bonded -“dangling” H atoms bind and partially hydrate electrons on the surfaces of H₂O overlayer structures show very similar feature as the dubbed “wet-electron” states in 2D environments [102-105], therefore are defined as “wet-electron” states transiently evolving at the H₂O/TiO₂ interface. The H₂O induced wet-electron resonance in the 2PP difference spectra of reduced TiO₂ in Fig. 5.6, which is absent when H₂O is chemisorbed on the stoichiometric TiO₂ surface (Fig. 5.3), is probably caused by a few percent of H₂O that dissociated at O atom vacancy defects to form OH [30]. In Fig. 5.7, we plot the work function change and the integrated wet electron state intensity vs. the H₂O exposure. The resonance intensity attains its maximum for 1.35 L of water, where the change of the work function is almost saturated. According to both of integrated peak area and our modeling of the work function change, we conclude that the exposure of 1.35 L of H₂O results in ~ 1 ML coverage. When the H₂O exposure is increased to attain coverage above 1 ML, the resonance peak area, i.e. the DOS of the unoccupied wet electron state decreases, and above 3 L it saturates at ~ 25% of its maximum value.

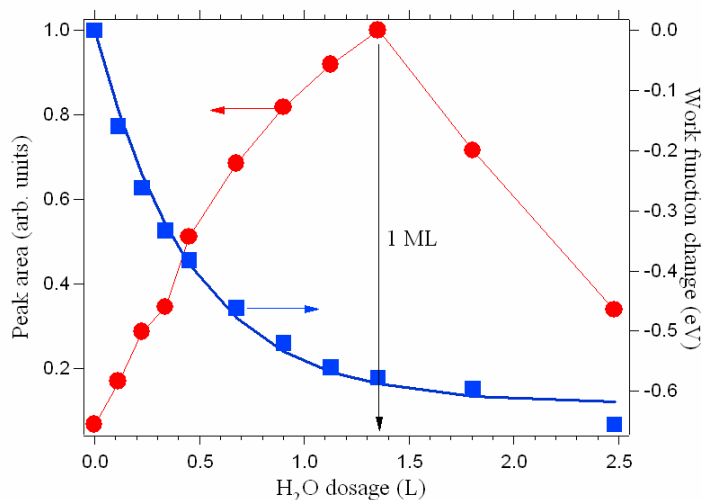


Figure 5.7 Plot of the wet electron-state peak area from difference spectra such as in Fig. 5.6 (circles), and the work-function change (squares) plotted as a function of water exposure. The solid line is a fit of the work-function change to the Helmholtz model. The resonance intensity reaches its maximum at a coverage of 1.35 L corresponding to the approximately 1-ML H₂O.

5.4 Temperature Dependence of the Water-induced Resonance

Intensity

In order to confirm that the wet-electron state attains the maximum intensity at 1 ML of H₂O, we also measured 2PP spectra for surfaces where H₂O coverage was defined by the surface temperature. Temperature programmed desorption (TPD) spectra of H₂O/TiO₂ surfaces in Fig. 5.8 from Henderson [46] exhibit peaks at 155, 175 and 270 K, respectively, which have been assigned to the desorption of water from the multilayer, the second layer and monolayer films. In

addition, for reduced surfaces hydroxyl recombination to form H₂O leads to an additional peak at 500 K (not shown) [46].

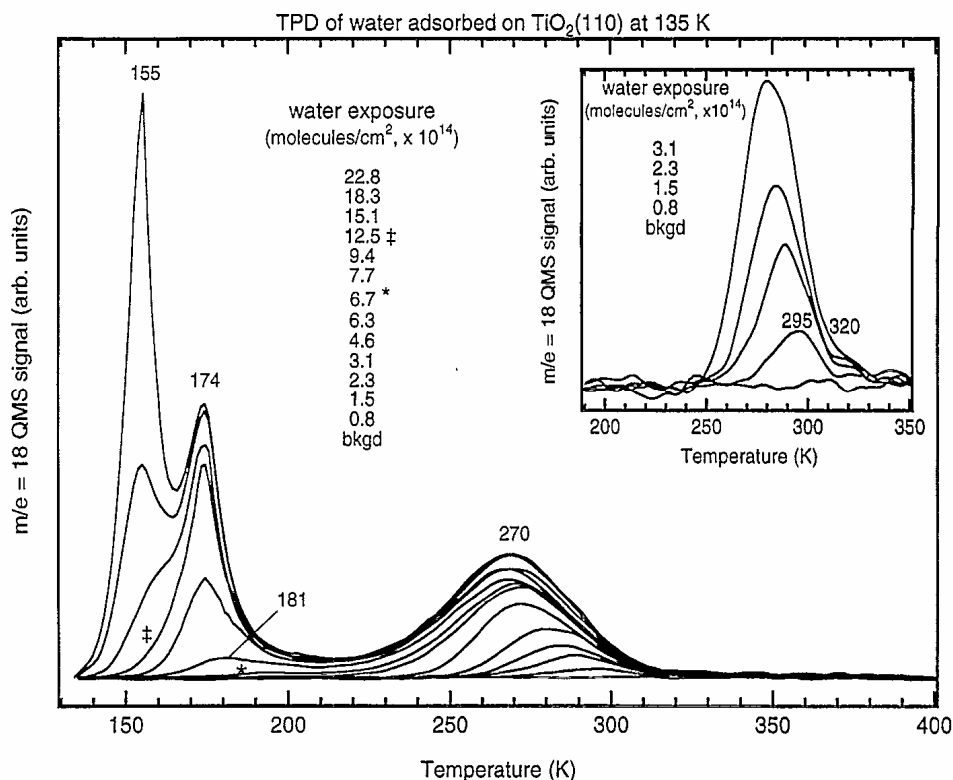


Figure 5.8 TPD spectra for different initial exposures of TiO₂ (110) surface to water at 135 K. The background spectrum corresponds to exposing the crystal to the background chamber pressure (2.0×10^{-10} Torr) for 40 min [46].

After dosing 3.7 L of H₂O onto a reduced surface, we measured 2PP spectra at several temperatures with both p- and s-polarized light. In Fig. 5.9, we plot the excess DOS arising from

the difference spectra of the “wet-electron” state for each temperature. The peak intensity is initially weak, and it increases to a maximum at 180 K after the H₂O multilayer film is desorbed above 175 K to expose the first monolayer. The wet-electron DOS decreases above 180 K and is nearly extinguished when the remaining H₂O is desorbed at 300 K. The 180 K data confirm that the resonance maximum occurs for ~ 1 ML H₂O coverage. With only OH groups remaining on the surface at 300 K, a weak feature, which appears as the low energy wing of a peak that exists above 3.05 eV, is observed. Based on the H₂O coverage dependence of the wet electron resonance and its appearance only on the reduced TiO₂ surfaces we conclude that both the minority OH and majority H₂O species are necessary to observe the “wet electron” resonance.

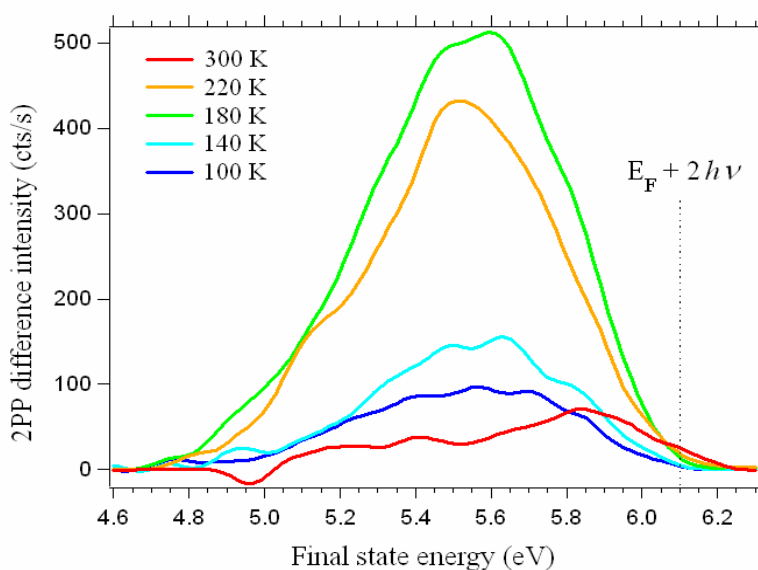


Figure 5.9 The p-s polarization difference spectra recorded at different temperatures after exposing the reduced TiO₂ surface to 3.7 L of H₂O below 100 K. According to the TPD spectra in Fig. 5.8, 1-ML coverage of H₂O is attained at 180 K, where the “wet-electron” state has maximum intensity. Only OH groups remain on the surface above 300 K.

5.5 DFT Electronic Structure of H₂O/TiO₂ Surfaces

To assign the wet-electron state to specific adsorbate-substrate structures, J. Zhao et. al. performed plane-wave pseudo-potential DFT calculations for associatively chemisorbed H₂O at Ti_{5c}^{4+} sites and H adsorbed on bridging O sites of TiO₂ for various coverages and structures [76]. Density function theory (DFT) was developed by W. Kohn and L. J. Sham to describe the electron distribution in a homogenous many-body interacting system as a function of the electron density n . Details of the DFT method are given in Appendix D [106]. The most relevant structure to our experiment is 1 ML H₂O + 0.5 ML H, where intervening bridging O atoms hinder orbital overlap between the neighboring OH species. Because, these clusters which are representative of the experimentally attained low-OH coverage surfaces, have a calculated unoccupied energy level at 2.4 eV in good agreement with the experimental measurement.

The calculated distribution of orbitals for the lowest energy adsorbate-localized unoccupied states for 1 ML H₂O + 0.5 ML H at 2.4 eV is shown in Fig. 5.10. The unoccupied states of the adsorbate-covered surfaces are either associated with the Ti^{4+} ions, which form the conduction band of TiO₂, or the dangling H atoms on OH and H₂O. For each H₂O and H coverage and structure, we found unoccupied adsorbate-localized states, where the unoccupied orbitals span clusters of several dangling H atoms, involving single OH with two or more H₂O molecules. The association of electrons with the dangling H atoms is well known from the studies of hydrated electrons in water [107] and its clusters [102-105, 108, 109]. Once again (defined previously in

Section 5.3), based on the analogy to the electrons partially hydrated in small H₂O clusters, we attribute the observed water-induced resonances to the partially hydrated or the so called “wet-electron” states that we calculated for TiO₂ surfaces.

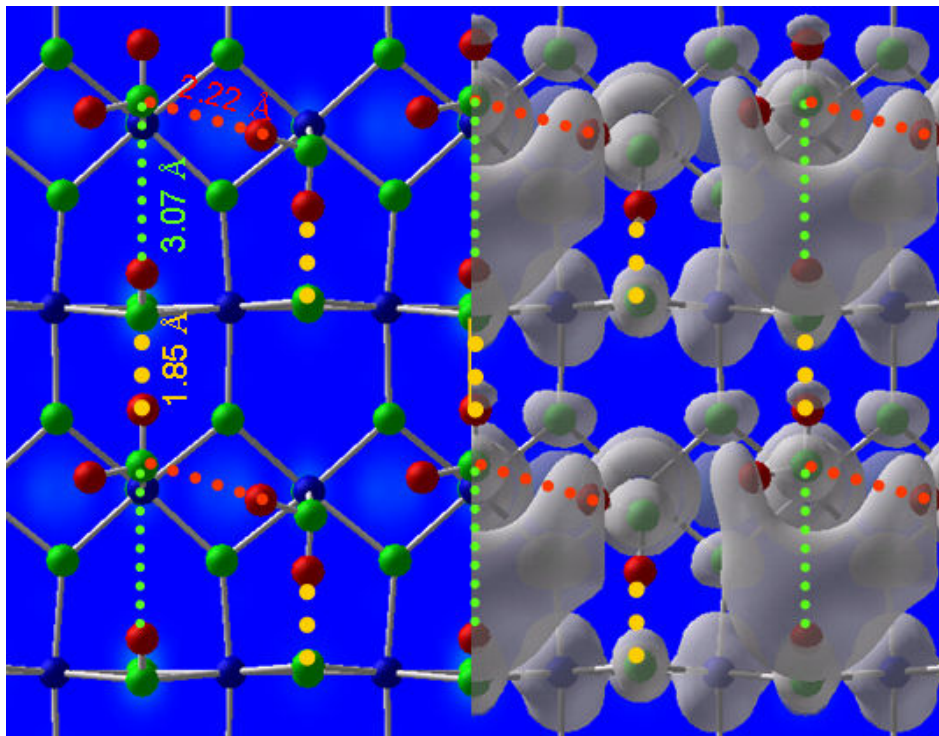


Figure 5.10 The optical molecular structure for the 1 ML H₂O + 0.5 ML H covered TiO₂ surface at 2.4 eV above the E_F (left), and the orbital distribution of the same structure with superimposed unoccupied state probability (right). The adsorbate orbitals are spread over clusters involving one OH and one H atom each contributed by two adjacent H₂O molecules. Red, Green, Blue atoms represent H, O, Ti atoms respectively, and various hydrogen bond separations are indicated [30, 89]

The DFT calculations of other structures and coverages show that the minimum wet electron energy is attained when there are adjacent OH sites on bridging O rows, i.e. for 1 ML H structures, where the unoccupied state energy could be as low as 1.5 eV. Such adjacent OH occurring on the experimental surfaces could be responsible for the characteristic low-energy tail in the difference spectrum in Fig. 5.6 [110]. Moreover, the calculated wet electron state energy of 3.5 eV for 1 ML H₂O explains why the resonance cannot be excited with 3.05 eV light for the stoichiometric surfaces. Because H₂O helps to stabilize the wet-electron state on the minority surface OH species, when H₂O desorbs above 300 K, the resonance energy increases above 3 eV, and cannot be observed by our laser. All the different wet-electron energies of the various corresponding H₂O/H adsorption structures along with the number of dangling H atoms in each hydration cluster are given in Fig. 5.11, and more detailed information on the theoretical study can be found in [76].

Above 1 ML H₂O coverage, the dangling H atoms on the OH species are partially consumed by the hydrogen bonding with the second layer water molecules thereby removing the attractive sites for stabilizing electrons in the H₂O overlayer. The removal of dangling H atoms at higher coverages has been reported in HREELS spectra of H₂O/TiO₂ surfaces [46], and was confirmed in our 2PP studies for the multilayer of H₂O adsorption causing the decrease of the resonance intensity over one monolayer coverage, presented in previous sections [30].

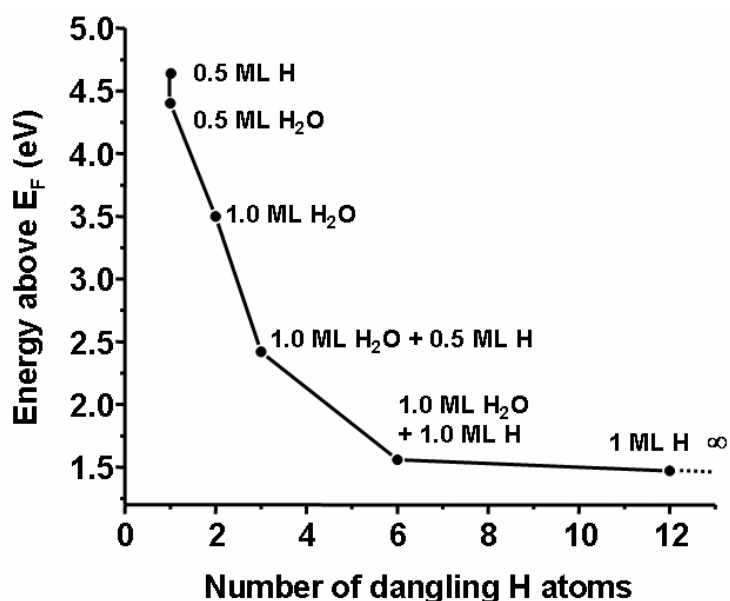


Figure 5.11 The correlation of the wet-electron energy for different coverages of H₂O and H adsorbates with the number of dangling H atoms in each hydration cluster. The infinite limit corresponds to the 1 D chain of H atoms on the bridging oxygens [76].

5.6 Atomic-H Adsorption on TiO₂ Surface and co-adsorption with H₂O

In section 5.3, we discussed the properties of the H₂O molecule induced resonance, i.e. the “wet electron state” [30, 76], which appears on the defective (i.e. reduced) TiO₂(110) surfaces. However, the absence of the molecular resonance on the H₂O covered stoichiometric surface (Fig. 5.3) tells us that this feature appears only when –OH groups are created on reduced surfaces through the dissociation H₂O at the bridging oxygen vacancy sites and in addition the molecular water is chemisorbed at the 5-coordinate Ti terminal sites. Here, we present an alternative protocol to create the wet-electron state: Exposing of the stoichiometric surface to H atoms

produced by flowing H₂ over a thermal cracking source, followed by molecular water deposition, which presents a separate route to producing surfaces with minority -OH species co-adsorbed with monolayer H₂O to confirm the proposed assignment of the wet-electron state.

Here is our experiment to generating the hydroxylated (or H-terminated) TiO₂ surface. The stoichiometric surface is prepared and cooled down to below 100 K, then exposed to hydrogen gas introduced by back-refilling method through a leak valve. H atoms are generated through thermal cracking of H₂ by a tungsten wire with a diameter of 0.38 mm, which is heated to ~2000 K. The distance between the wire and the sample is around 50 mm. This experimental condition is comparable to that used by Suzuki, et al. [111] for the same application. However, we apply much higher H₂ pressure (2×10^{-7} mbar), which results in a shorter exposure time (up to 4 min).

In Fig. 5.12, we observe in 2PP spectra that the work function of TiO₂ is continuously down-shifting upon the exposure to the H atom flux to form the bridging -OH. Before exposing the surface to H atoms, we also recorded 2PP spectra during the exposure to molecular hydrogen at high pressure as control measurement (data not shown). We observed that the 2PP spectra were barely changed, indicating the hydrogen molecules H₂ do not dissociate to an experimentally significant extent on TiO₂ surface due to a high energy barrier for molecular chemisorption. Therefore, the spectral changes in Fig. 5.12 are mainly due to the exposure to atomic H from the thermal cracking source. More over, at our experimental condition, the work function change (Fig. 5.12) due to chemisorption of H flux does not stop or saturate yet, indicating the H

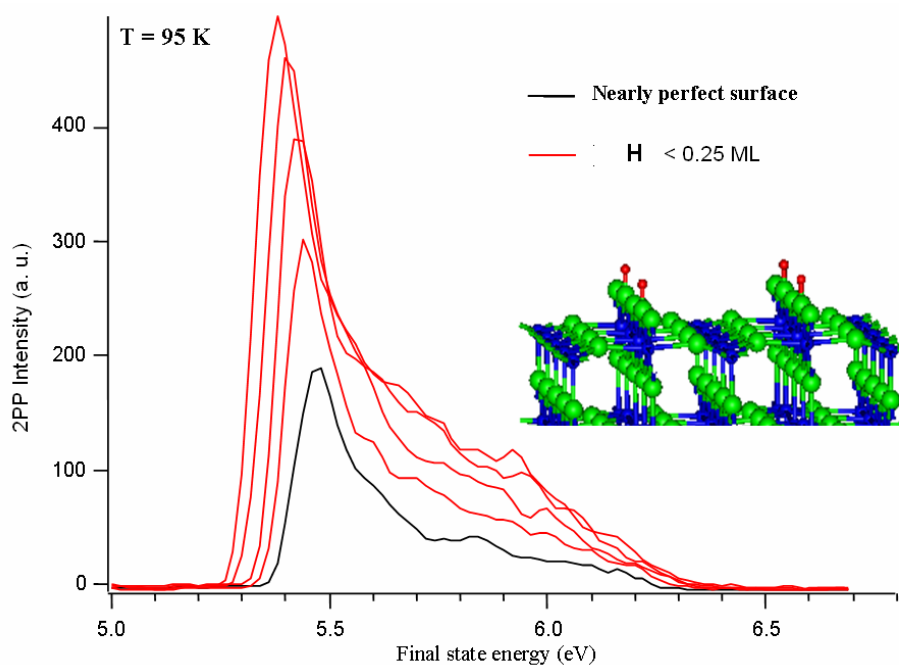


Figure 5.12 2PP spectra for progressive exposures to atomic H onto a stoichiometric TiO_2 . The estimated H-atom coverage is < 0.25 ML.

coverage is relatively smaller compared to the highest H coverage (0.23 ML) reached by Suzuki et al [111]. As we know, the saturation of the work function change for O_2 or H_2O adsorption corresponds either to the complete titration of oxygen vacancies on the surface or the establishment of the monolayer structures, therefore our H dosage is actually corresponding to a minority of -OH terminals on the TiO_2 surface.

STM of Atomic-H / TiO₂ (110)

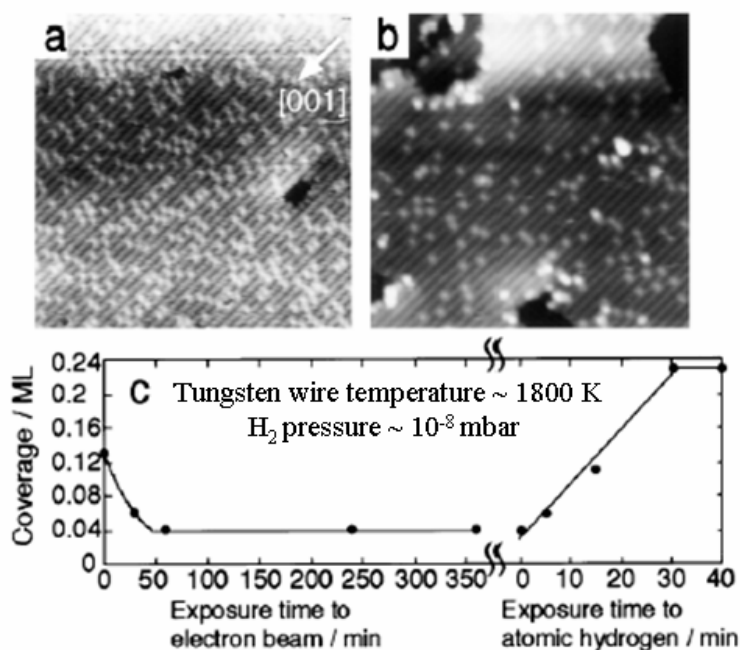


Figure 5.13 The STM image for H-terminated surface, where the 20 eV electron irradiation decreases the concentration of -OH population and exposure of the H-flux up to a half hour reaches the saturation at 0.23 ML [111].

Suzuki et al determined the H-coverage according to their STM in Fig. 5.13, where the Ar⁺ sputtered-annealed surface is essentially covered by submonolayer of -OH, either from cracking of H₂ molecules by Ar⁺ ions, or the dissociation of H₂O at defects. By using a low energy electron irradiation (~ 20 eV), the H atom features are greatly decreased, without damaging the surface. As shown on the left side of Fig. 5.13 (c), the H atom density is decreased from 0.13 to 0.04 ML during the first 60-min of electron irradiation. Further exposure does not change the H

atom coverage. After the electron treatment, exposing the surface to the H atom source increases the H atom concentration to a saturated coverage at ~ 0.23 ML as deduced from the STM images (Fig. 5.13). Among those surface species, the majority are bridging -OH, which can be removed by 20-eV electron irradiation; the minor species (0.04 ML) that remained on the surface after electron irradiation can be assigned to H adatoms trapped at oxygen vacancies.

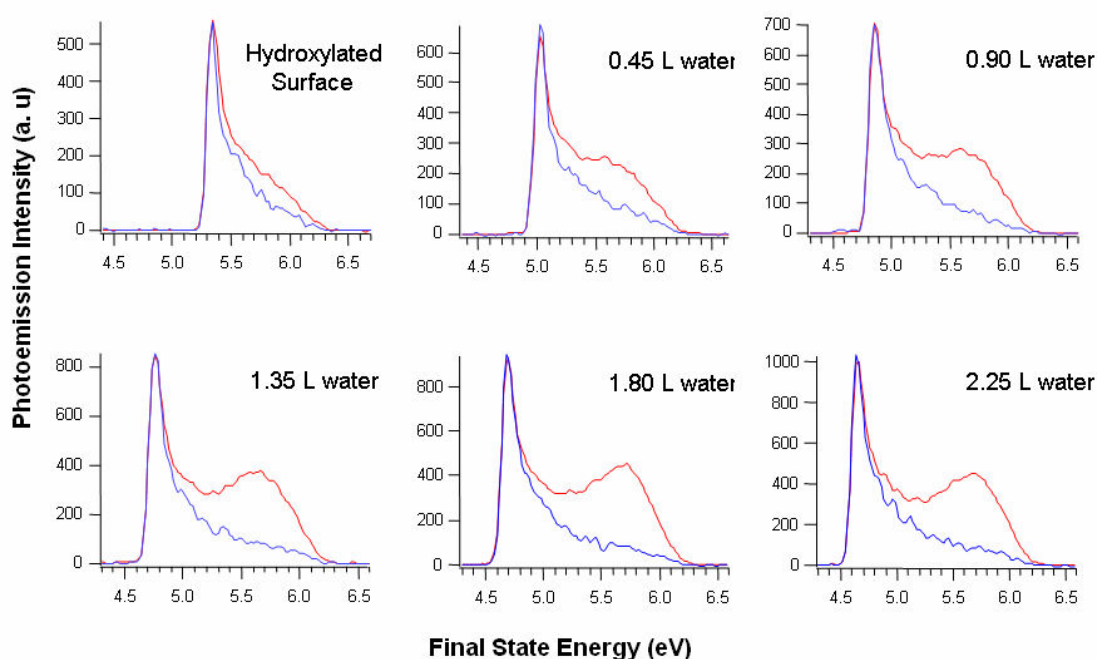


Figure 5.14 The comparison of 2PP spectra excited with s- (blue) and p-polarized (red) light for different exposures of the hydroxylated $\text{TiO}_2(110)$ surface to H_2O molecules.

In Fig. 5.14, we show the effect of exposure of the minority H terminated (generated from Fig. 5.12) stoichiometric surface to different dosages of H_2O molecules from 0 up to 2.25 Langmuir at 90 K. Before the introduction of H_2O , there is a small difference between the normalized p-

and s-polarized 2PP spectra. The small difference is probably caused by the H₂O formed in the UHV chamber by the interaction of H atoms with the chamber surfaces. With additional exposure to water molecules, the difference becomes larger and saturates above 1.8 L. The additional DOS introduced by H₂O adsorption is very similar in energy and its dependence on the H₂O exposure to the wet electron states produced through exposure of reduced TiO₂ surfaces to H₂O. Therefore, this alternative protocol can also create wet-electron states, and it confirms our assignment of the wet-electron DOS to the electron solvation by the minority of -OH and majority of H₂O species on the surface. However, the central energy for the wet electron states generated by this protocol is somewhat (0.2 eV) higher than that achieved through the dissociation of H₂O on reduced TiO₂ surfaces [30]. This difference may be related to differences in the -OH coverage achieved by the two protocols, which apparently affects the character of the wet electron states.

5.7 Charge Transfer Dynamics at the H₂O/TiO₂ Interface

In order to measure the lifetimes of the wet-electron states, we performed time-resolved measurements at various energies for the TiO₂ surface after different exposures to H₂O. Fig. 5.15 (a) indicates the measurement energies at the wet electron resonance induced by ~ 1 ML H₂O for the time-resolved interferometric two-photon correlation I2PC scans [2] which are shown in Fig. 5.15 (b). We compare the I2PC scans averaged over the optical phase at different energies, and find out that they were only weakly dependent on the measurement energy. So this feature

demonstrates that the photoexcited wet-electrons in the interfacial molecular structures decay uniformly back to the TiO₂ substrate surface.

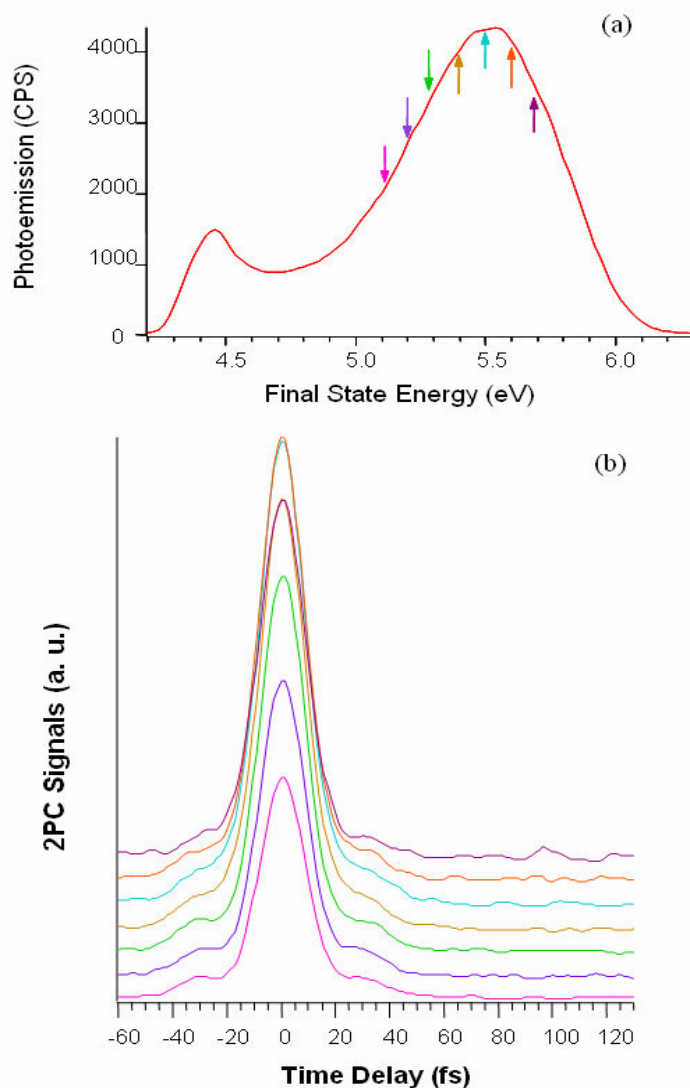


Figure 5.15 (a) 2PP spectrum for ~ 1 ML H₂O covered TiO₂(110) surface with the energies for time-resolved measurements indicated by color coded arrows. (b) The corresponding I2PC scan envelopes in the order of decreasing energy from top to bottom.

In order to calculate the ultrafast time scales for the decay of the wet electron states, in Fig. 5.16 we plot the averaged I2PC scans and their fits to an optical Bloch model [27] assuming single exponential decay kinetics for the bare TiO₂ surface, and reduced TiO₂ surfaces with 0.5 and 1.1 ML H₂O coverages. All surfaces displayed only weak dependence on the measurement energy; however, the adsorption of H₂O noticeably increased the I2PC width and therefore implies a finite intermediate-state lifetime. The I2PC scan for the bare surface is identical to the pulse autocorrelation, given by the two-pulse correlation from the Molybdenum sample, indicating that the 2PP process most likely occurs via virtual intermediate states. The wet-electron lifetimes increase to 10 ± 1 and 14 ± 1 fs for exposures of 0.5 and 1.1 ML of H₂O, respectively, and saturate at ~ 15 fs for >1 ML coverage. Because their energy relaxation by electron inelastic scattering in H₂O overlayer is unlikely to be so fast, wet electrons probably decay by resonant charge transfer into the conduction band of TiO₂. And the inserted diagram in Fig. 5.16 gives more details regarding to the two-photon photoemission (2PP) process occurring at the H₂O/TiO₂ interfaces. The electron distributions are excited exclusively (using Franck-Condon approximation [19], which assumes that the nuclei in the system are frozen during the electronic transition) from the bandgap $Ti_{5c}^{+4-\delta}$ DOS (Section 4.2) to the H₂O-OH chemisorption induced wet-electron state, followed by a decay process within 15 fs through the resonant charge transfer into the conduction band of TiO₂ substrate. The measured lifetime corresponds to only two periods of O-H stretching vibration, therefore the nuclear motion of H₂O molecules to more favorable electron hydration structures cannot compete with the resonant charge transfer.

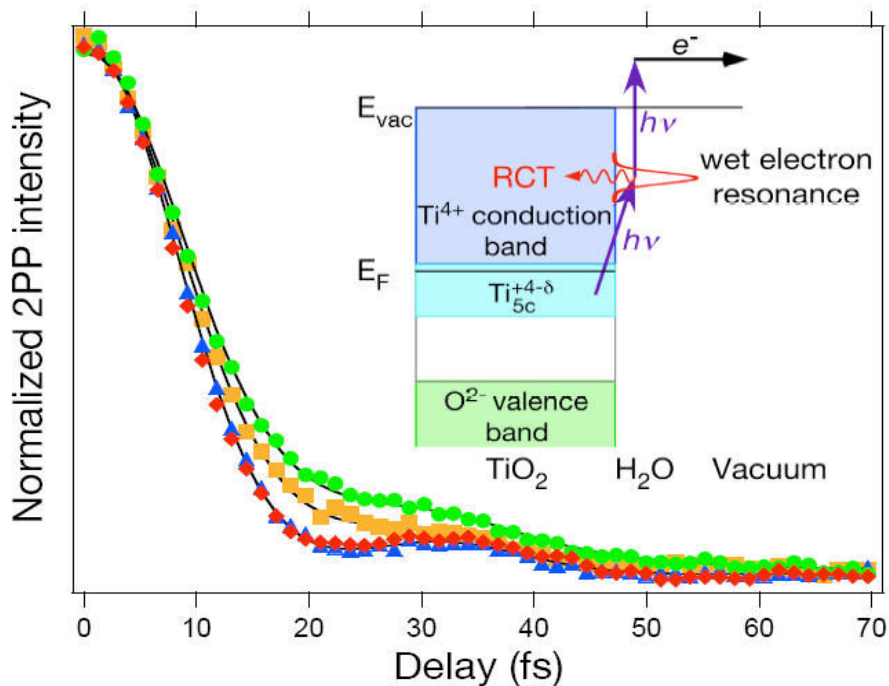


Figure 5.16 Phase-averaged I2PC scans for the bare reduced TiO_2 surface (red), and after its exposure to 0.5 (orange) and 1.1 ML (green) of H_2O . The black lines represent fits with a three-level optical Bloch equation model assuming single exponential decay kinetics for the intermediate state and using the experimentally measured pulse autocorrelation (blue). The bare surface intermediate-state lifetime is too short to determine, and the lifetimes for 0.5 and 1.1 ML H_2O covered surfaces are 10 ± 1 and 14 ± 1 fs, respectively. The insert illustrates the relevant two-photon process associated with the reverse charge transfer (RCT) occurring at the intermediate state.

Chapter 6

Electron Solvation in Methanol Overlayers on TiO₂ Surfaces

In order to probe the fundamental photocatalytic processes of TiO₂ in water, in the previous chapters we described the 2PP spectroscopy studies of H₂O/TiO₂(110) surfaces. 2PP spectra provide information on both the occupied and unoccupied electronic states near the Fermi level, such as the formation of $Ti^{+4-\delta}$ defect states near the conduction band minimum, and the changes of the work function through the reduction of the sample by various means. Remarkably, for reduced H₂O/TiO₂(110) surfaces we also observed a pronounced peak in 2PP spectra due to adsorbate-induced intermediate state at 2.45 eV above E_F [30]. Because this peak can only be observed when TiO₂ surface is hydroxylated, and reaches the maximum intensity at 1 ML coverage of water, we assigned it to the charge transfer from the reduced five-coordinate $Ti_{5c}^{+4-\delta}$ ions to the excited hydrated electron states centered on the neighboring -OH groups and stabilized by coadsorbed H₂O molecules.

In order to further elucidate the nature of molecule induced resonances and to understand how organic molecules interact with the TiO₂ surfaces, we use 2PP spectroscopy to study the system of CH₃OH/TiO₂(110). Methanol is the simplest protic organic adsorbate with well-known liquid and interfacial electron solvation, adsorption and photochemical properties. In the photocatalytic splitting of water, a small amount of methanol significantly accelerates reaction rate by sacrificial decomposition [1, 11, 12, 79]. Infrared time-resolved spectroscopy revealed that lifetimes of photogenerated electrons on TiO₂ surfaces are extremely long in the presence of methanol, because it acts as an efficient trap for the photogenerated holes [112].

6.1 Methanol Adsorption Structure

Firstly, we consider the adsorption structure of methanol on TiO₂(110) surface. Figure 6.1 illustrates our proposed model for the possible adsorption modes of methanol based on the conclusions of previous experimental measurements [113] and theoretical calculations [114]. Methanol can chemisorb at the bridging oxygen vacancy sites, where it titrates the vacancies and dissociates into methoxy (CH₃O⁻) and hydroxy (-OH) groups. After the defects are titrated, the methanol molecules bind at the terminal Ti^{4+} sites. According to both experiment [113] and theory [114], it partially dissociates (deprotonates) leaving CH₃O⁻ at the $Ti_{5c}^{4-\delta}$ sites and transferring a proton to form -OH at the bridging sites. This additional dissociation process results in a higher -OH coverage than that can be achieved for H₂O covered surfaces. Henderson's temperature programmed desorption (TPD) results along with Electron Energy Loss

Spectroscopy show that both the molecular and dissociated species co-exist on CH_3OH covered TiO_2 surfaces [113]. However, the molecular methanol can adsorb at the 5-fold terminal sites, whereas the methoxy can adsorb either in the terminal or bridging sites. Bates et al. [114] performed the first-principles calculations of the structure of 1 ML $\text{CH}_3\text{OH}/\text{TiO}_2$, and they found that among the various absorption structures, the mixed structure, including 0.5 ML molecular CH_3OH and 0.5 ML dissociated species (CH_3O^- and $-\text{OH}$) is the most stable structure.

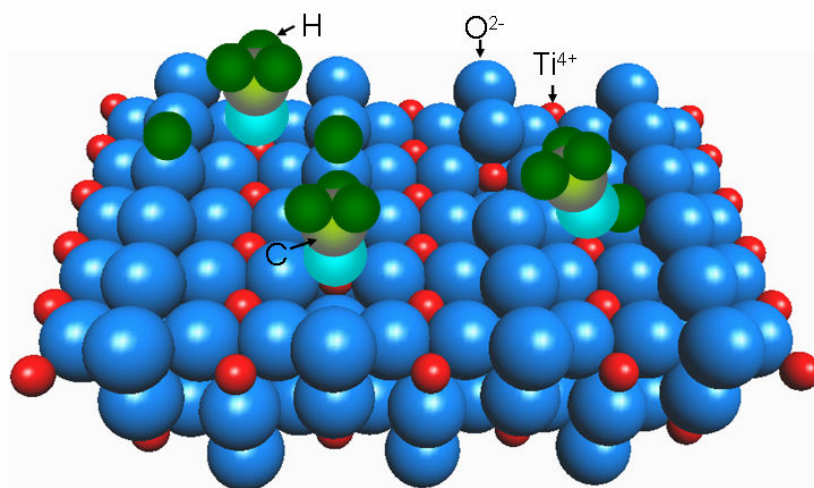


Figure 6.1 Possible adsorption sites and structures of CH_3OH on $\text{TiO}_2(110)$ surface.

In order to understand the unoccupied electronic structure of chemisorbed methanol, J. Zhao performed the DFT calculation for 1ML $\text{CH}_3\text{OH}/\text{TiO}_2(110)$ using the VASP code [115, 116]. In Fig. 6.2, we show several typical calculated molecular structures, where the overall adsorption energies for the molecular and the fully-dissociated structures (upper) are -0.68 and -0.58 eV per

unit cell respectively. However, the energies for the two possible half-dissociated structures in Fig. 6.2 (below) of -0.86 or -0.81 eV are even larger [117]. Based on previous experiments and our calculations we conclude at 1 ML coverage CH_3OH molecules partially dissociate into the mixed structures of CH_3OH , CH_3O^- and $-\text{OH}$, to minimize the overall adsorption energy for the whole system. According to Bates and Gillan, the barrier for the proton transfer from the molecularly chemisorbed to the deprotonated form is negligible (less than 0.05 eV) [114].

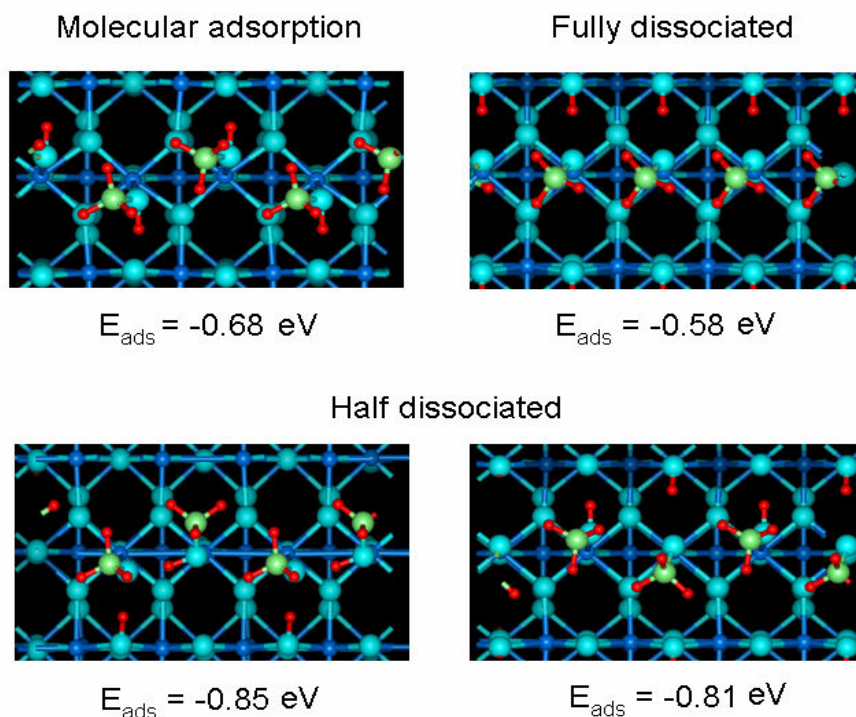


Figure 6.2 Several calculated structures for the chemisorption of CH_3OH on $\text{TiO}_2(110)$ surface and the respective adsorption energies [117].

6.2 CH₃OH Adsorption Induced Wet-Electron States

We investigate the unoccupied electronic structure of CH₃OH on TiO₂(110) surfaces in order to provide more information on the wet electron state that was observed for H₂O/TiO₂(110) surfaces.

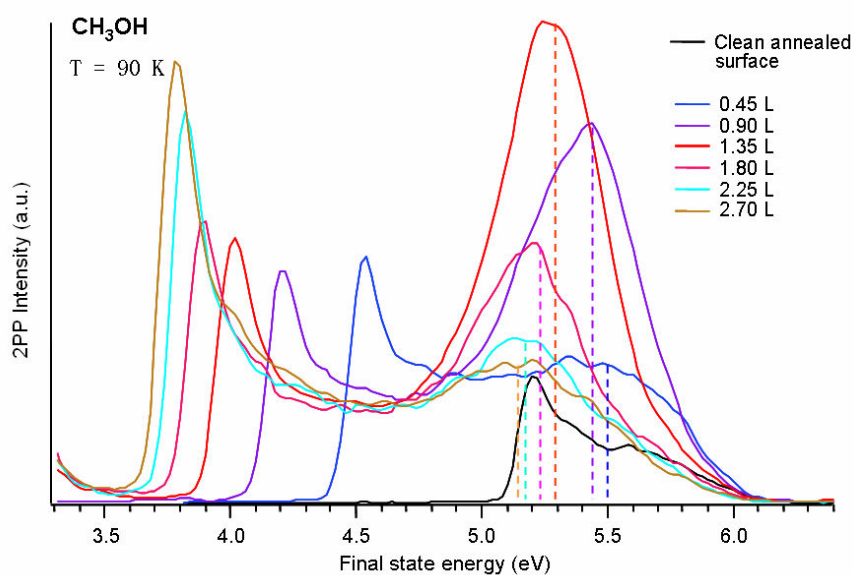


Figure 6.3 2PP spectra for a series of exposures of CH₃OH on TiO₂ surfaces.

In Fig. 6.3, we plot a series of 2PP spectra for various exposures of CH₃OH on a reduced TiO₂(110) surface. The 2PP spectra indicate substantial decrease in the surface work function as the CH₃OH coverage increases. The rate of decrease is initially fast, and eventually approaches

saturation. Similar to H₂O, the change of work function can be fitted by the Helmholtz model [29], where the effective dipole momentum of CH₃OH is calculated to be 0.72 D, which is significantly larger than for H₂O (0.5 D). Another distinct feature in Fig. 6.3 is the broad CH₃OH coverage dependent resonance with final state energies in the range of 5.0 ~ 5.8 eV. Similar to H₂O, the resonance peak area increases with CH₃OH coverage upon initial exposure, however, above certain exposure, the trend reverses and the peak area starts to decrease to a saturation value of 20~30% of its maximum value. However, by contrast to H₂O the resonance peak energy decreases monotonously with the CH₃OH dosage.

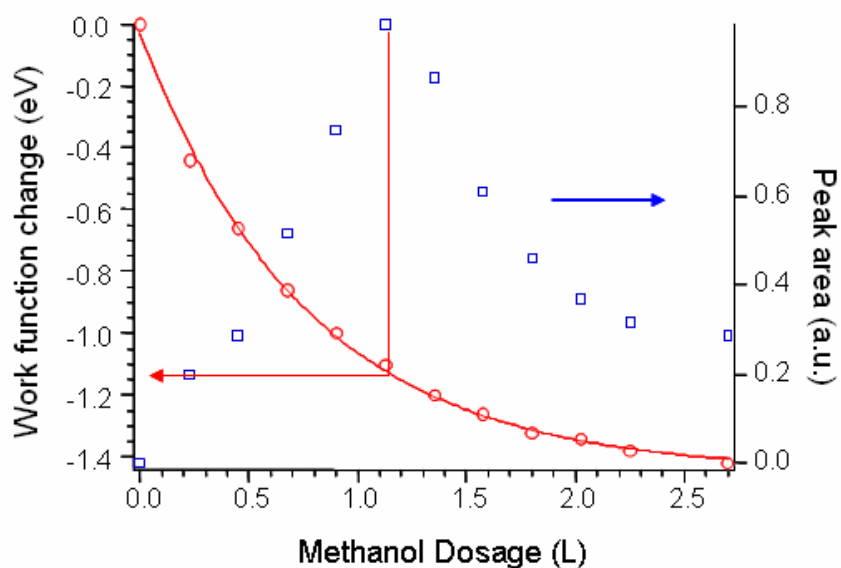


Figure 6.4 Work function change fitted by Helmholtz model and the resonance peak area for increasing exposure of TiO₂(110) surface to CH₃OH. The arrows indicate the appropriate axis for different data.

In Fig. 6.4, we plot the normalized integrated resonance peak areas for different exposure of CH_3OH , and similar to H_2O assign one-monolayer coverage (1 ML) to the point where the peak area achieves the maximum. At this point the work function change of about -1.2 eV approaches saturation. The work function shift of -1.2 eV is almost twice as large as that of H_2O , indicating that CH_3OH molecules induce larger charge transfer to the surface and possess a larger dipole moment than H_2O molecules.

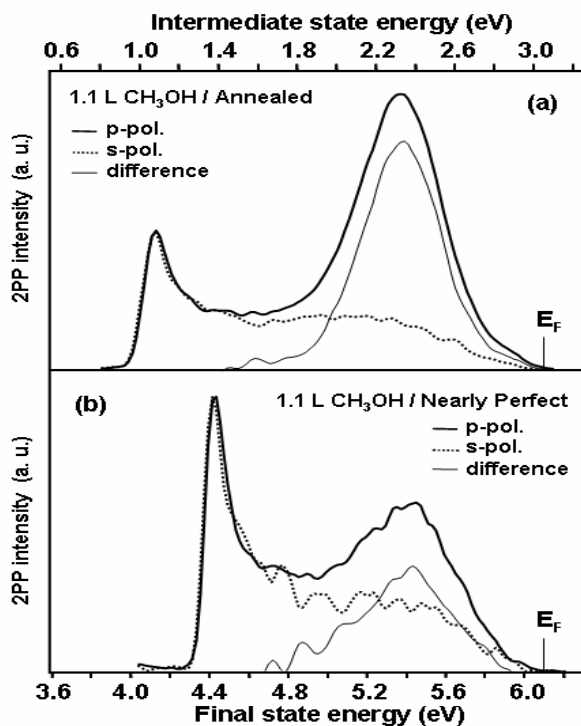


Figure 6.5 The normalized 2PP spectra of (a) reduced and (b) stoichiometric $\text{TiO}_2(110)$ surfaces exposed to 1.1 L methanol measured with p- (thick lines) and s-polarization (dashed lines) at 100 K. The difference spectra (thin lines) show the methanol-induced resonance [118].

Fig. 6.5 shows 2PP spectra of the (a) reduced and (b) stoichiometric TiO₂ surfaces at approximately 1 ML coverage measured with p- and s-polarization. The spectra are normalized at the work function edge, and their difference is shown with thin solid lines. Like for H₂O/TiO₂, this procedure isolates the methanol-induced resonance. However, unlike water, the peak is observed for both the stoichiometric and annealed surfaces. We note, however, the peak is considerably stronger for the annealed surface.

The polarization dependence of the 2PP spectra in Fig. 6.5 indicates that the transition dipole moment is directed normal to the surface. The methanol induced resonance does not appear in spectra measured with a single 6.1 eV pulse-excitation, so it must represent an unoccupied intermediate state, which mediates the 2PP process for resonant excitation from the $Ti_{5c}^{+4-\delta}$ defect states. Consequently, the resonance peak implies the adsorption of methanol introduces a new state at ~ 2.3 eV above the Fermi level for both the stoichiometric and reduced surfaces. The energy, coverage dependence, and polarization dependence of the methanol induced resonance peak is similar to that observed for H₂O adsorbed reduced TiO₂ surfaces (Section 5.7). Based on this comparison, we assign it to the charge transfer (CT) excitation from neighboring terminal $Ti_{5c}^{+4-\delta}$ ions to the methanol overlayer [119-121]. The main difference between methanol and water is that for the former the resonance peak appears on both the reduced and stoichiometric surfaces, while for the latter, it only appears on reduced surfaces. This difference can be attributed to lack of dissociation of water on stoichiometric surfaces, while methanol partially

dissociates on both surfaces. The different propensity of H₂O and CH₃OH towards the dissociation on TiO₂ is in agreement with the previous IR and TPD measurements of Henderson et al [113]. In order to further characterize the methanol induced resonance, we investigate its dispersion along the [001] (parallel to the bridging oxygen rows) and $[\bar{1}10]$ (perpendicular) for ~ 1 ML coverage (data not shown). We found that the methanol induced resonance is non-dispersive, indicating that the excitation is localized [118].

6.3 Electron Dynamics at the CH₃OH/TiO₂ Interface: Energy and Coverage Dependence

We perform time-resolved measurements on ~1.2 ML CH₃OH covered TiO₂ surface in order to characterize the time scale of the electron decay from the photoexcited CH₃OH/TiO₂ overlayer [2, 75] (Fig. 6.6 (a)). We record interferometric two-pulse correlation signals (I2PC) for a range of energies near the methanol resonance (Fig. 6.6 (b)). The representative phase averaged I2PC scans strongly depend on the observation energy: at energy levels above the peak maximum the signals follow the single exponential decay kinetics. However, at the lower energy levels, especially below the resonance energy, the dynamics obviously deviate from the single exponential decay kinetics, including at least two independent decay time scales. The electron kinetics are substantially different from the observed “wet-electron” dynamics in the H₂O/TiO₂ system.

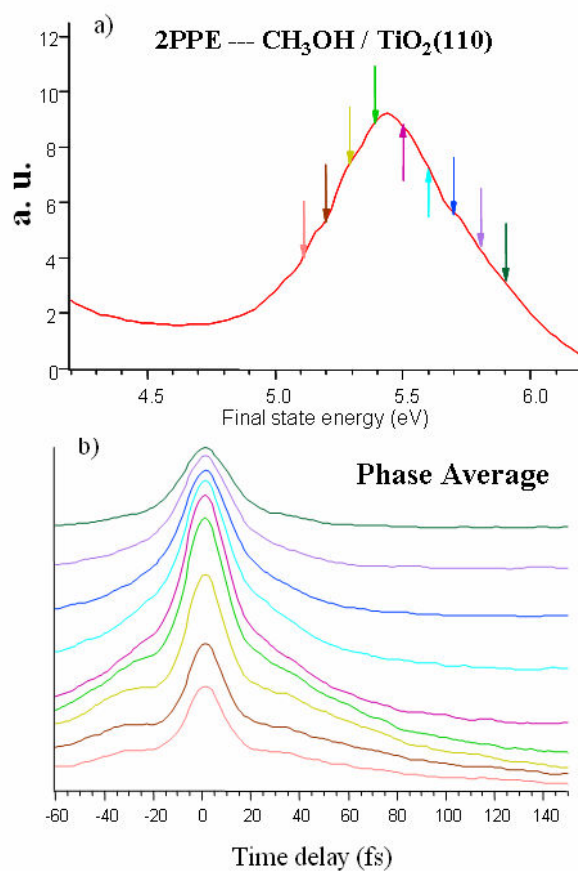


Figure 6.6 (a) 2PP spectrum for ~ 1.2 ML covered CH_3OH surface. Colored arrows indicate the energies for which time-resolved measurements in (b). (b) The Phase-averaged interferometric two-photon correlation signals for energy levels indicated in (a).

Time-resolved measurements for different CH_3OH coverages (from ~ 0.3 ML up to ~ 2.0 ML) indicate that the excited state dynamics strongly depends on the CH_3OH coverage. In Fig. 6.7 we compare phase averaged I2PC signals at the resonance energy for each of the measured CH_3OH coverages. Compared with the pulse autocorrelation signal, the normalized I2PC signals

have similar central shapes indicating the coherence decay time < 1 fs. The much broader and coverage dependent wings indicate much longer and more complex population dynamics. By contrast to the wet-electron feature in $\text{H}_2\text{O}/\text{TiO}_2$ system, the typical I2PC at resonance energy for different CH_3OH coverages are very different: The decay time of the I2PC increases significantly as the CH_3OH coverage increases; at the higher CH_3OH coverage, the substructure in the autocorrelation trace due to the nonlinear dispersion is washed out due to the longer electron decay time. However, at and above 1 ML coverage a distinct new sub-peak feature appears, exhibiting coverage-dependent non-exponential decay kinetics.

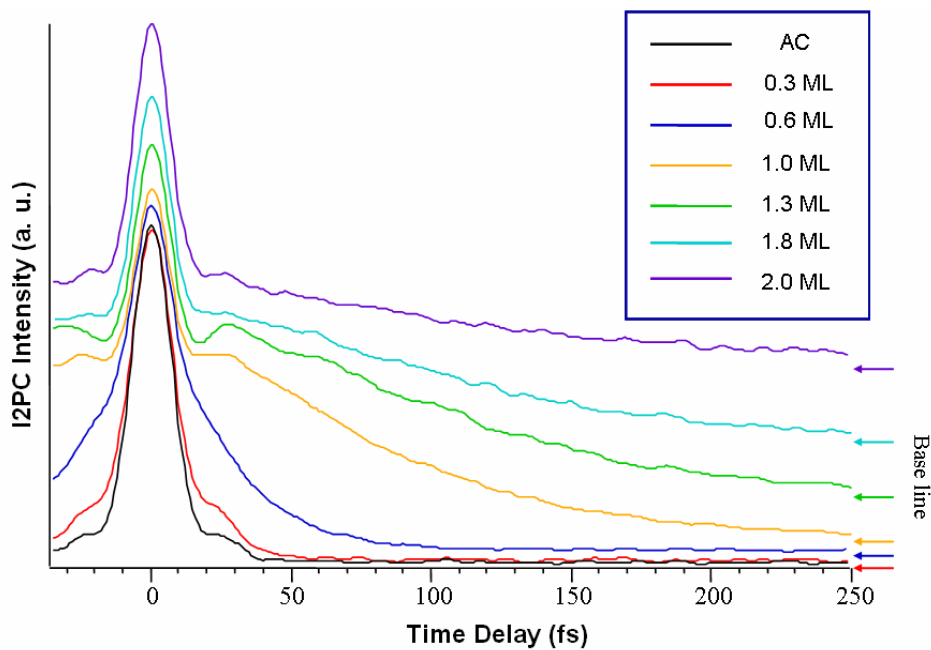


Figure 6.7 The typical normalized I2PC scans for different coverages of CH_3OH adsorbed TiO_2 surfaces (from 0.3 ML up to 2.0 ML). The arrows at the low-right corner indicate that the appropriate offsets are used. The pulse autocorrelation (AC) trace is given in black.

In order to investigate quantitatively and develop a model of the wet-electron dynamics on CH₃OH/TiO₂ surfaces, we perform systematically time-resolved measurements for a spectrum of energies across the methanol resonance induced by various coverages and present the results in three dimensional (3D) contour plots in Fig. 6.8. These plots are constructed from 2PC measurements recorded in 0.1 eV intervals, which are combined to provide a map of 2PP emission intensities at different energies and pump-probe delays. These 3D plots in Fig. 6.8 obtained for various CH₃OH coverages show that the CH₃OH induced wet-electron state density is spread over a broad energy range of 0.5 ~ 0.7 eV, and that the decay time scales increase with the CH₃OH coverage, from roughly 35 fs at ~0.3 ML to above 200 fs at ~2.0 ML. The 3D plots in Fig. 6.8 are composed of 2PC scans spanning around 20 different energies. The 2PP intensity scale is given by the bar code in the figure. The 3D plot clearly show that the lifetimes are long (relative to e.g. clean surface) and coverage dependence, while below the resonance, where the 2PP processes mediated by virtual intermediate states, the 2PC trace widths are laser pulse width limited. We will employ such 3D plots to present and analyze the electron dynamics in the methanol overlayer structures on the TiO₂ surfaces in the following sections.

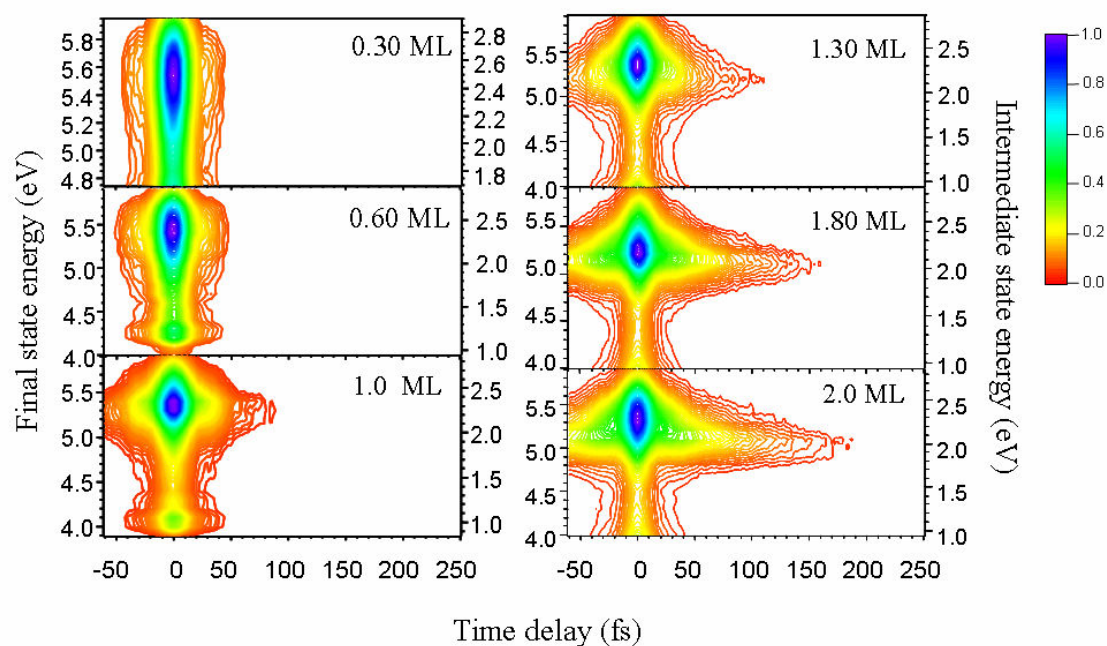


Figure 6.8 The 3D contour plots of the 2PP intensity profiles for the different amounts of CH_3OH adsorbed TiO_2 surfaces as a function of pump-probe delay. The left axis indicates the final state energy, and the right axis the intermediate state energy. The 3D plots are constructed from two-pulse correlation measurements (2PC) taken at 0.1 eV intervals. The bar graph on the right represents the normalized intensity scale where the peak intensity at each coverage is set to 1.0.

6.4 The Kinetic Scheme for Simulating the CH_3OH Dynamics

Besides the remarkable energy (Fig. 6.6 (b)) and coverage dependence (Fig. 6.7) revealed in measurement of the wet-electron dynamics on the CH_3OH deposited TiO_2 surfaces, we also find

that in a certain coverage and energy range the 2PC signals do not obey the single exponential decay kinetics. This is especially true at the energy levels below the resonance energy for CH₃OH coverages of >1 ML. More detailed investigations and analysis of the CH₃OH/TiO₂ system in the next Section (Section 6.5) indicate the CH₃OH related electron dynamics include both population and energy relaxation processes, as well as a pronounced deuterium isotope effect. Obviously, this complex kinetics cannot be explained by the standard 3-level scheme involving single adsorbate localized intermediate state [27]. In order to simulate the experimental data and retrieve the time decay constants for the various relevant kinetic processes, we modified the standard Optical Bloch Equation (OBE) model by proposing two close lying intermediate states (Fig. 6.9 (a)). In the proposed model, the ground states 0 are the occupied bandgap states below the Fermi level, the final states 2 are the free electron states above the vacuum level as before. The intermediate states 1 and 1* represent the intermediate molecular resonance excited states that are responsible for the observed dynamics [31].

Now, let us consider the population decay of the intermediate energy states following the photo-excitation process. Initially, the photoexcitation transfers electrons from the band gap DOS and populates mainly the higher intermediate state 1, however the simulation shows the lower energy state 1* could also be mildly populated (< 30%). After excitation, the population of the higher energy level N_1 partially transfers into the lower energy level N_{1^*} through an energy relaxation process with a time scale $T_1^{11^*}$. In parallel with the energy relaxation from $1 \rightarrow 1^*$, the population relaxation occurs from both states by the reverse charge transfer (RCT) [3] to the CB of the TiO₂

substrate, similar to the $\text{H}_2\text{O}/\text{TiO}_2$ system. The excess electron population decay times in both of these excited states through the aforementioned RCT process are denoted as T_1^1 and T_1^{1*} respectively. In Fig. 6.9 (a), the coherence decay time scales (e.g. T_2^{01}) are indicated as well.

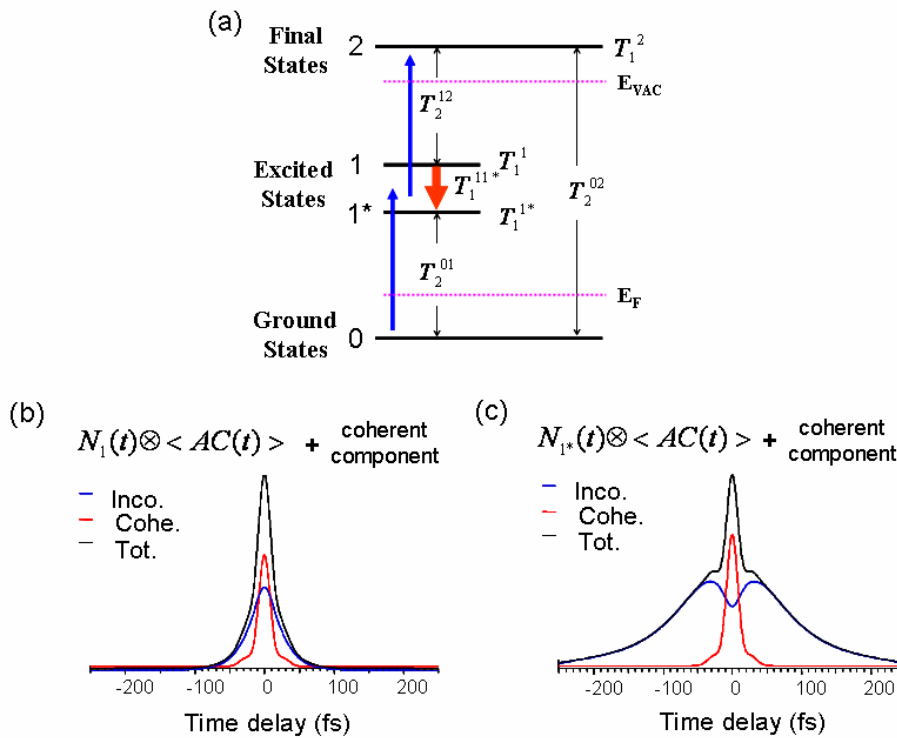


Figure 6.9 (a) The modified OBE model [27] used to simulate the non-exponential decay kinetics, where the ground state $\underline{0}$ is below E_F , the final state $\underline{2}$ is above E_{VAC} , and the intermediate states include two separate energy levels $\underline{1}$ and $\underline{1^*}$. (b) Decomposition of the coherent/incoherent components of the electron dynamics at the higher intermediate energy level $N_1(t)$, and (c) at the lower energy level $N_{1^*}(t)$. The fitting parameters are given in the text.

According to the model in Fig. 6.9, a set of differential equations (Eqs. 6.1) can be used to describe the photoexcited electron population and energy relaxation dynamics at the intermediate states 1 and 1*, where we simplify the notation for the decay parameters in Fig. 6.9 (c) by the notation:

$$T_1^1 \rightarrow \tau_1', T_1^{1*} \rightarrow \tau_{1*}, T_1^{11*} \rightarrow \tau_{11*}.$$

The differential equations describing the evolution of 1 and 1* are given by:

$$\frac{dN_1(t)}{dt} = -\frac{1}{\tau_1'} N_1(t) - \frac{1}{\tau_{11*}} N_1(t) \quad (6.1)$$

$$\frac{dN_{1*}(t)}{dt} = -\frac{1}{\tau_{1*}} N_{1*}(t) + \alpha \frac{1}{\tau_{11*}} N_1(t) \quad (6.2)$$

Where the free parameter α is used in the second equation to model a continuum of the intermediate excited states with a two-state model. The population decay rate at the higher energy level N_1 includes the contribution from both the population relaxation from the molecular overlayer through RCT (τ_1') and the energy relaxation to 1* (τ_{11*}) [30, 31]. However, since both processes lead to the decay of state 1, the combined effect can still be simulated by single exponential decay kinetics $\frac{1}{\tau_1} = \frac{1}{\tau_1'} + \frac{1}{\tau_{11*}}$. The total decay time of the primary photoexcited state 1 corresponds to the rise time of the 1* state. The population kinetics of the 1* state include the energy relaxation from the higher lying 1 state, as well as the exponential decay through both RCT and a significantly slower energy relaxation process probably related to with

the electron solvation. Since the 1* state decay kinetics again include both energy and population decay, we can combine these two rates into a single process. Thus, the intermediate state populations 1 and 1* evolve according to:

$$N_1(t) = N_1^0 e^{-\left(\frac{1}{\tau_1} + \frac{1}{\tau_{1*}}\right)t} = N_1^0 e^{-\frac{1}{\tau_1}t} \quad (6.3)$$

$$\text{and } N_{1*}(t) = N_{1*}^0 e^{-\frac{1}{\tau_{1*}}t} + \alpha \frac{N_1^0}{\tau_{1*}} \frac{\tau_1 \tau_{1*}}{\tau_1 - \tau_{1*}} \left(e^{-\frac{1}{\tau_1}t} - e^{-\frac{1}{\tau_{1*}}t} \right) \quad (6.4)$$

where N_1^0 and N_{1*}^0 are the initial amplitudes, and τ_1 and τ_{1*} are electron energy and population decay time scales for N_1 and N_{1*} respectively. For N_{1*} , the extent of the rising amplitude and the time that the population reaches its peak are determined by both the parameter α and the energy relaxation time scale τ_{1*} . We will employ this model to analyze the methanol dynamics and discuss the physical meaning of the various time scales in Equation (6.3) and (6.4) in next section.

In order to simulate the experimental 2PC scans, the coherent component (mainly involving the decoherence time scale between ground state and intermediate state i.e. T_2^{01}) of the 2PP process is added to the incoherent components described by Eqs. 6.3 or 6.4, and the sums are convoluted with the pulse autocorrelation:

$$I2PC_{pa}^{Sim}(\Delta t) = c_0 + c_1 \begin{cases} N_1(t) \\ N_{1^*}(t) \end{cases} \otimes \langle AC(\Delta t) \rangle + c_2 \exp\left(-\frac{t}{T_2^{01}}\right) \otimes \langle AC(\Delta t) \rangle \quad (6.5)$$

The parameters c_1 and c_2 are variable coefficients used to obtain the correct amplitudes of the coherent and incoherent components of the 2PC signals for the N_1 or N_{1^*} dynamic, and c_0 gives the baseline. The ratio of the coherent and the incoherent contribution is determined by the photo-excitation and electron decay kinetic in each specific system [122].

6.5 Charge Transfer Dynamics, Isotopic Effect, Solvation and Proton-Coupled Electron Transfer Mechanism

In previous sections, we introduced the CH_3OH coverage dependent dynamics by comparing the 2PP signal intensities at different methanol coverages or various representative photoelectron energies (Fig. 6.8). In order to understand the electron dynamics in the CH_3OH overlayer more precisely, we perform 2PC measurements for three comparable coverages of CH_3OH (left-side in Fig. 6.10) and CH_3OD (right-side) from <1 ML to ~ 2 ML, and present the 3D plots of 2PP intensity decay profiles plotted as a function of both energy and pump-probe delay. The

motivation for performing 2PC measurements on the deuterated molecule is the well-documented $\sqrt{2}$ slower inertial component of solvation of electrons in D₂O as compared with H₂O. The observation of such an isotope effect would provide additional information on the molecular response to the injection of excess electrons.

In Fig. 6.10, each 3D plot is constructed from the 2PC intensities at 14 different energies encompassing the methanol resonance. Horizontal cuts through the 3D plots (e.g. Fig. 6.10 (1b)) give the original two-photon correlation (2PC) scans. By simulating the 2PC scans based on the above model for both the H and D substituted molecules we can present and compare the extracted time constants for related processes in Fig. 6.11. As can be seen in Fig. 10, the proposed model provides a good representation of the observed dynamics. The deduced decay parameters from the simulation show the following trends: i) at low coverages (≤ 1 ML), the methanol resonance decays in < 30 fs independent of energy or isotopic substitution; ii) above 1 ML coverage both the excited state population and its energy decay with fast and slow components; iii) only the slow decay components depend strongly on the methanol coverage; and iv) most significantly, the slow population decay shows a pronounced deuterium isotope effect.

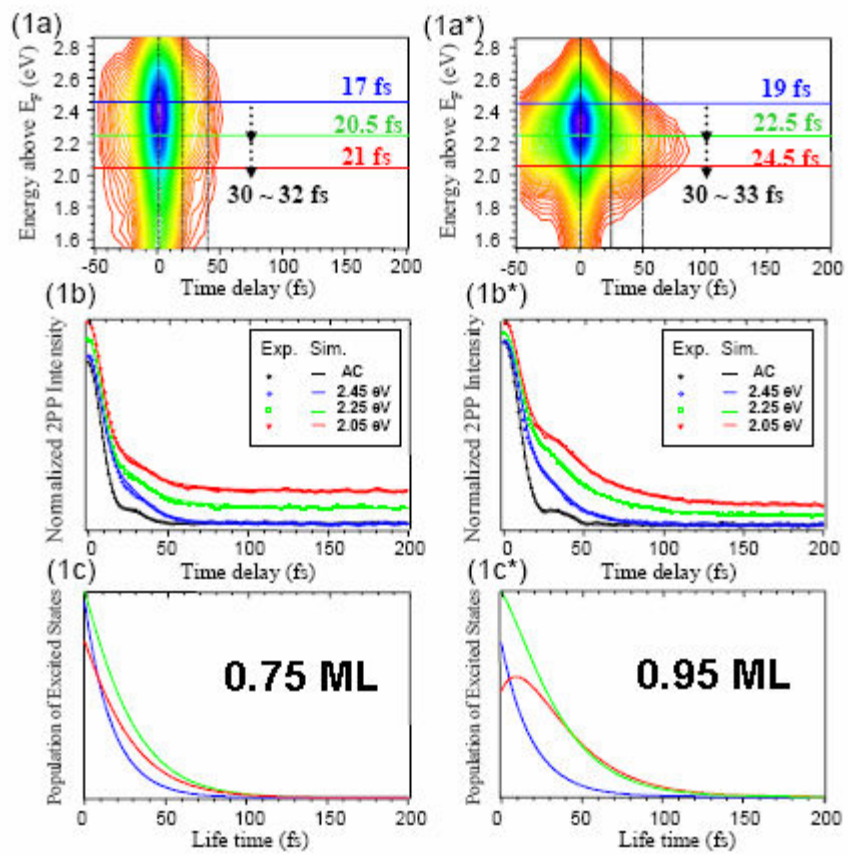


Figure 6.10-1

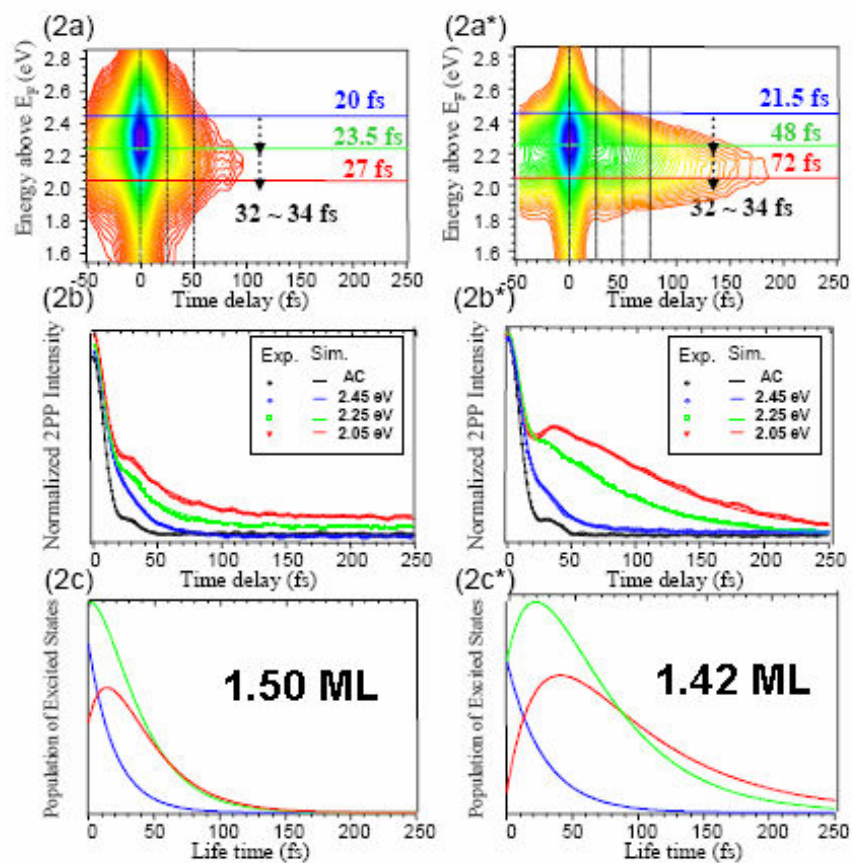


Figure 6.10-2

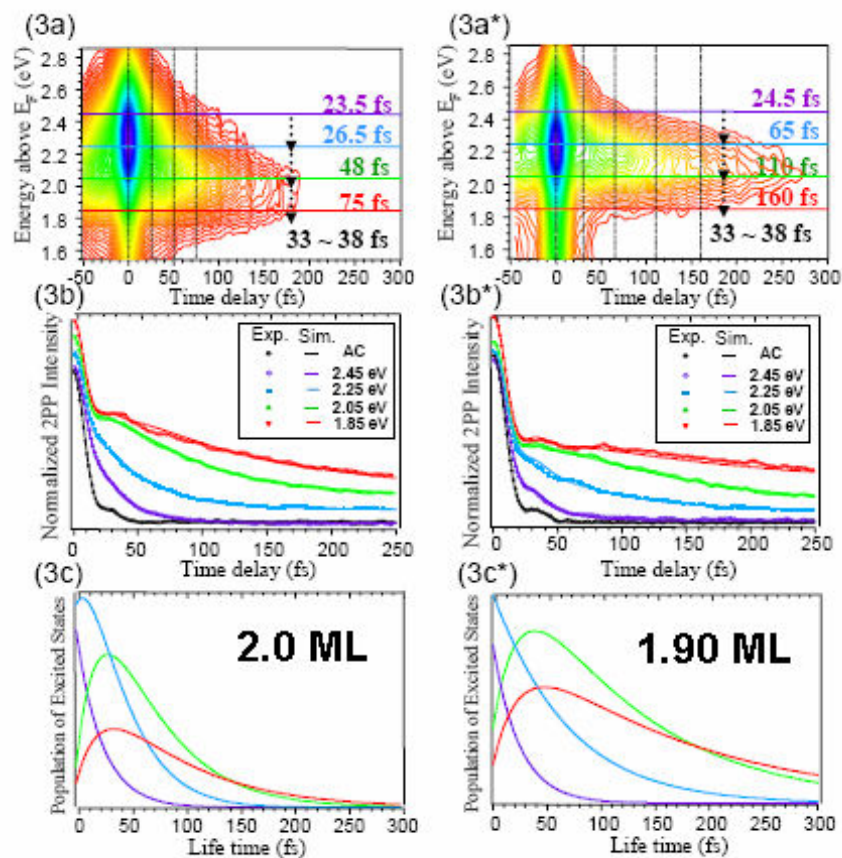


Figure 6.10-3

Figure 6.10 (1a, 2a, 3a) The 3D contour plots of the 2PP intensity decay profiles of the wet-electron states on CH_3OH adsorbed $\text{TiO}_2(110)$ surfaces with coverages of ~ 0.85 ML, ~ 1.5 ML and ~ 2.0 ML). (1b, 2b, 3b) The original two-pulse correlation signals (2PC) used to construct the 3D plots for several characteristic energies near the wet electron resonance that are indicated by color coded horizontal lines in parts a). The solid lines show the simulation of the experimental results according to the model described in Fig. 6.9. (1c, 2c, 3c) are the wet-electron population time-evolution profiles at each of the representative energies used in the

simulation, coded with same colors in (1b-3b). The black arrows in each of the 3D plot indicate the coverage independent feature of the energy relaxation from N_1 to N_{1^*} in a time constant of 30 ~ 40 fs. The corresponding measurements or simulations for the CH_3OD dynamics are presented on the right side of CH_3OH results.

The results presented in Fig. 6.11 show the characteristic time scales for the fast and slow decay components for the protonated and deuterated molecules. Based on the time scales, the nature of the decay process, and the isotope effect we attribute the physical and chemical interpretation to the observed the electron dynamics in the methanol overlayer. As we discussed previously, the dynamics of electrons described by $N_1(t)$ involve both the population decay and energy relaxation to the 1^* state. The population decay probably occurs by RCT into the conduction band of TiO_2 as for $\text{H}_2\text{O}/\text{TiO}_2$. Simultaneously, N_1 decays in energy by ~0.1 eV to a quasi-stationary state 1^* on a time constant τ_{11^*} within 30 – 40 fs (Fig. 6.10). According to Fig. 6.11, the time scale for the decay of N_1 is essentially isotope independent, since the slope for τ_1 of 1.1. Because the photoexcitation involves the charge redistribution from the $\text{Ti}_{5c}^{+4-\delta}$ sites to the methanol overlayer, the fast energy relaxation process probably involves polaron formation. The photoinduced charge redistribution prompts the inertial screening response of the lattice ions. This assignment is consistent with the energy and time scales for polaron formation through the excitation of ~24 THz longitudinal optical phonons in TiO_2 crystal [123]. Substantial electron-lattice correlation in TiO_2 is also evident in both the electronic structure of bridging oxygen atom

vacancy defects and the transient photoconductivity of TiO₂ [10, 123]. This inertial dielectric response stabilizes N_{1*} with respect to the population decay by RCT.

The observed trends for the evolution of the 1* state given by N_{1*(t)} can be used to interpret the photoelectron dynamics below the CH₃OH resonance energy (e.g. 2.05 eV, Fig. 6.10 (2b*)) for the 1* state. A rise time τ_1 and a slower RCT population decay kinetics τ_{1*} with coverage and isotope dependence, characterize the 2PC signal at this energy. The energies corresponding to the 2PP intensities maximum relaxes first because of the fast polaron formation in 30-40 fs, and for longer delays, on account of a much slower process with time scale of > 200 fs (e.g. Fig. 6.10 (2a*)). Based on similar 2PP measurements for CH₃OH/Ag(111), we attribute this energy relaxation process to the injected charge solvated by CH₃OH molecules with a time constant τ_{sol} [124]. Thus, the total decay rate of N_{1*(t)} can be described as a joint effect including a reverse charge transfer process and injected charge solvation in the CH₃OH overlayer,

$$\frac{1}{\tau_{1*}} = \frac{1}{\tau_{RCT}} + \frac{1}{\tau_{sol}}.$$

By contrast to the decay of the primary, photoexcited state 1, the dynamics described by N_{1*(t)} exhibit a strong deuterium isotope effect, according to the slope of 2.2 ± 0.05 reported in Fig. 6.11. Since solvation in liquid methanol is isotope independent [125, 126], the source of the observed isotope effect lies most likely in the RCT dynamics. Isotope substitution can affect rates of kinetic processes through different mechanism [31], which may be differentiated through

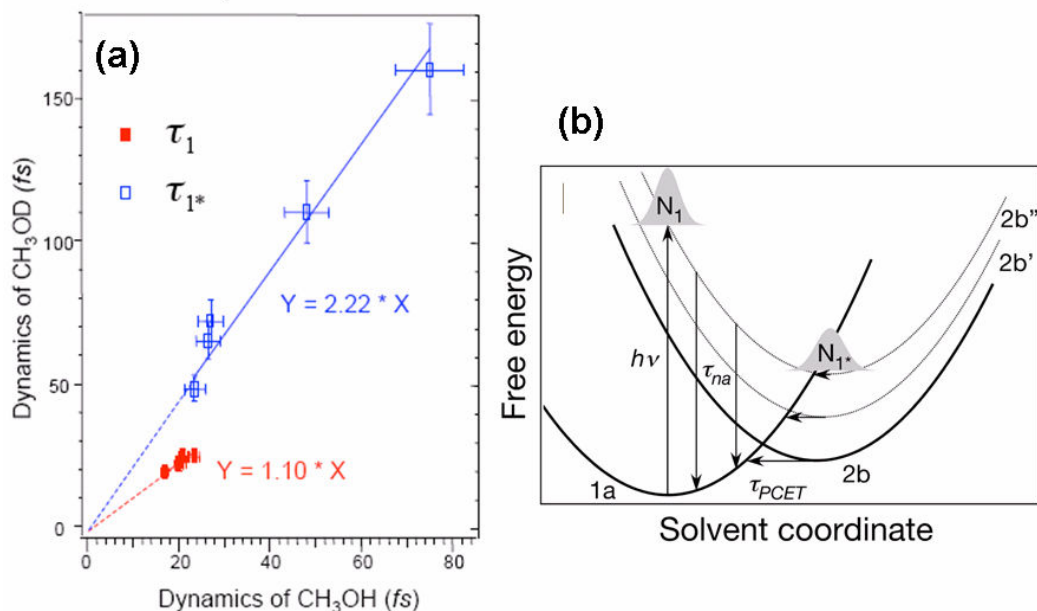


Figure 6.11 (a) The τ_1 and τ_{1^*} lifetimes determined for comparable coverage and observation energy for the CH₃OH/TiO₂(110) (abscissa) and CH₃OD/TiO₂(110) (ordinate) surfaces. (b) Schematic free energy surfaces for the proton-coupled electron transfer (PCET) plotted against a generalized solvent coordinate. The solid lines represent surfaces for an electron and a proton before (1a) or after (2b) photoinduced transfer; the dotted line (2b' and 2b'') represent manifold 2b surfaces with different degrees of proton vibrational equilibrium ground state structure (N_1 state) evolve through the inertial dielectric response toward the 2b manifold minima (N_{1^*} state). The nonadiabatic electronic decay (down arrows) most likely occurs before crossing of the 1a manifold with the 2b manifold. The PCET is the most probable at surface crossing between the 1a and 2b manifolds (horizontal arrows).

the magnitude of the observed ratio of kinetic parameters. For example, an isotope effect of $\sqrt{m_D/m_H} \sim 1.4$, that was observed in the inertial component of electron hydration in liquid H₂O [126], has been attributed to the inertial response of the solvent molecules involving molecular liberation. The substantially larger isotope effect on τ_{1^*} of 2.2 is significantly larger than the reduced mass ratio for any conceivable kinetic process involving the motion of single proton or proton containing species such as vibration or liberation. The larger ratio, therefore, implies either that the kinetic process involves the motion of multiple protons, or the tunneling motion of protons where the reduced mass effect enters in an exponent [127].

The reverse charge transfer dynamics associated with the N_{1*} population relaxation, which exhibit a significant isotope effect, cannot be explained by a purely electronic process (e.g. inelastic electron scattering). Rather, they are indicative of a correlated electron transfer process that is mediated by the motion of protons or H atoms, i.e. proton-coupled electron transfer (PCET), which is well documented in homogeneous photocatalysis [128, 129], but our results show first evidence for such dynamics for molecular overlayers on solid surfaces. Based on this understanding, we describe the total decay rate of N_{1*(t)} with a modified expression,

$$\frac{1}{\tau_{1^*}} = \frac{1}{\tau_{PCET}} + \frac{1}{\tau_{sol}}.$$

Photoinduced electron transfer under highly nonequilibrium conditions, such as in the dye sensitized charge injection or the wet electron population decay into TiO_2 , cannot be described by quasi-equilibrium models such the Marcus-Jortner theory [24, 130, 131]. However, in Fig. 6.11 (b) we draw on the formalism of the Marcus-Jortner theory to propose a scenario for how the inertial structural changes are associated with the dielectric response of the interface control the wet electron dynamics.

The free energy surfaces for the proton and electron transfer are plotted in Fig. 6.11 (b) against a generalized solvent coordinate representing the multi-dimensional dielectric response of the interface to both the electron and proton displacements [127]. Photoexcitation occurs “vertically”, that is, faster than the proton or solvent response, shown in Fig. 6.11 (b), from the donor surface 1a (electron at the $\text{Ti}_{5c}^{+4-\delta}$ sites and proton at its ground state geometry) to a manifold of acceptor surfaces 2b, 2b', 2b'', etc. This manifold represents the excited state where an electron is in the CH_3OH overlayer and a proton is displaced with respect to the ground state, with different degrees of excitation of an internal proton vibration. Because at the instant of excitation, a proton in the excited state is strongly displaced along these internal coordinates, the optical transition terminates on a distribution of vibrationally excited free-energy surfaces. The wave packet created on the 2b manifold evolves toward the surface minimum through the inertial dielectric response. In competition with the dielectric relaxation, the excited state population

decays by nonadiabatic processes, which change the state occupation (vertical transitions), and by PCET processes, which exchange the proton and electron between the donor and acceptor states (horizontal transitions) [130]. Exothermic non-adiabatic transitions occur before the wave packet propagates to crossings of the 1a manifold with the 2b manifold. By contrast, PCET is most probable at crossings between 1a and 2b manifolds, where the activation energy (solvent reorganization) is minimum. As the excited state evolves toward the equilibrium structure of wet electron state, the transition from non-adiabatic to PCET-dominated population decay is revealed by the emergence of the deuterium isotope effect.

6.6 DFT Electronic Structure Interpretation of the PCET Dynamics

To gain further insight into the PCET process, Dr. J. Zhao performed DFT calculations of the molecular and electronic structure of CH₃OH/TiO₂ surface [89, 117]. The ground state geometry (Fig. 6.2) with the unoccupied electronic structure is calculated for a 3-layer TiO₂ slab covered by 1 ML of CH₃OH, where 50% of the molecules are dissociated. The unoccupied wet electron orbital in the methanol overlayer was identified as for H₂O/TiO₂ [76]. In order to optimize the excited state structure, the delta self-consistent (Δ -SCF) DFT calculation is performed on a single layer of TiO₂ that is cut from a 3 layer slab of the optimized ground state structure (Fig. 6.12 A and B). In this calculation, an electron is added to the wet electron orbital, which is mainly

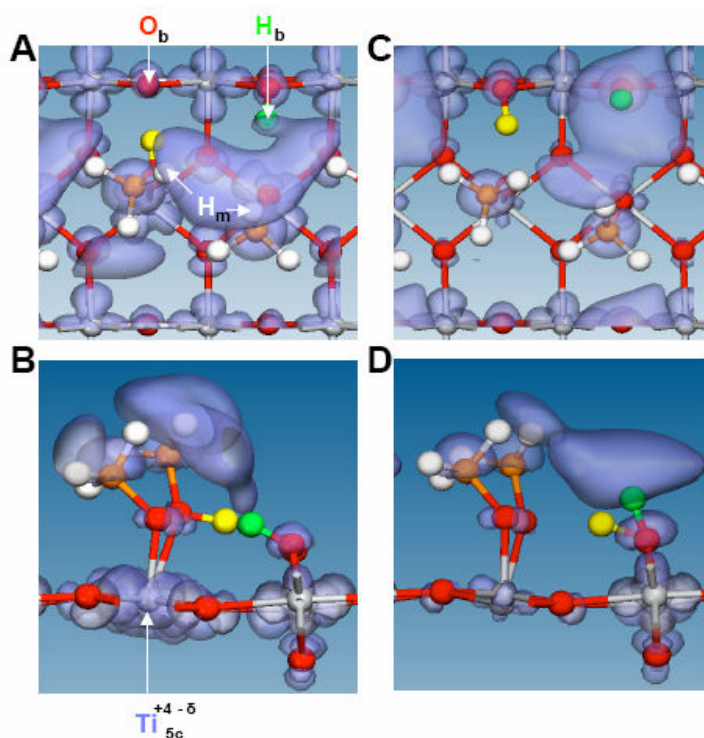


Figure 6.12 (A and B) Top and side views of the optimized geometry of the ground state and the associated lowest (2.5 eV) unoccupied adsorbate localized orbital of 50% dissociated CH₃OH at 1 ML coverage on TiO₂(110) as obtained from DFT calculations [115, 116]. Ti, O, C, and H atoms are designated by blue, red, orange, and white (green and yellow), respectively. The arrows indicate the bridging oxygen O_b, terminal five-coordinate titanium Ti_{5c} rows, and methyl H_m atoms. The translucent structures indicate the unoccupied orbital distribution of the wet electron state. (C and D) The top and side views of the optimized geometry of the electronically excited state. The primary structural change from A and B is rotation of the bridging -OH (green) towards the surface normal configuration, followed by the transfer of proton (yellow) from the CH₃OH to the proximate O_b site. Simultaneously, the wet electron distribution descends towards the surface from the methyl groups to the bridging -OH.

localized on methyl hydrogen (H_m) atoms. Thus formed excited state structure is optimized while keeping all the surface atoms of the substrate except bridging oxygen (O_b) fixed. The optimized structure is attained after substantial displacement of H atoms belonging to OH groups on the surface H_b (green) and CH_3OH (yellow), as shown in Fig. 6.12 C and D, with concomitant shift of the excited state electron distribution from H_m to H_b atoms. By following the H atom positions at each structure optimization step, we find that the primary rotation of the bridging -OH (green) to the vertical orientation contributes 80% of the ~ 0.5 eV stabilization energy, while the secondary transfer of a proton from CH_3OH (yellow) to its neighboring O_b site is responsible for the rest.

The excited state calculations provide insight into this PCET dynamic mechanism that could account for the D isotope effect observed at >1 ML coverage. The calculated concerted H^+/e^- transfer for <1 ML CH_3OH occurs without an energy barrier, and therefore, the PCET process should be rapid and not exhibit an isotope effect that is larger than implied by the reduced mass for the calculated motion. While for methanol coverages of >1 ML, the second layer molecules chemisorb by forming a hydrogen bond with the O_b atoms. Since this perturbs the existing hydrogen bond structure, it can impose an energy barrier to hinder the proton motion in Fig. 6.12, and thereby give rise to the isotope effect that stabilizes wet electrons on H_m atoms [96]. Here, the role of second layer CH_3OH molecules may be to gate the H^+/e^- transfer, and therefore retard the charge transport through the molecule-oxide interface, causing the time scales of electron decay correlated with proton motion increases significantly.

There are reports about the intermolecular proton transfer or tautomerization processes in solvents. At the barrierless case, it occurs in time scales of tens of fs [132, 133]; the PCET process tunneling through some energy barrier, for example the photo-induced double-proton transfer in DNA base pair structures is corresponding to several hundred fs to pico-second time scale [134, 135]. Our measured time scales, spanning from 25 fs to 160 fs are in the range of well-documented PECT process [128, 129], however, the values we presented include both the times for the adiabatic avoided cross section search and for electron inelastic scattering decay in the conduction band (CB) of the substrate, just giving the upper temporal limit of the proton transfer process..

Fig. 6.13 summarizes the overall scheme for the electronic structure and dynamics of the CH₃OH/TiO₂ interface that are investigated in our TR-2PP experiments. On TiO₂(110) surfaces reduced by creation of O_b vacancies or by chemisorption of electron donating adsorbates, e.g. H atoms, the excess surface charge is delocalized over several Ti_{5c}^{+4-δ} sites forming a band 0.1 eV below the CB minimum with a maximum DOS appearing ~0.9 eV below E_F. Excitation with 3.05 eV light induces charge transfer from this defect band to an acceptor state in the CH₃OH overlayer around 2.3 eV above E_F [118].

The photo-induced charges are transferred to an excited state whose geometry is displaced from the equilibrium geometry of ground state along several coordinates, and are associated with a complex electronic decay and solvation process. These coordinates are related to the creation of the hole in the TiO₂ substrate, and injection of an electron into the CH₃OH overlayer. The creation of a hole excites the Ti-O bond stretching vibration. Likewise, the injection of an electron into the molecular overlayer excites the motion of the electropositive H atoms. Both motions can lead to the fast energy relaxation associated with the dielectric screening of the photogenerated charge distribution, where the energy and time scales are consistent with the polaron formation dynamics in TiO₂ [123].

Simultaneously with the screening of the excited state charge distribution through the inertial motion of heavy nuclei, the photoexcited excess charge can decay through a nonadiabatic RCT into the CB of TiO₂. Meanwhile, the aforementioned fast energy relaxation process via polaron formation, feeds the lower lying states N₁*, whose population dynamics clearly shows a delayed rise and a slower decay, as well as a significant D isotope effect of factor 2.2. According to the previous discussion, the lower-lying state N₁* decays through a correlated electron-proton motion, i. e. the PCET process (Fig. 6.13).

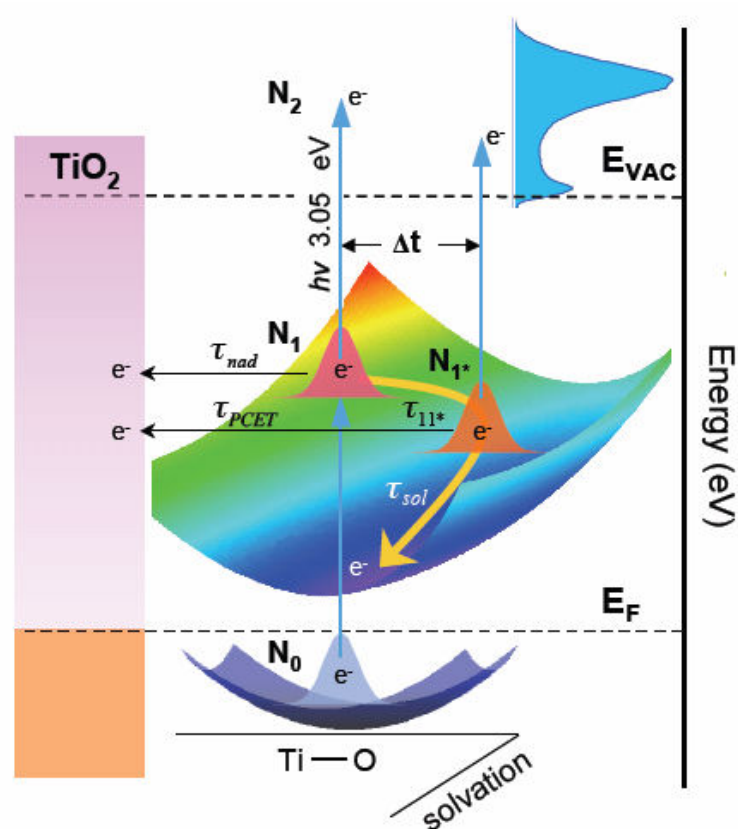


Figure 6.13 Schematic diagram for the 2PP excitation at the CH₃OH/TiO₂ interface. The photoinduced charge transfer from the partially reduced Ti_{5c}^{+4-δ} sites (N₀) to the CH₃OH overlayer (N₁) initiates the coupled electron-nuclear dynamics. The charge redistribution elicits dielectric response involving fast nuclear motion of the Ti-O bonds (polaron formation), along with slower motion of adsorbate molecules (solvation), thereby relaxing the initially prepared N₁ state to the quasi-stable N₁* state. Simultaneously, the population decay evolves from the nonadiabtic (τ_{nad}) to the proton-coupled (τ_{PCET}) resonant charge transfer (RCT) regimes. The two-photon photoemission spectra such as shown for 1 ML CH₃OH, and pump-probe two-pulse correlation measurements obtained by further excitation of electrons above the vacuum level (N₂) record the intermediate state electronic structure and relaxation dynamics.

As the result of the structural change of the interface, which leads to the energy stabilization of the primary excited state, a quasi-stable intermediate state forms, from which further relaxation is substantially suppressed. Since this quasi-stable state is substantially displaced from the ground state geometry, it can be stabilized with respect to RCT if the nonadiabatic decay can become endothermic. The continuing energy relaxation of the quasi-stable state can be attributed to the diffusive electron solvation by the molecular overlayer [124, 136, 137]. Our preliminary investigation of the electron solvation dynamics in the ≥ 3 ML CH_3OH overlayers, shows the electron lifetime can be extended to the picosecond range. However, the precise rate of energy relaxation is difficult to quantify because our measurements are limited to delays of 300 fs. Further discussions on this topic of the hydrated electrons will appear in our future publication [138].

Our studies elucidate how the dielectric response of a protic-solvent/metal-oxide interface controls the electron transfer and solvation in a photocatalytic process. Presolvated electrons, such as those observed for $\text{CH}_3\text{OH}/\text{TiO}_2$, are potent reagents that have been implicated in the photocatalytic decomposition of halocarbons, which are relevant to chemical remediation and the destruction of Earth's ozone layer [139]. Conditions exist to support similar wet electron states on all oxide surfaces in contact with protic solvents. However, details of the electronic structure and dynamics most likely depend on the specific molecular-scale solvent-substrate interactions.

Chapter 7

Summary and Conclusions

The goal of the research presented in this thesis is to study the electronic structure (spectroscopy) and electron dynamics at the atomically ordered adsorbate covered TiO₂ single crystalline surfaces by means of the time-resolved two-photon photoemission (2PP) technique. 2PP spectroscopy is mainly used to investigate the unoccupied states of chemisorbed molecular overlayers. Pump-probe measurements with femtosecond time resolution on the energy and population dynamics of transiently excited electrons reveal dynamical processes both within the molecular overlayers on the TiO₂ surfaces and involving the charge transfer across the interface.

The primary electronic properties of TiO₂ are discussed, mainly focusing on the rutile (110) surfaces. The most important industrial applications of TiO₂ are reviewed, e.g. the photocatalytic splitting of H₂O, or the TiO₂ based photovoltaic solar cells. The advantages and importance of applying the femtosecond 2PP techniques to study the molecule/TiO₂ system have been addressed.

The 2PP experimental apparatus used in our measurements is extensively described. The components of the optical system include the self-made Ti:Sapphire laser oscillator cavity that generates ~ 10 fs laser pulses, the nonlinear optical generation of near UV light, and the Mach-Zehnder Interferometer for the generation of time-correlated pump probe pulses. The optical pulses are delivered to the UHV photoemission apparatus, where the 2PP measurements are performed. The UHV apparatus, including the sample preparation facilities, the ultra-high vacuum pumping systems, along with the photoemission measurement devices and methods have been discussed in detail. Most importantly, the electron energy analyzer and channeltron detectors are extensively discussed. The details of the data acquisition, the diagnostics and the signal processing/analysis are presented.

The theoretical section describes the 2PP process, including effects such as hot electron relaxation dynamics at a solid-state surface, that can affect the experimental results. Moreover, a theoretical description of the nonlinear interferometric autocorrelation measurement, the Optical Bloch Equation (OBE) method as they pertain to the analysis two-photon process and the electron dynamics simulation/fitting procedures are presented.

2PP spectroscopic investigations on bare stoichiometric and modified TiO_2 surfaces are discussed for various surface preparation methods. Experiments are performed under the UHV environment for surfaces modified by annealing in UHV to 1000 K, energetic electron (500 eV)

bombardment, as well as Ar^+ sputtering. The sensitivity of different surface preparation methods to O_2 adsorption are discussed with particular emphasis in the interaction of O_2 molecules with the surface O atom vacancy sites.

The H_2O chemisorption on and interaction with TiO_2 surfaces are extensively studied. The overall electronic structures of the $\text{H}_2\text{O}/\text{TiO}_2$ system and the work function changes due to the H_2O deposition to induce a surface dipole layer are systematically studied via 2PP spectroscopy. Most remarkably, at the coverage of one monolayer H_2O molecules and minority $-\text{OH}$ terminated species on TiO_2 surfaces, an unoccupied electronic state is observed at 2.4 eV above the Fermi level. Density functional theory (DFT) shows this resonance can be described as a partially hydrated electron or “wet-electron” state. The dynamics of the wet-electron state is studied by time-resolved 2PP, indicating the electron decay from the wet-electron state occurs in less than 15 femtoseconds.

The same time-resolved 2PP technique also is employed to study the electronic structure and dynamics of CH_3OH overlayers chemisorbed TiO_2 surfaces. A similar wet-electron excited state to $\text{H}_2\text{O}/\text{TiO}_2$ is discovered. It displays a broadband molecular resonance feature with energy of 2.3 eV above the Fermi level. However compared to H_2O , this CH_3OH induced wet-electron state exhibits much more complex dynamics, which are strongly coverage dependent; especially at the coverage of above one monolayer, the CH_3OH dynamics display both the population decay and energy relaxation processes, including both fast and slow decay components, as well as a

deuterium isotope effect. A kinetic model is developed to simulate the electron kinetics in the CH₃OH/TiO₂ structure, indicating that the wet-electrons decay through a reverse charge transfer process (RCT) mediated by the correlated motion of H atoms and electrons at the interface. Although such proton-coupled electron transfer process (PCET) is known in homogeneous electron transfer, this is the first example of such dynamics at a molecule/solid interface. The 2D electron diffusive solvation dynamics is also studied. Finally, we find longer, picosecond time scale lifetimes of the hydrated electrons for ≥ 3 -ML CH₃OH coverage, which could be an interesting topic for further investigations.

The “wet-electron” or partially hydrated electron states we observed at the H₂O or CH₃OH/TiO₂ surfaces represent the lowest energy pathway for the nonadiabatic electron transfer. The energy level (2.3 ~ 2.5 eV) is associated with the minimum energy that photons must deliver to transport electrons through the interface into the molecular overlayer. Such electrons can drive photochemical or photocatalytic reactions of molecules in the chemisorbed overlayer. Our research is also relevant to the photosensitized charge injection for the dye-molecules/TiO₂ system, where wet electron state can present a similar low energy pathway for transport into the conduction band of TiO₂. Furthermore, similar wet electron states are likely to exist on all protic solvent covered metal oxide surfaces. Their participation in chemical and physical processes in UHV and under atmospheric conditions can now be investigated by methods described in this thesis.

APPENDIX A

THE TYPICAL PARAMETERS OF THE 2PP SPECTROSCOPY

The typical parameters for recording 2PP spectra shown in Fig. 2.10 will be briefly discussed here. 1) **Start** energy and **End** energy are 9.80 eV and 12.00 eV. Since we employ a bias voltage of 5 eV between the sample and the energy analyzer, the measured energy range of measured spectra actually covers 4.80 ~ 7.00 eV above the Fermi level. 2) **Step** 0.02 eV and **Dwell** time 0.5 s give the energy interval between each measured points and the integration time for the photoemission counts at each energy. 3) **Mode** CAE, 5.0 eV means that the analyzer is operating in Constant Analyzer Energy mode with average pass energy of 5.0 eV (Section 2.2.2). 4) **Mag.** -“Low” means that the “low magnification mode” is employed, where the focal plane of the electrostatic input lens is far behind the sample, so the lens accepts electrons emitted in a narrow cone of angles from a large area. 5) **Ent.** Slit of 6 mm dia. and **Exit** Slit of 3 x 10 mm give the entrance aperture of 6 mm diameter, while the exit slit has the given rectangular dimension for each of the 7 channels. From Fig. A.1, there are three options for the exit slit; we generally employ the medium size dimension of 3 x 10 mm. 6) # **Ch.** 7, means that the analyzer is working in a 7-channel acquisition mode, i.e. 7 channeltrons are measuring photoelectrons simultaneously and presenting 7 parallel energy spectra after each scan.

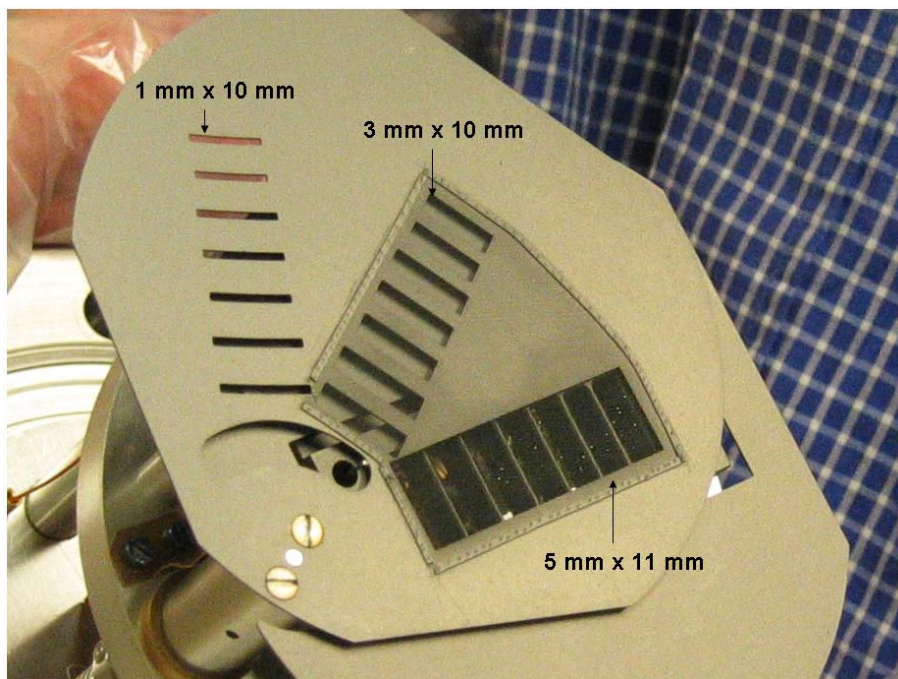


Figure A.1 The photo of the analyzer's exit slit plate.

The other information can also be found in the screenshot window as well, such as the excitation energy ~ 3.1 eV, the experiment date and time, and etc.

APPENDIX B

SOFTWARE FOR TIME-RESOLVED EXPERIMENT

We developed a software package for control of all the optoelectronic devices and computer boards (Fig. 2.11) for signal processing, data acquisition and storage in our time-resolved two-photon photoemission experiment. The following diagram (Fig. B.1) illustrates the electronic signals in the experiments, and is very helpful to describe the operation of the overall software.

Our software includes four major functions (or operations) in the current time-resolved 2PP experiment: **1)** Sending a signal through a GPIB board to generate the “Sawtooth Wave” with the SRS 345 functional generator; **2)** Sending a command to one of the NI-DAQ boards (1), requesting the control box 1 to acquire analog interference fringes from the photodiode and to save the data; **3)** Sending a command to the other NI-DAQ board (2), to generate a sequence of TTL signals that act as the “external trigger signal” for the Omicron data acquisition card; **4)** Directing the TTL signals to trigger the Omicron card to record the photoemission counts from the channeltron detectors.

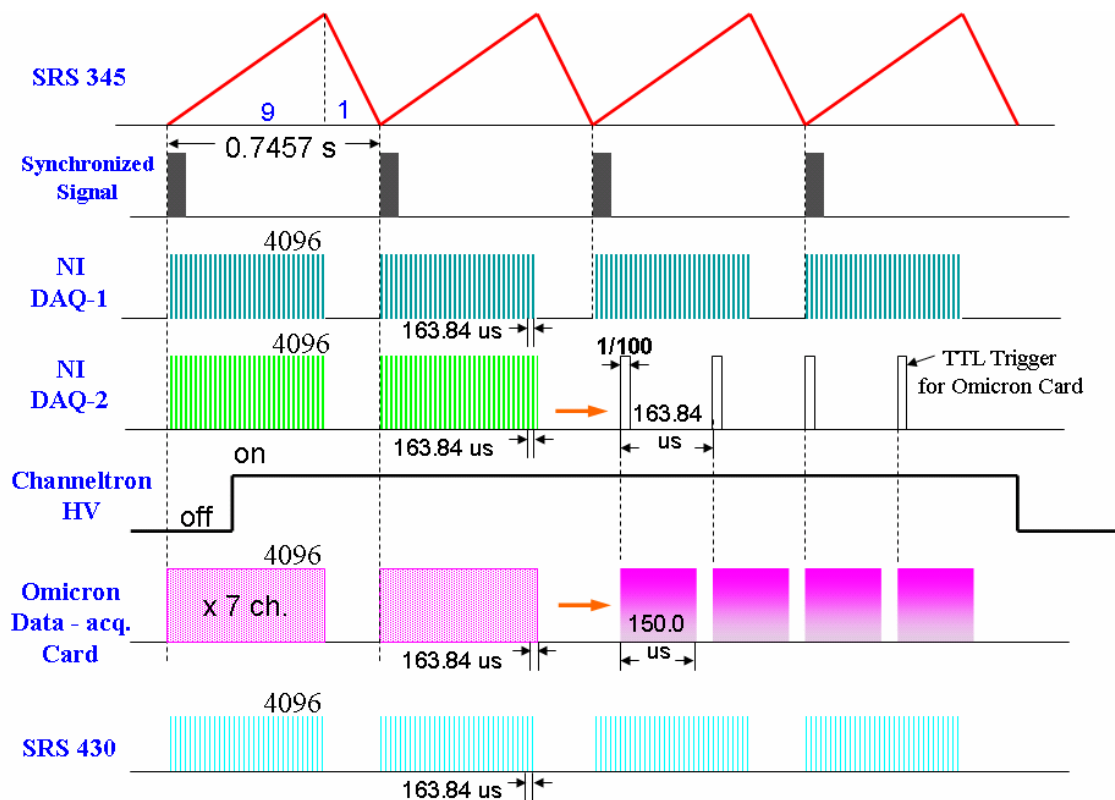


Figure B.1 The synchronized electronic signals in the various electronic devices and computer cards (boards).

The software is also able to send commands through the GPIB board to turn on/off the channeltron high voltage to start/terminate the data acquisition process. Moreover, the software includes the codes to record the photon counts at SRS 430, which is originally designed to record the SSHG signals for the laser-pulse diagnostics. We will describe the software components individually.

B.1 The parameter file, which serves as an input file including a set of appropriate parameters for each of those electronic devices functioning synchronized in a TR-2PP experiment.

DEFAULT PARAMETERS FOR 2PP EXPERIMENTS

(The data in numeric lines would be retrieved for parameter-settings)

--- Display Settings, AD = 0, MSC = 1, SAC Ch1-7 = 2-8 ---

//Define the positions of each panel in the display window.

top plot:

0 //Top panel is used to display the interfering fringe signals from DAQ-1 card.

middle plot:

1 /* Middle panel is supposed to display the SSHG from SRS 430, however we don't have the experimental data presently. */

bottom plot:

2 /*Bottom panel could be used to display the I2PC electron-counts from any of the seven channeltron detectors. */

--- Function Generator (SRS 345) Settings ---

amplitude (V):

0.8 // Set the peak to peak amplitude of Sawtooth wave to 0.8 volt.

offset (V);

0.0 // Set the offset of the Sawtooth wave to zero

frequency of point (Hz): (14920 points, minimum value) (20000 x 1, 2 ,4)

20000 /* The Sawtooth wave cycle includes 14920 small points, each of which has a time duration 1/20000 second, so the Sawtooth wave cycle corresponding to a piezo-scanning motion cycle is: $14920/20000=0.746$ s. We only use part of the increasing wave (90%) as the piezo-scanning time-delay modulation, so the each data acquisition (or pump-probe) cycle is less than $0.746*0.9=0.6714$ s. */

--- Multichannel Scaler (SRS 430) Settings ---

binwidth (11=40.96us 12=81.92us, 13=163.84us, 14=327.68us):

13 /* Each time-bin or per data acquisition duration at each of time-delay intervals is
163.84 us. */

number of bins (1=1k):

4 /* Total number of the data in each data acquisition cycle or pump-probe cycle is
4096, therefore each data acquisition cycle corresponds to $4096*163.84$ us = 0.6711 s */.

number of iteration:

20 //We don't have SSHG data, so this really doesn't matter.

---AD Board (NI-DAQ) Settings ---

sampling rate (sec): (0.00016384, 0.00008192, 0.00004096)

0.00016384 /* Set the time-duration per data acquisition interval in NI-DAQ 1 same as
that of SRS 430, 163.84 us. */

number of data points (less than 5000, usually 4096):

4096 // Total number of the data in each pump-probe cycle is also the same 4096.

number of iteration:

1 // We just need one set of the interferometric fringe signal as time-delay reference.

--- Omicron SAC Card Settings ---

number of channel:

7 /* Typically, 7 channeltron detectors are functioning all-together, thus we need the Omicron Card to store all of the 7 different data-sets. */

dwelt time (micro sec, integer only):

150 /* Only the first 150 us in the 163.84 us is used to collect the photoelectron counts, the rest of 13.84 us is the deadtime used to clear the memory to record the data for the next time-delay interval. */

number of data points (each channel, usually 4096):

4096 // Total # of data acquisition in each pump-probe cycle is always the same 4096.

number of iteration only for SAC card (total=AD x SAC):

1000 /* The iteration of data acquisition for SAC card, the different channels can be functioning simultaneously and coincidently. */

--- Analyzer Settings ---

pass energy

5 // The pass energy for the CAE (Constant Analyzer Energy) mode is always 5.

B.2 The software opens the input file “TR-2PP_2003.txt”, and retrieves and transfers the preset parameters to all the participating electronic devices for initialization.

```
CGraphDoc::CGraphDoc () // Class Initialization and Parameters Reading.
{
    // TODO: add one-time construction code here

    char dummy[128]; // Temporary memory allocation for data-storage.
    FILE *fp; //Temporary file pointer

    if((fp=fopen("TR-2PP_2003.txt","rt"))==NULL){
        AfxMessageBox ("Cannot open Default.txt!");
        exit(0); }

    // The command to open the input file, including malfunction treatment.

    fgets(dummy, 128, fp); // title, return button and memory reallocation
    fgets(dummy, 128, fp); // display settings, return and memory reallocation
    fgets(dummy, 128, fp); // non-numeric buffer, return and memory reallocation

    fscanf(fp, "%d\n", &Panel0);

    // Set top panel to display the interfering fringe signals
    fgets(dummy, 128, fp); // return to next line, memory reallocation
    fscanf(fp, "%d\n", &Panel1); //Set middle panel to display the data from SRS 430
    fgets(dummy, 128, fp); // return to next line, memory reallocation
    fscanf(fp, "%d\n", &Panel2); //Set bottom panel to display the one of the 7-chns.
```

```

fgets(dummy, 128, fp); // SRS345 settings, return to next line, memory reallocation

fgets(dummy, 128, fp); //return to next line, memory reallocation

fscanf(fp, "%f\n", &AMP_DS345); //Set amplitude for SRS345 (or DS345)

// The SRS345 is labeled as DS345 in the software!

fgets(dummy, 128, fp); //return to next line, memory reallocation

fscanf(fp, "%f\n", &OFFSET_DS345); //Set offset for SRS345

fgets(dummy, 128, fp); //return to next line, memory reallocation

fscanf(fp, "%lf\n", &FRQ_DS345); // Set single-point frequency for SRS345

fgets(dummy, 128, fp); // SR430 settings, return to next line, memory reallocation

//SRS430 is labeled as SR430 in the software

fgets(dummy, 128, fp); //return to next line, memory reallocation

fscanf(fp, "%d\n", &BINWIDTH_SR430); //Set time-bin duration for SRS 430

fgets(dummy, 128, fp); //return to next line, memory reallocation

fscanf(fp, "%d\n", &NumBINS_SR430); //Set the number of time-bin for SRS 430

fgets(dummy, 128, fp); //return to next line, memory reallocation

fscanf(fp, "%d\n", &ITRE_SR430); /*Set the iteration time of data-acquisition
                                cycles for SRS 430 */

fgets(dummy, 128, fp); //DAQ Board, return to next line, memory reallocation

//NI-DAQ Board is simplified as AD board in software.

fgets(dummy, 128, fp); //return to next line, memory reallocation

```

```

fscanf(fp, "%lf\n", &RATE_AD); /* Set the time-duration per data acquisition
                                interval in NI-DAQ 1 */

fgets(dummy, 128, fp); //return to next line, memory reallocation

fscanf(fp, "%d\n", &NumDATA_AD); /*Set number of data points for each data
                                acquisition cycle for NI-DAQ 1. */

fgets(dummy, 128, fp); //return to next line, memory reallocation

fscanf(fp, "%d\n", &ITRE_AD); /*Set the iteration time of data-acquisition
                                cycles for NI-DAQ 1 */

fgets(dummy, 128, fp); // Omicron Board, return to next line, memory reallocation
//Omicron data-acquisition card is simplified as SAC board in the software.

fgets(dummy, 128, fp); //return to next line, memory reallocation

fscanf(fp, "%d\n", &NumCH_SAC); /*Set the number of channels functioning
                                coincidentally for Omicron SAC board */

fgets(dummy, 128, fp); //return to next line, memory reallocation

fscanf(fp, "%d\n", &Dwell_SAC); /*Set the time-duration for each of the data
                                acquisition interval for SAC board*/

fgets(dummy, 128, fp); //return to next line, memory reallocation

fscanf(fp, "%d\n", &NumDATA_SAC); /*Set number of data points for each data
                                acquisition cycle for Omicron SAC Board. */

fgets(dummy, 128, fp); //return to next line, memory reallocation

```

```

fscanf(fp, "%d\n", &ITRE_SAC); /*Set the iteration time of data-acquisition
                                cycles for SAC Board */

fgets(dummy, 128, fp); /* Energy analyzer setting, return to next line, memory
                        reallocation */

fgets(dummy, 128, fp); //return to next line, memory reallocation

fscanf(fp, "%d\n", &PE); //Set the pass energy for the energy analyzer

fclose(fp); // Close the input file

NumData0=0; //Data initialization for later purposes.

NumData1=0;

NumData2=0;

} // The end of CGraphDoc () class!

```

B.3 GP-IB Control and Initialization

```

#include "WINDECL.h" //System headfile

#define BDINDEX      0 // Set GPIB-Board Index as 0

#define PRIMARY_ADDR_OF_SCOPE_1  8 // Primary address for SR430, 8

#define PRIMARY_ADDR_OF_SCOPE_2  19 // Primary address for DS345, 19

#define NO_SECONDARY_ADDR  0 // Secondary address of both devices are 0

#define TIMEOUT      T10s // Timeout value = 10 seconds

```

```
#define EOTMODE      1    // Enable the END message
#define EOSMODE     0    // Disable the EOS mode
```

B.4 Set DS345 to generate the Sawtooth wave for the piezoelectric actuator scanning.

```
void CGraphDoc::SetWave() // Construct a class for DS345
{
    int DS345; //definition of DS345
    char cmd[40]; //memory allocation for a string buffer
    int i, sum, number; //definition integers inside the current class
    short data[100]; //memory allocation for an data array of short integers

DS345 = ibdev(BDINDEX, PRIMARY_ADDR_OF_SCOPE_2, NO_SECONDARY_ADDR,
TIMEOUT, EOTMODE, EOSMODE);

    //Device DS345 Initialization with some default setting parameters.

    if (ibsta & ERR)
        {AfxMessageBox("Unable to open device DS345");}

        //Turn on the DS345 for functioning!

    ibclr(DS345);

    if (ibsta & ERR)
```

```

{AfxMessageBox("Unable to clear device DS345");}

// Clear the Device DS345

sprintf(cmd, "AMPL %f VP\n", AMP_DS345);
ibwrt (DS345, cmd, strlen(cmd));

// Set the amplitude for the generated wave in DS345

sprintf(cmd, "FSMP%lf\n", FRQ_DS345);
ibwrt (DS345, cmd, strlen(cmd));

/* Set frequency for each point in a mode of multi-point-sequence (N), so the total
duration for each data-acquisition cycle should be equal to  $N*(1/FRQ\_DS345)$ . */

    sprintf(cmd,"OFFS%lf\n", OFFSET_DS345);
    ibwrt (DS345, cmd, strlen(cmd));

//Set the offset for the wave in DS345

    sum=0; //Diagnostic value
    number=3; //The three extraordinary points for the Sawtooth wave
    data[0]=0; data[1]=-2047; //x and y coordinates for the first point
    data[2]=14669; data[3]=2047; //x and y coordinates for the second point
    data[4]=16299; data[5]=-2047; //x and y coordinates for the third point

    for(i=0; i<number; i++) sum+=data[2*i]+data[2*i+1]; // diagnostic value

```

```

        data[2*number]=sum; //set check point
    sprintf(cmd,"LDWF?1,%d\n",number); /* Construct the Sawtooth wave
    based on the parameter settings, using the three extraordinary points */
    ibwrt (DS345, cmd, strlen(cmd)); //Write String "LDWF?1,3" to DS345
    ibrd (DS345, cmd, 40); //Retrieving the current status of DS345, ready
    ibwrt (DS345, (char *)data, (long)(4*number+2)); /* Pass the x and
    y coordinates of the three extraordinary points and the diagnostic value into
    DS345 */

    sprintf(cmd,"FUNC5\n"); //vector waveform
    ibwrt(DS345,cmd,strlen(cmd)); /*Sending command to DS345 to generate a
    vector waveform (Sawtooth) using the input data. */

    ibonl(DS345, 0); //DS345 clearing and re-initialization
} // The end of DS345() (or SetWave()) class!

```

B.5 Set the NI-DAQ AD 1 board to record the interfering fringes for delay time calibration.

```

#include "nidaqex.h" //Include an essential headfile

void CGraphDoc::NIDAQControl() //Construct a Class for NI-DAQ board
{
    int i, j;

```

```

/*
* Local Variable Declarations for NI-DAQ
*/

NTimes0=ITRE_AD; // Set the iteration time for data-acquisition cycles

NPoint=NumDATA_AD; // Set number of data points per acquisition cycle

i16 iStatus = 0; /* The status value for NI-DAQ board, where 0 means it is working as an
AD board. i16 is predefined as the “short integer” data type. */

i16 iRetVal = 0; /* Error indicator. If an error occurs, we can tell what kind error it is
from the value of “iRetVal”. */

i16 iDevice = 1; /* The index of GPIB is assigned as 0, and the index of NI-DAQ board is
assigned as Device 1. */

i16 iChan = 1; // Default value

i16 iStartTrig = 1; // 1: means using the external trigger

i16 iExtConv = 0; // 0:Use the onboard clock to control data acquisition

i16 iGain = 1; /* Gain is one, which means the identical transformation from the
input analog signal to the digitized signal */

u32 ulCount = NPoint; /* NPoint = NumDATA_AD, data points per cycle, where u32 is
predefined as “unsigned long integer” */

f64 dGainAdjust = 1.0;

/* No further gain adjustment, f64 is predefined as “double-precision float” data type */

```

```

f64 dOffset = 0.0; // No offset

f64 dSampRate = RATE_AD; // Set the time-interval for each of Data points

i16 iUnits = 1; // using second as the unit, so 0.00016384 s.

i16 iSampTB = 0; //Default parameters

u16 uSampInt = 0; //Default parameters, using unsigned short int.

static i16 piBuffer[5000] = {0}; /* Temporary memory allocation for an array of static
                                short integer, with maximum accommodation of 5000 data points. */

static f64 pdVoltBuffer[5000] = {0.0}; /* Temporary memory allocation for an array of
static double-float, with maximum accommodation of 5000 data points, used to store the
measurement results of 4096 data. */

static f64 outputArray[5000]={0.0}; /* Memory allocation for a data array for temporary data
                                delivery and storage. */

i16 iDAQstopped = 0; /* The data acquisition completion indicator, where 0 means the
                                measurement is still in processing, or doesn't finish yet. */

u32 ulRetrieved = 0;

i16 iIgnoreWarning = 0;

i16 iYieldON = 1; //Quite a few default setting parameters for NI-DAQ board

for(i=0; i<NPoint; i++) outputArray[i]=0.0; //Data storage memory initialization

```

```

for(j=0; j<NTimes0; j++) {

    /* NI-DAQ board data acquisition processing, set the iteration time for the data
       acquisition cycles as “NTimes0”, using “for” Loop */

    iStatus = Select_Signal (iDevice, ND_IN_START_TRIGGER, ND_PFI_0,
ND_LOW_TO_HIGH); //1. * Setup part: setting the status of the Board and leading the
external trigger signal into the “PFI0” pin of the instrument! */

    // Select_Signal (deviceNumber, Trigger_signal, source_Trigger, sourceSpec)
    iRetVal = NIDAQErrorHandler(iStatus, "Select_Signal", iIgnoreWarning);

    //Reset the error handler

    iStatus = DAQ_Config(iDevice, iStartTrig, iExtConv);

    // 1: External Trigger; 0: Use onboard Internal Clock to control the acquisition
    iRetVal = NIDAQErrorHandler(iStatus, "DAQ_Config", iIgnoreWarning);

    //Reset the error handler, including the NI-DAQ trigger and relevant configuration.

    iStatus = DAQ_Rate(dSampRate, iUnits, &iSampTB, &uSampInt);

    /* Set the acquisition interval for each data point in appropriate unit (s). And
       initialization of both the “iSampTB” (timebase) and “uSampInt” (interval). */

    iStatus = DAQ_Start(iDevice, iChan, iGain, piBuffer, ulCount, iSampTB, uSampInt);

    /* Prepare the data acquisition and set all the processing parameters previously mentioned, where
       the data array “piBuffer” is used to store the acquired counts in each time-interval. */

```

```

iRetVal = NIDAQErrorHandler(iStatus, "DAQ_Start", iIgnoreWarning);

//Reset the error handler, start the data acquisition.

while ((iDAQstopped != 1) && (iStatus == 0)) {

/* 2. * Taking Data Part*, employing a “while” Loop to check if the preset data
acquisition process is complete or not. A single data acquisition cycle. */

iStatus = DAQ_Check(iDevice, &iDAQstopped, &ulRetrieved);

//Check the Status of NI-DAQ

iRetVal = NIDAQYield(iYieldON);

//Check the error indicator of NI-DAQ

}

//3 * Finish Data Acquisition, re-initialization and data storage

iRetVal = NIDAQErrorHandler(iStatus, "DAQ_Check", iIgnoreWarning);

//After the data acquisition, Reset the error handler.

iStatus = DAQ_VScale(iDevice, iChan, iGain, dGainAdjust, dOffset, ulCount, piBuffer,
pdVoltBuffer);

/* Check the status, store the acquired data into “piBuffer” and “pdVoltBuffer”. The binary
data is acquired, but the double-precision values are returned in pdVoltBuffer. */

iRetVal = NIDAQErrorHandler(iStatus, "DAQ_VScale", iIgnoreWarning);

//Reset the error handler.

iStatus = DAQ_Config(iDevice, 0, 0);

```

```

// CLEANUP, set triggering mode back to initial state.

/* 0: Set the trigger for another NI-DAQ sequence (the default); 0: Set PFI line back
to initial state. */

iStatus = Select_Signal(iDevice, ND_IN_START_TRIGGER, ND_AUTOMATIC,
                        ND_DONT_CARE);

iStatus = DAQ_Clear(iDevice);

iDAQstopped = 0; //a few command-lines to finish up the current Acquisition cycle.

for(i=0; i<NPoint; i++){ /* Using a “for” Loop to save Data into outputArray[], employing the
accumulative style: Adding the corresponding data in each of time-intervals of all the previous
data-acquisition cycles together! */

outputArray[i]+=pdVoltBuffer[i];
pdVoltBuffer[i]=0;
piBuffer[i]=0; /* After data retrieving, Initialization of the data array for the next cycle of data
                acquisition. */

        }

} /* Very important bracket, the end of the big “for” (j) Loop, finishing all of the data
   acquisition cycles!

```

```

        for(i=0; i<NPoint; i++){
            Data0X[i]=(float)i;
            Data0Y[i]=(float)outputArray[i];
        } //Save the accumulative data for each of the time-intervals

        NumData0=NPoint;
        for(i=0; i<NumData0; i++){ // Saving the Original Data for back-up
            OrgData0X[i]=Data0X[i];
            OrgData0Y[i]=Data0Y[i]; }
    } //The end of NIDAQControl class!

```

B.6 Set the Omicron SAC card to record the interferometric two-pulse correlation (I2PC) counts for the 7 channeltron detectors

```

#include "SacDriverDll.h" //Include the head file for the Omicron card

void CGraphDoc::SACControl() //Construct a class for Omicron SAC card
{
    int i,k; /* Local integer variable Declaration for SAC card */
    int sacNChannels = NumCH_SAC; // Number of channels used in data acquisition
    unsigned long dwelluSec = (unsigned long) Dwell_SAC;
    /* Set the duration time for each of the data acquisition intervals */
    long numReads = 0; // The default value

```

```

unsigned long* pbuf = 0; //Temporary memory allocation for data buffer

unsigned long* sacArray = 0; //Memory allocation and initialization for data storage.

long sacNPoint = NumDATA_SAC; //Number of data points for each channeltron

long sacNData = sacNPoint*sacNChannels; /* The total number of data points for
                                         all of channels functioning in data acquisition process. */

sacArray = new unsigned long[sacNData]; //Memory allocation for saving the data.

NTimes2=ITRE_SAC;

/* Set the data acquisition iteration time for the SAC card, and Keep in mind: the SAC
card starts each of data acquisition cycle just a little bit after the NI-DAQ AD board
does. */

for(k=0; k<NTimes2; k++) { // Using "for" Loop for the acquisition iteration time !

    for(i=0; i<sacNData; i++) sacArray[i] = 0; //Data array initialization!

    SAC::Init (); //SAC card initialization

    SAC::EmptyBuffer (); //Clear the memory buffer for the SAC card

    SAC::SetDwellTime(dwelSec*1E-6); /* Set the duration time for each
                                         data-acquisition interval in unit of "second" */

    pbuf = SAC::PrepareCountingDMA(sacNChannels, sacNPoint);

    if (pbuf == 0) {

```

```

        AfxMessageBox("Unable to allocate memory to SAC board");
        exit (0); }

/* Allocate the dynamic memory accessory (DMA) unit for data acquisition and check
the status of NI-DAQ SAC card! */

SAC::StartCountingDMA(); // Start the Data Acquisition in the SAC card
while (!SAC::IsFinishedCountingDMA())
{Sleep(1); } //Check if the Data acquisition process is finished or not!

for(i=0; i<sacNData; i++){
    sacArray[i]+=(long)(pbuf[i] & 0x7FFFFFFF);
} /* Using a "for" Loop to save Data into the sacArray [], as an accumulative
style: Adding the corresponding data in each of time-intervals and in various channeltrons of all
the previous data-acquisition cycles together! */

SAC::ResetCountingDMA (); /* Reset the DMA after each of data
acquisition cycle! */

SAC::EndCountingPolled ();
SAC::Exit();

//Clearing the SAC board after each data acquisition cycle.

```

```
    } /* Very important bracket, the end of the big “for” (k) Loop, finishing all of the data acquisition cycles for the Omicron SAC card!
```

```
    ....
```

```
    if(sacNChannels==7){ for(i=0; i<sacNPoint; i++){
```

```
        Data2X[i]=(float)i;
```

```
        Data2Y[i]=(float)sacArray[7*i];
```

```
        Data3Y[i]=(float)sacArray[7*i+1];
```

```
        Data4Y[i]=(float)sacArray[7*i+2];
```

```
        Data5Y[i]=(float)sacArray[7*i+3];
```

```
        Data6Y[i]=(float)sacArray[7*i+4];
```

```
        Data7Y[i]=(float)sacArray[7*i+5];
```

```
        Data8Y[i]=(float)sacArray[7*i+6]; }
```

```
    } /* Saving the accumulative data recorded by SAC card into 7 different data array, representing the I2PC signals from 7 different channeltron detectors. */
```

```
    delete [] sacArray; // Delete the sacArray [], scavenge the dynamic memory!
```

```
    } //The end of SACControl() class!
```

B.7 Set the GPIB control to manipulate the SR430 processing, send commands to activate the NI-DAQ-AD-1 board and Omicron SAC card, and turn on/off the front-bias high voltages for the channeltron detectors

```
void CGraphDoc::GPIBControl()

/* Construct a class for SRS430, which is simplified as SR430 in the software! */

{   int SR430;    //Definition of SR430

    char cmd[40];

    int i;

    int sp=0;    //Some local variables definition and initialization

    short buffer[5000];

    char scan[20]; //Local data arrays definition!

    int status=1; //Set the status of SR430 to "ready"!

    for(i=0; i<5000; i++) buffer[i]=0; //Data array initialization and memory allocation.

    SR430 = ibdev(BDINDEX, PRIMARY_ADDR_OF_SCOPE_1, NO_SECONDARY_ADDR,
    TIMEOUT, EOTMODE, EOSMODE);

    //Device SR430 Initialization with some default setting parameters.

    if (ibsta & ERR)

        {AfxMessageBox ("Unable to open device SR430") ;}
```

```

//Open the device SR430, and check the status!

ibclr(SR430); //Clear the device SR430.

if (ibsta & ERR)
    {AfxMessageBox("Unable to clear device SR430");}

//Check the status after device clearing process!

    sprintf(cmd, "OUTP 1\n");
    ibwrt(SR430, cmd, strlen(cmd));

//Direct SR430 output to the GPIB interface.

    sprintf(cmd, "BWTH %d\n", BINWIDTH_SR430);
    ibwrt (SR430, cmd, strlen(cmd));

/* Set the Binwidth (time duration for each data acquisition interval) of SR430 to
BINWIDTH_SR430, which is 163.84 us for our experiment. */

    sprintf (cmd,"BREC %d\n", NumBINS_SR430);
    ibwrt (SR430, cmd, strlen(cmd));

/* Set Number of bins (or data points) per acquisition scanning cycle to NumBINS_SR430
(which is 4096 typically). */

    sprintf(cmd, "RSCN %d\n", ITRE_SR430);
    ibwrt (SR430, cmd, strlen(cmd));

```

```

//Set the data acquisition iteration times to ITRE_SR430.

sprintf(cmd, "ACMD 0\n");

ibwrt (SR430, cmd, strlen(cmd));

/* Set the data acquisition scanning mode as “accumulative” mode, all the counts from each of
previous scans should be summed for each corresponding time-bin! */

sprintf(cmd, "CLRS\n");

ibwrt (SR430, cmd, strlen(cmd)); // Clear the device SR430

sprintf(cmd, "SSCN\n");

ibwrt (SR430, cmd, strlen(cmd));

//Start the data acquisition scanning using the preset parameters!

MultiON (); //Apply the front-bias high voltage to the channeltrons
NIDAQControl (); //Activate the NI-DAQ AD board
SACControl (); //Activate the Omicron SAC board.
MultiOFF (); //Turn of the high voltage from the channeltron detectors

do{

sprintf(cmd, "*STB?\n");

ibwrt (SR430, cmd, strlen(cmd));

/* Communicating with SR430 by using serial poll* /

```

```

        ibrd (SR430, scan, 40); //Retrieving the current status of SR430

        status=(atoi(scan))%2; //Checking the current status of SR430, the last digital
    } while(!(status & 1)); /* Using a “do-while” Loop to check whether the data
acquisition scanning of the SR430 has finished or not! */

        sprintf(cmd, "BINB?\n");
        ibwrt (SR430, cmd, strlen(cmd));

/* After the SR430 data acquisition has been finished, Read Recorded Data from the memory in
the ASCII format */

ibrd (SR430, (char *)buffer, 2*4096); /* Store the data read from the SR430 memory to a
temporary array ( buffer[] ) as the data type of short integer. */

ibonl(SR430, 0); //Clearing and resetting the Device after data saving!

// Data from SR430 is supposed to be displaying in the panel 1.

        for(i=0; i<4096; i++){
                Data1X[i]=(float)i;
                Data1Y[i]=(float)buffer[i]; }

/*Data obtained from SR430 are forced to convert to “float” and saved into some other
permanent data arrays! */

    } // The end of GPIBControl () class!

```

B.8 A separate C++ program (main {}) to generate the synchronized TTL triggering signal for the Omicron SAC card. The commands are sent through the NI-DAQ-2 board.

```
# include "stdio.h"

#include "nidaqex.h" //Including essential headfile

void main(void)

//Using a separate C++ main {} function to generate a sequential TTL pulsed signals
{
    int i=0; int time=1;

    i16 iStatus = 0; i16 iRetVal = 0; i16 iDevice = 1; //Board index 1

    i16 iNumChans = 1; i16 iChan = 0; //Only one channel with an index 0

    /* Several local variable Declaration and Initialization, the data type is short int ! */
    static i16 piChanVect[1] = {0}; //Initialization of an array with only a single item.

    //analog signals output, only using single output channel.

    static f64 pdBuffer[100] = {0}; // Memory allocation for storage data
    static i16 piBuffer[100] = {0}; // Memory allocation for transformed data

    u32 ulCount = 100; //Each data-point interval could be divided into 100 small divisions
    u32 ulIterations = 4096; /* Each generation cycle includes a sequence of 4096 different
        TTL signals */

    f64 dUpdateRate = 1.34102*4096*100;

    /*Set the sampling rate for each of the TTL signals, obvious it is 100 times faster
```

compared to the data-acquisition rate, which means the TTL width is 1/100 of each data-acquisition time interval (Referred to Fig. B.1). */

```
i32 ITimeout = 180; //Set timeout value for the NI-DAQ 2 board
i16 iIgnoreWarning = 0; //Default value

iStatus = Timeout_Config(iDevice, -1); //Initialization of the NI-DAQ 2 board
iRetVal = NIDAQErrorHandler(iStatus, "Timeout_Config", iIgnoreWarning);
//Check the board status and setup the ErrorHandler

printf("Please Choose Corresponding Trigger Rate from the following: \n\n");
printf("1. Original Trigger Rate: 163.84 us. (Default Value)\n");
printf("2. Double Original Trigger Rate: 81.92 us. \n");
printf("3. 4 times of Original Trigger Rate: 40.96 us. \n\n");
printf("Your Option: ");
scanf("%d", &time);
```

/* We designed a customer oriented computer interface, which allow the customer to generate the TTL trigger rates from the default value, up to 4 times as fast as the default value. The customers should make their desired option, typically choosing "1". */

```
//The digital data array initialization
pdBuffer[0]=8; //The first data in the array is high-value, or "1"
for (i=1;i<100;i++)
```

```

    pdBuffer[i]=0; //The rest of data in the array is low-value, or "0"

//So this gives an identified feature of the TTL signal.

    if (iStatus == 0) {
/* If the NI-DAQ 2 board is available (or free), we direct it to TTL signals generation. */
        if (time == 1 || time ==2) time*=1;
        else if (time ==3) time=time+1;
        else time=1; //Set up the appropriate multiplier to satisfy the customers' choice.
        dUpdateRate = dUpdateRate*time;
//Update the sampling rate implementing the multiplier

printf(" A %lu point waveform should be output at a rate of %f updates/sec.\n", ulCount,
(dUpdateRate/100));
/* Output a line in the minor to remind the customer 100 data (actually only one TTL signal) is
generated at the specific rate. This rate is well matched and synchronized with the data-
acquisition interval of all the other instruments or computer boards. */

        iStatus = Select_Signal(iDevice, ND_OUT_START_TRIGGER,
        ND_PFI_0, ND_LOW_TO_HIGH);
// Check the status of NI-DAQ 2, especially set the PFI_0 pin to receive the
external triggering signals. */
        printf(" Apply your digital trigger signal to PFI0 when ready.\n");
//Reminder regarding to external trigger

```

```

iRetVal = NIDAQErrorHandler(iStatus, "Select_Signal", iIgnoreWarning);

//Set the ErrorHandler again

iStatus = WFM_Scale(iDevice, iChan, ulCount, 1.0, pdBuffer, piBuffer);

/* Prepare the wave generation through channel-0 of the NI-DAQ 2 board, with the configuration
given by the data array pdBuffer [100] (data type is the double-precision float); and direct the
output wave to the new data array piBuffer [], whose data type is static short integer. The
parameter "1.0" means generation of a Square wave form!)

iRetVal = NIDAQErrorHandler(iStatus, "WFM_Scale", iIgnoreWarning);

//Reset the ErrorHandler at the current situation!

while(1) { /* Using a always-true "while" Loop, so the TTL signals generation will be
continuous and never-ending, unless there is an error occurring, or the program is forced to
close! */

iStatus = WFM_Op(iDevice, iNumChans, piChanVect, piBuffer, ulCount, ulIterations,
                dUpdateRate);

/* Generating a sequence of ulIterations (4096) TTL signals in a single data-generation channel,
with a sampling rate-, dUpdateRate; outputting the TTL signals to piBuffer [] array. After each
cycle of signal generation, there will come another cycle, -which will be never ending! */

iRetVal = NIDAQErrorHandler(iStatus, "WFM_Op", iIgnoreWarning);

//Check the Error indicator continuous while the TTL signals generation!

```

```

}; //End of the “while” Loop!

iStatus = AO_VWrite(iDevice, iChan, 0.0);

/* CLEAR UP the device, and Set the output to 0 volts. */

iStatus = Select_Signal(iDevice, ND_OUT_START_TRIGGER,
ND_AUTOMATIC, ND_LOW_TO_HIGH);
// Reset the NI-DAQ 2 board to “ready” status, and set an automatically generated trigger!
} /* The end of the big “if” Loop, followed by the case when the NI-DAQ 2 is not
available! */

else {printf("Check the parameters and status of NIDAQMakeBuffer! \n");
} /* The status of the NI-DAQ 2 board is busy or available, so it cannot be directed
to wave-generating! */

iStatus = Timeout_Config(iDevice, -1); /* Disable the Timeout function! */

}/* End of the main {} program! */

```

APPENDIX C

UNIVERSAL CURVE FOR ELECTRON ESCAPE DEPTH

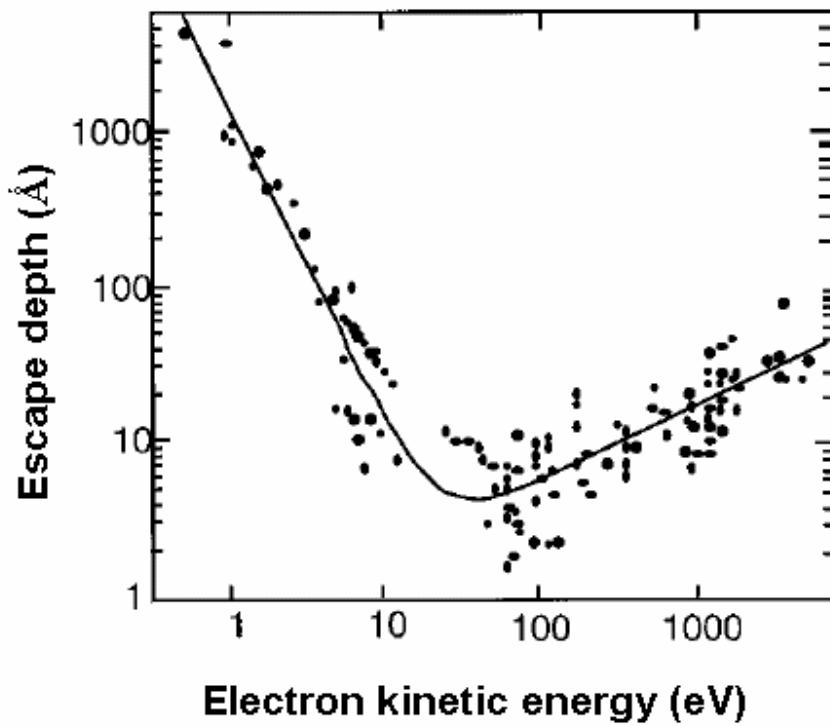


Figure C.1 Universal curve for electron escape depth.

From Ref. [69].

APPENDIX D

DENSITY FUNCTIONAL THEORY

Analytic solutions of the Schrödinger equation and numerically exact solutions are only available for a few very simple systems; however, in most cases of interest, such as reactions on surfaces in chemistry or electron-electron interaction in solids, require the use of approximate Hamiltonians or simplified computational schemes. In order to predict the physical and chemical properties of many-body systems with reliability and without excessive computation, the density functional formalism was developed [140, 141].

The predecessor of density function theory (DFT) is Thomas-Fermi theory [142], where the chemical potential μ can be expressed as,

$$\mu = \frac{\hbar^2}{2m} (3\pi^2 n(\vec{r}))^{2/3} + v_{eff}(\vec{r}), \quad (\text{D.1})$$

in which the $n(\vec{r})$ and $v_{eff}(\vec{r})$ are the electron density and effective potential in a system of interacting electrons, respectively. However, it was not clear whether there is a strict relation between the electron density appearing in the Thomas-Fermi equations and the corresponding many-body wave function.

Analogous to the Hartree-Fock method [143, 144], Kohn and Sham developed the so-called Kohn-Sham equations with respect to the single particle states [106],

$$\left\{-\frac{\hbar^2}{2m}\nabla^2 + v_{\text{ext}}(\vec{r}) + v_H(\vec{r}) + v_{xc}(\vec{r})\right\}\psi_i(\vec{r}) = \varepsilon_i\psi_i(\vec{r}). \quad (\text{D.2})$$

Thus, the effective one-electron potential is given by,

$$v_{\text{eff}}(\vec{r}) = v_{\text{ext}}(\vec{r}) + v_H(\vec{r}) + v_{xc}(\vec{r}): \quad (\text{D.3})$$

where the term $v_{\text{ext}}(\vec{r})$ represents the external potential due to the nucleus in the system,

$$v_{\text{ext}}(\vec{r}) = -\sum_I \frac{Z_I \cdot e^2}{|\vec{r} - \vec{R}_I|}; \quad (\text{D.4})$$

the Hartree potential $v_H(\vec{r})$ is defined as

$$v_H(\vec{r}) = \int d^3r' \cdot n(\vec{r}') \frac{e^2}{|\vec{r} - \vec{r}'|}; \quad (\text{D.5})$$

which corresponds to the electrostatic potential of all other electrons; the third term $v_{xc}(\vec{r})$ in Eq. (D.3) is the exchange-correlation potential from the derivative of the exchange-correlation functional $E_{xc}[n]$,

$$v_{xc}(\vec{r}) = \frac{\delta E_{xc}[n]}{\delta n}. \quad (\text{D.6})$$

The exchange-correlation functional $E_{xc}[n]$ can be written as

$$E_{xc}[n] = \int d^3r \cdot n(\vec{r}) \cdot \varepsilon_{xc}[n](\vec{r}), \quad (\text{D.7})$$

where $\varepsilon_{XC}[n](\vec{r})$ is the exchange-correlation energy per particle at the point \vec{r} , but depends on the whole electron density distribution $n(\vec{r})$. Generally, in a many-body system, the exchange-correlation energy is not known, and cannot be exactly derived. What is known is the exchange-correlation energy for the homogenous electron gas, i.e. for a system with a constant electron density. Therefore, two important models have been developed for the exchange-correlation energy calculation: one is called Local Density Approximation (LDA) model [145], and a more recent one is called Generalized Gradient Approximation (GGA) model [115, 116], the corresponding exchange energies are described by the following equations: Eq. (D.8) and Eq. (D.9) respectively,

$$E_{XC}^{LDA}[n] = \int d^3r \cdot n(\vec{r}) \cdot \varepsilon_{XC}^{LDA}[n](\vec{r}), \quad (D.8)$$

and

$$E_{XC}^{GGA}[n] = \int d^3r \cdot n(\vec{r}) \cdot \varepsilon_{XC}^{GGA}(n(\vec{r}), |\nabla n(\vec{r})|). \quad (D.9)$$

The electron density can be expressed as a sum over single-electron states from the solutions of Eq. (D.2),

$$n(\vec{r}) = \sum_i \left| \psi_i(\vec{r}) \right|^2. \quad (D.10)$$

Then the calculated electron density $n(\vec{r})$ can be implemented into Eq. (D.2) again to perform the next iteration cycle of calculation until a satisfactory convergence is obtained.

Bibliography

1. Diebold, U., The Surface Science of Titanium Dioxide. Surf. Sci. Rept., 2003. **48**: p. 53.
2. H. Petek and S. Ogawa, Femtosecond Time-Resolved Two-Photon Photoemission Studies of Electron Dynamics in Metals. Prog. in Surf. Sci., 1997. **56**: p. 239.
3. M. Grätzel, Heterogeneous photochemical electron transfer. 1989: CRC.
4. Samsonov, G.V., The Oxide Handbook. 1982, New York: IFI/Plenum Press.
5. B. O'Regan and M. Grätzel, A low-cost, high-efficiency solar cell based on dye-sensitized colloidal TiO₂ films. Nature, 1991. **353**: p. 737.
6. M. A. Henderson, The interaction of water with solid surfaces: fundamental aspects revisited. Surf. Sci. Rept., 2002. **46**: p. 1.
7. S. Munnix and M. Schmeits, Phys. Rev. B, 1984. **30**: p. 2202.
8. P. Y. Yu and M. Cardona, Fundamentals of Semiconductors. 1999: Springer.
9. K. A. See and R.A. Bartvnski, J. Vac. Sci. Technol. A, 1992. **10**: p. 2951.
10. T. Minato, et al., Phys. Rev. Lett., submitted.
11. A. L. Linsebigler, G. Lu, and J.T. Yates, Photocatalysis on TiO₂ Surfaces: Principles, Mechanisms, and Selected Results. Chem. Rev., 1995. **95**: p. 735.
12. Kamat, P.V., Photochemistry on Nonreactive and Reactive Semiconductor Surfaces. Chem. Rev., 1993. **93**: p. 267.
13. A. Fujishima and K. Honda, Nature, 1972. **238**: p. 27.
14. Grätzel, M., Photoelectrochemical cells. Nature, 2001. **414**: p. 338.
15. R. Wang, et al., Nature, 1997. **388**: p. 431.
16. S. A. Campbell, et al., IBM J. Res. Develop., 1999. **43**: p. 383.
17. Grant, F.A., Rev. Mod. Phys., 1959. **31**: p. 646.
18. A. Nakajima, et al., Langmuir, 2000. **16**: p. 7044.
19. R. E. Wyatt and J.Z.H. Zhang, Dynamics of Molecules and Chemical Reactions. 1996: Marcel Dekker, Inc.
20. J. D. Simon, Ultrafast Dynamics of Chemical Systems. 1994: Kluwer Academic Publishers.
21. J. B. Asbury, et al., Ultrafast Electron Transfer Dynamics from Molecular Adsorbates to Semiconductor Nanocrystalline Thin Films. J. Phys. Chem. B, 2001. **105**: p. 4545.
22. R. Huber, et al., Real-Time Observation of Photoinduced Adiabatic Electron Transfer in Strongly Coupled Dye/Semiconductor Colloidal Systems with a 6 fs Time Constant. J. Phys. Chem. B, 2002. **106**: p. 6494.
23. J. Schnadt, Experimental evidence for sub-3-fs charge transfer from an aromatic adsorbate to a semiconductor. Nature, 2002. **418**: p. 620.
24. L. G. C. Rego and V.S. Batista, Quantum Dynamics Simulations of Interfacial Electron Transfer in Sensitized TiO₂ Semiconductors. J. Am. Chem. Soc., 2003. **125**: p. 7989.

25. A. Stingl, C. Spielmann, and F. Krausz, Generation of 11-fs pulses from a Ti:Sapphire laser without the use of prisms. *Opt. Lett.*, 1994. **19**: p. 204.
26. X. -Y. Zhu, Electronic structure and electron dynamics at molecule-metal interfaces: implications for molecule-based electronics. *Surf. Sci. Rept.*, 2004. **56**: p. 1.
27. M. J. Weida, et al., Ultrafast interferometric pump-probe correlation measurements in systems with broadened bands or continua. *J. Opt. Soc. Am. B*, 2000. **17**: p. 1443.
28. J. -C Diels and W. Rudolph, *Ultrashort Laser Pulse Phenomena*. 1995: ACADEMIC PRESS.
29. K. Onda, B. Li, and H. Petek, Two-photon photoemission spectroscopy of TiO₂ (110) surfaces modified by defects and O₂ or H₂O adsorbates. *Phys. Rev. B*, 2004. **70**: p. 045415.
30. K. Onda, et al., Wet Electrons at the H₂O/TiO₂(110) Surface. *Science*, 2005. **308**: p. 1154.
31. B. Li, et al., Ultrafast Interfacial Proton-Coupled Electron Transfer. *Science*, 2006. **311**: p. 1436.
32. U. Keller, et al., Femtosecond pulses from a continuously self-starting passively mode-locked Ti:Sapphire laser. *Opt. Lett.*, 1991. **16**: p. 1022.
33. D. E. Spence, P. N. Kean, and W. Sibbett, 60-fsec pulse generation from a self-mode-locked Ti:Sapphire laser. *Opt. Lett.*, 1991. **16**: p. 42.
34. H. Liu, J. Yao, and A. Puri, Second and third harmonic generation in BBO by femtosecond Ti:Sapphire laser pulses. *Opt. Comm.*, 1994. **109**: p. 139.
35. D. A. Roberts, Simplified Characterization of Uniaxial and Biaxial Nonlinear Optical Crystals: A Plea for Standardization of Nomenclature and Conventions. *IEEE J. of Quan. Elec.*, 1992. **28**: p. 2057.
36. Jackson, J.D., *Classical Electrodynamics*. 1975: John Wiley & Sons, Inc.
37. M. Born and E. Wolf, *Principles of optics*. 1999: Cambridge University Press.
38. Yariv, A., *Quantum Electronics*. 1989: John Wiley & Sons.
39. N. W. Ashcroft and N.D. Mermin, *Solid State Physics*. 1976: Holt, Rinehart and Winston.
40. U. Hofer, et al., Time-Resolved Coherent Photoelectron Spectroscopy of Quantized Electronic States on Metal Surfaces. *Science*, 1997. **277**: p. 1480.
41. Haight, R., Electron dynamics at surfaces. *Surf. Sci. Rept.*, 1995. **21**: p. 275.
42. Henrich, V.E., The surfaces of metal oxides. *Rep. Prog. Phys.*, 1985. **48**: p. 1481.
43. Bokor, J., Ultrafast Dynamics at Semiconductor and Metal Surfaces. *Science*, 1989. **246**: p. 1130.
44. Yates, J.T., *Experimental Innovations in Surface Science*. 1997: AIP Press.
45. S. Krischok, et al., *Surf. Sci.*, 2001. **495**: p. 8.
46. Henderson, M.A., *Surf. Sci.*, 1996. **355**: p. 151.
47. Cox, P.A., *Transition Metal Oxides - An Introduction to Their Electronic Structure, Properties*. 1992, Oxford: Carendon Press.
48. V. E. Henrich and P.A. Cox, *The Surface Science of Metal Oxides*. 1994: Cambridge University Press.
49. Weinelt, M., Time-resolved two-photon photoemission from metal surfaces. *J. Phys.: Condens. Matter*, 2002. **14**: p. R1099.
50. S. Ogawa, H. Nagano, and H. Petek, *Phys. Rev. B*, 1997. **55**: p. 10869.

51. S. Ogawa, H. Nagano, and H. Petek, Optical Dephasing in Cu(111) Measured by Interferometric Two-Photon Time-resolved Photoemission. *Phys. Rev. Lett.*, 1997. **78**: p. 1339.
52. T. Hertel, et al., *Phys. Rev. Lett.*, 1996. **76**: p. 535.
53. T. Hertel, et al., *J. Vac. Sci. Tech. A*, 1997. **15**: p. 1503.
54. P. Szymanski, S. Garrett-Roe, and C.B. Harris, *Prog. in Surf. Sci.*, 2005. **78**: p. 1.
55. C. Gahl, et al., *Phys. Rev. Lett.*, 2002. **89**: p. 1074021.
56. A. D. Miller, et al., Electron Solvation in Two Dimensions. *Science*, 2002. **297**: p. 1163.
57. N. D. Fatti, et al., Nonequilibrium electron dynamics in noble metals. *Phys. Rev. B*, 2000. **61**: p. 16956.
58. Quinn, J.J., *Appl. Phys. Lett.*, 1962. **126**: p. 1453.
59. Quinn, J.J., *Phys. Rev.*, 1958. **112**: p. 812.
60. V. E. Gusev and O.B. Wright, *Phys. Rev. B*, 1998. **57**: p. 2878.
61. R. Matzdorf, G. Meister, and A. Goldmann, *Surf. Sci.*, 1993. **286**: p. 56.
62. E. Knoesel, A. Hotzel, and M. Wolf, Ultrafast dynamics of hot electrons and holes in copper: Excitation, energy relaxation and transport effects. *Phys. Rev. B*, 1998. **57**: p. 12812.
63. H. Haug and S.W. Koch, *Quantum Theory of the Optical and Electronic Properties of Semiconductors*. 1990, Singapore: World Scientific.
64. Ziman, J.M., *Electrons and Phonons*. 1960, Oxford: Clarendon.
65. Palik, E.D., *Handbook of Optical Constants of Solids*. 1985, New York: Academic Press.
66. J. Gao, et al., *Phys. Rev. B*, 1997. **56**: p. 1099.
67. P. M. Echenique, et al., Theory of inelastic lifetimes of low-energy electrons in metals. *Chem. Phys.*, 2000. **251**: p. 1.
68. M. Aeschlimann, et al., Transport and dynamics of optically excited electrons in metals. *Appl. Phys. A*, 2000. **71**: p. 485.
69. I. Lindau and W.E. Spicer, *J. Elect. Spect. Rel. Phen.*, 1974. **3**: p. 409.
70. E. J. Canto-Said, et al., *Opt. Lett.*, 1993. **18**: p. 2038.
71. W. Plab, et al., *Appl. Phys. B*, 1992. **54**: p. 199.
72. G. G. Brewer and E.L. Hahn, *Phys. Rev. A*, 1975. **11**: p. 1641.
73. R. L. Kurtz, et al., *Surf. Sci.*, 1989. **218**: p. 178.
74. W. Nessler, et al., *J. Elect. Spect. Rel. Phen.*, 1998. **88-91**: p. 495.
75. H. Petek, et al., Optical Phase Control of Coherent Electron Dynamics in Metals. *Phys. Rev. Lett.*, 1997. **79**: p. 4649.
76. J. Zhao, et al., *Phys. Rev. B*, 2006. **73**: p. 159309.
77. D. S. Warren and A.J. McQuillan, *J. Phys. Chem. B*, 2004. **108**: p. 19373.
78. Somorjai, G.A., *Introduction to Surface Chemistry and Catalysis*. 1994, New York: Wiley.
79. M. A. Henderson, et al., *J. Phys. Chem. B*, 1999. **103**: p. 5328.
80. C. N. Rusu and J.T. Yates, *Langmuir*, 1997. **13**: p. 4311.
81. W. S. Epling, et al., *Surf. Sci.*, 1998. **412**: p. 333.
82. M. D. Rasmussen, L. M. Molina, and B. Hammer, *J. Chem. Phys.*, 2004. **120**: p. 988.
83. G. Lu, A. L. Linsebigler, and J.T. Yates, *J. Chem. Phys.*, 1995. **102**: p. 4657.
84. U. Diebold, et al., *Surf. Sci.*, 1998. **411**: p. 137.
85. J. T. Mayer, et al., *J. Elect. Spect. Rel. Phen.*, 1995. **73**: p. 1.
86. S. Wendt, et al., *Surf. Sci.*, 2005. **598**: p. 226.

87. T. J. Beck, et al., *Surf. Sci.*, 2005. **591**: p. L267.
88. O. Bulub, U. Diebold, and G. Kresse, 90, 2003: p. 016102.
89. J. Zhao, et al., *Solvated Electrons on Metal Oxide Surfaces*. *Chem. Rev.*, in Press.
90. A. Tilocca and A. Selloni, *Langmuir*, 2004. **20**: p. 8379.
91. Zangwill, A., *Physics at Surfaces*. 1994, Cambridge: Cambridge University Press.
92. J. R. MacDonald and J. Barlow, *J. Chem. Phys.*, 1963. **39**: p. 412.
93. C. M. Mate, C. -T. Kao, and G.A. Somorjai, *Surf. Sci.*, 1988. **206**: p. 145.
94. M. B. Hugenschmidt, L. Gamble, and C.T. Campbell, *Surf. Sci.*, 1994. **302**: p. 329.
95. C. Zhang and P.J.D. Lindan, *J. Chem. Phys.*, 2003. **119**: p. 9183.
96. C. Zhang and P.J.D. Lindan, *J. Chem. Phys.*, 2003. **118**: p. 4620.
97. T. S. Wittrig, D. E. Ibbotson, and W.H. Weinberg, *Surf. Sci.*, 1981. **102**: p. 506.
98. K. Bange, et al., *Vacuum*, 1983. **33**: p. 757.
99. Linde, R.D., *CRC Handbook of Chemistry and Physics*. 2000, Boca Raton: CRC Press LLC.
100. B. N. J. Persson and L.H. Dubois, *Phys. Rev. B*, 1989. **39**: p. 8220.
101. A. Michaelides, et al., *Phys. Rev. Lett.*, 2003. **90**: p. 216102.
102. Jordan, K.D., *Science*, 2004. **306**: p. 618.
103. J. R. R. Verlet, et al., *Science*, 2005. **307**: p. 93.
104. D. H. Paik, et al., *Science*, 2004. **306**: p. 672.
105. A. E. Bragg, et al., *Science*, 2004. **306**: p. 669.
106. W. Kohn and L.J. Sham, *Phys. Rev.*, 1965. **140**: p. A1133.
107. J. Schnitker and P.J. Rossky, *J. Chem. Phys.*, 1987. **86**: p. 3471.
108. Kim, K.S., *Phys. Rev. Lett.*, 1996. **76**: p. 956.
109. Hammer, N.I., *Science*, 2004. **306**: p. 675.
110. J. Zhao, et al., *Phys. Rev. B*, in Press.
111. S. Suzuki, et al., Hydrogen Adatoms on TiO₂(110)-(1x1) Characterized by Scanning Tunneling Microscopy and Electron Stimulated Desorption. *Phys. Rev. Lett.*, 2000. **84**: p. 2156.
112. A. Yamakata, T. Ishibashi, and H. Onishi, *J. Phys. Chem. B*, 2002. **106**: p. 9122.
113. M. A. Henderson, S. O. Tapia, and M.E. Castro, *Fara. Disc.*, 1999. **114**: p. 313.
114. S. P. Bates, M. J. Gillan, and G. Kresse, *J. Phys. Chem. B*, 1998. **102**: p. 2017.
115. J. P. Perdew, K. Burke, and M. Ernzerhof, *Phys. Rev. Lett.*, 1996. **77**: p. 3865.
116. J. P. Perdew, K. Burke, and M. Ernzerhof, *Phys. Rev. Lett.*, 1997. **78**: p. 1396.
117. J. Zhao and H. Petek, unpublished data.
118. K. Onda, et al., The electronic structure of methanol covered TiO₂(110) surfaces. *Surf. Sci.*, 2005. **593**: p. 32.
119. M. Calatayud, et al., *Catal. Today*, 2003. **85**: p. 125.
120. M. Brause, S. Skordas, and V. Kempter, *Surf. Sci.*, 2000. **445**: p. 224.
121. T. Bredow, et al., *Surf. Sci.*, 1999. **418**: p. 1999.
122. B. Saleh and M.C. Teich, *Fundamentals of Photonics*. 1991, New York: John Wiley & Sons, INC.
123. E. Hendry, et al., *Phys. Rev. B*, 2004. **69**: p. 081101.
124. S. H. Liu, *J. Phys. Chem. B*, 2002. **106**: p. 12908.
125. H. Shirota, et al., *Chem. Phys. Lett.*, 1997. **281**: p. 27.
126. M. S. Pshenichnikov, A. Baltuska, and D. A. Wiersma, *Chem. Phys. Lett.*, 2004. **389**: p. 171.

127. H. Decornez and S. Hammes-Schiffer, *J. Phys. Chem. A*, 2000. **104**: p. 9370.
128. Hammes-Schiffer, S., *Acc. Chem. Res.*, 2001. **34**: p. 273.
129. R. I. Cukier and D.G. Nocera, *Annu. Rev. Phys. Chem.*, 1998. **49**: p. 337.
130. W. Stier and O.V. Prezhdo, *J. Phys. Chem. B*, 2002. **106**: p. 8047.
131. H. Tributsch and L. Pohlmann, *Science*, 1998. **279**: p. 1891.
132. S. J. Schmidtke, D. F. Underwood, and D.A. Blank, *J. Am. Chem. Soc.*, 2004. **126**: p. 8620.
133. S. Luchbrunner, K. Stock, and E. Riedel, *J. Mole. Stru.*, 2004. **700**: p. 13.
134. W. S. Yu, et al., *J. Phys. Chem. A*, 2002. **106**: p. 8006.
135. C. S. Yee, et al., *J. Am. Chem. Soc.*, 2003. **125**: p. 10506.
136. Turi, L., *J. Chem. Phys.*, 1999. **110**: p. 10364.
137. P. Minary, L. Turi, and P.J. Rossky, *J. Chem. Phys.*, 1999. **110**: p. 10953.
138. B. Li, et al., in preparation.
139. Q. B. Lu and T.E. Madey, *Phys. Rev. Lett.*, 1999. **82**: p. 4122.
140. P. Hohenberg and W. Kohn, *Phys. Rev.*, 1964. **136**: p. B864.
141. R. M. Dreizler and E.K.U. Gross, *Density Functional Theory: An Approach to the Quantum Many-Body Problem*. 1990: Springer.
142. Lieb, E.H., *Rev. Mod. Phys.*, 1981. **53**: p. 603.
143. Fock, V.A., *Z. Phys.*, 1930. **15**: p. 126.
144. Hartree, D.R., *Proc. Cambridge. Philos. Soc.*, 1928. **24**: p. 328.
145. D. M. Ceperley and B.J. Alder, *Phys. Rev. Lett.*, 1980. **45**: p. 566.